Title: Emergence of binding and catalysis from a designed generalist binding protein

Authors: Yuda Chen[1†], Sagar Bhattacharya[1†], Lena Bergmann[2†], Galen J. Correy[2†], Sophia Tan[1], Kaipeng Hou[1], Justin Biel[2], Lei Lu[1], Ian Bakanas[1], Nicholas F. Polizzi[3,4], James S. Fraser[2]*,William F. DeGrado[1]*

Affiliations:

[1]Department of Pharmaceutical Chemistry & Cardiovascular Research Institute, University of California, San Francisco, CA 94158, USA.

[2]Department of Bioengineering and Therapeutic Sciences, University of California, San Francisco, CA 94158, USA

[3]Department of Cancer Biology, Dana-Farber Cancer Institute, Boston, MA 02215, USA.

[4]Department of Biological Chemistry and Molecular Pharmacology, Harvard Medical School, Boston, MA 02215, USA.

*Corresponding author. Email: jfraser@fraserlab.com, bill.degrado@ucsf.edu

†These authors contributed equally to this work.

Abstract: The evolution of proteins that bind to small molecules and catalyze chemical transformations played a central role in the emergence of life. While natural proteins have finely tuned affinity for their primary ligands, they also often have weak affinities for other molecules. These interactions serve as starting points for the evolution of new specificities and functions. Inspired by this concept, we determined the ability of a simple *de novo* protein to bind a set of diverse small molecules (< 300 Da) by crystallographic fragment screening. We then used this information to design one variant that binds fluorogenic molecule and another that acts as a highly efficient Kemp eliminase enzyme. Collectively, our work illuminates how the evolution of novel protein functions can emerge from existing proteins.

Main Text: The evolution of life leveraged the emergence of primordial proteins that could bind, utilize, and create new small molecule metabolites and signaling molecules. These proteins evolve on a landscape that is often portrayed pictorially by mapping sequence space into two dimensions (*1–3*). Here, we expand this concept to understand binding specificity, which involves both sequence (collapsing sequence space to only the Y-axis) and chemical diversity (representing chemical space by the X-axis, Fig. 1). Proteins that bind to and catalyze small molecules evolve along this sequence-chemical space landscape, as they acquire new functions. The ability to bind to new chemical entities is represented by horizontal moves in chemical space and enabled through alteration of their amino acid sequences, which are represented by vertical moves.

Such new specificities are thought to have primarily been acquired after gene duplication. In these scenarios, a gene encodes a protein with an existing activity (e.g., strongly binding molecule A) and an "off-target" promiscuous activity (e.g., weak-moderate binding affinity to molecule B) (*4–6*). The duplication event frees the two copies – which initially have "generalist" activities to specialize independently. Mutations to the amino acid sequence of one copy can increase the

specificity for B by substituting residues that contact B or that increase the population of a conformational sub-state that promotes binding. Thus, cells have been evolving an increasing array of proteins with distinct specificities that complement increasing functional complexity and adaptability.

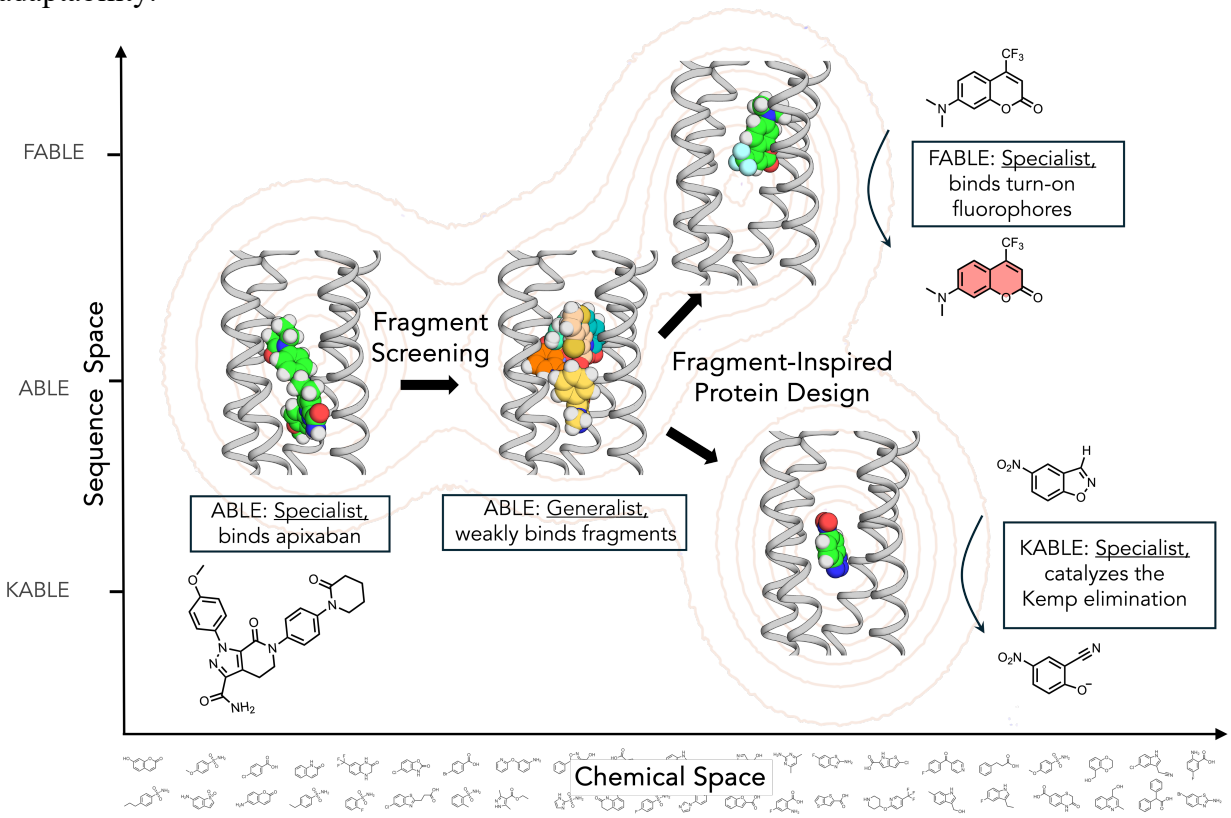

Figure 1: Design of novel functions through exploration of the chemical space and sequence space of protein-ligand interaction via crystallographic fragment screening. Sequence diversity and small molecule chemical diversity are conceptually represented on orthogonal axes, and the contours are meant to denote fitness for binding or catalyzing the Kemp elimination reaction. Starting with ABLE, a specialist for binding apixaban, crystallographic fragment screening revealed ABLE as a generalist for binding 43 chemical fragments. Although the fragments tend to have very low affinity, a set of aromatic fragments informed the design of a fluorescent derivative of ABLE (FABLE), which is a specialist for binding to a turn-on fluorophore. A second set of fragments informed the design of KABLE, an efficient catalyst for the Kemp elimination reaction (k_{cat}/K_M = 600,000 $M^{-1}s^{-1}$).

Even within the gene duplication paradigm, searching broadly and simultaneously through both chemical and sequence space to evolve new functions is daunting. Most experimental work has focused on exploring each of these two variables in isolation: drug discovery involves an extensive search of chemical space to discover small molecules that bind to a target protein with a fixed sequence (*7*), while methods such as yeast display, phage display or directed evolution explore sequence space to discover new protein sequences for a given small molecule (*2*, *3*). *De novo* protein design provides an alternative approach to explore sequence space, and, although *de novo* design of small molecule-binding proteins is still considered a significant challenge (*8*), a number of proteins have been designed to bind drugs and cofactors (*8–15*). However, it is unknown whether designed proteins are more or less specific than natural proteins. The great conformational

stability of *de novo* proteins (*14*) and the idealized nature of their designed interactions might increase their specificity, making it difficult for them to act as generalists and to evolve new functions. Alternatively, they might have relatively low specificity because their binding sites have not been subject to the negative selective pressures that enforce specificity in a natural context.

Aside from acting on their primary substrates and closely related analogs, natural proteins have a low affinity (K_D in the low mM range) for a plethora of small molecular fragments (MW < 300 Da). Although these molecules can bear little resemblance to the protein's natural ligands, they present starting points for evolution of new specificities (*1*, *5*, *16*). In this thinking, the active sites of natural proteins have a repertoire of weak binding sites, which stand ready to evolve novel functions (*5*). Here, we probe the implications of this idea by using fragment discovery to design new binding and catalytic activity paired with *de novo* sequence design.

We chose helical bundles for this application, because they represent one of the most ancient, evolvable, and arguably the most functionally diverse tertiary structures (*17*). Most transmembrane proteins are helical bundles (with the notable exception of beta barrels in outer membranes of bacteria and mitochondria) and they are involved in transport, signal transduction, small molecule binding, and catalysis of a wide range of reactions from proteolysis to the generation and utilization of O_2 (*18*). For instance, G-coupled protein receptors (GPCRs) specialize to recognize a wide array of small molecules in sites bounded by four transmembrane helices (*19*). Helical bundles are also found in water soluble proteins involved in electron transport (*20*), metalloenzymes (*21*), small molecule binding and transport (e.g., serum albumin (*22*)), and natural enzymes such as chorismate mutase (*23*). *De novo* helical bundles have also been evolved to perform essential functions *in vivo* (*24*, *25*).

As a starting point to explore the evolution of novel binding and catalytic functions from promiscuous binding, we used a *de novo* protein, the Apixaban-Binding helical BundLE (ABLE), which was previously designed to bind the antithrombotic drug, apixaban (Fig. 1) (*13*). While ABLE can discriminate apixaban from close congeners, we addressed its specificity towards more distantly related molecules using X-ray crystallography. This crystallographic method is one of several experimental and computational methods that is frequently used to discover fragments with very weak affinity but geometrically well-defined poses for structure-based drug design (*26*). We show that the malleability and promiscuity of ABLE is within the range seen in natural proteins studied by fragment screening (*26–28*). Conformational rearrangements of ABLE's binding site were primarily restricted to sidechain rotamer shifts. Many of the ABLE-binding fragments showed little similarity to apixaban, and some bound in a novel aromatic box opened by conformational rearrangement of a Tyr sidechain. We next asked whether ABLE might be converted from a generalist for binding multiple fragments to a specialist for the binding of turn-on fluorophores. Using different cues from fragment complexes, we also converted ABLE to an enzymatic catalyst for the Kemp Elimination reaction (*29–37*) with a catalytic efficiency (k_{cat}/K_M = 600,000 $M^{-1}s^{-1}$) exceeding the rates of mechanistically similar natural enzymes such as ketosteroid isomerase (k_{cat}/K_M = 540,000 $M^{-1}s^{-1}$) (*38*) and triosephosphate isomerase (k_{cat}/K_M = 440,000 $M^{-1}s^{-1}$) (*39*). Together with previous studies (*13*, *14*, *40–46*), our results show that an impressive range of catalytic and binding functions can emerge through sequence variation of even a simple four-helix scaffold similar to ones that might have emerged early in evolution. These

findings have fundamental implications inspired by protein evolution, as well as practical implications for the design of (*13*, *47–51*) new detectors and catalysts.

Plasticity of the binding site from analyses of crystal structures and molecular dynamics (MD) simulations.

To assess the potential of ABLE (Fig. 2A) to bind ligands other than apixaban, we first examined multiple crystallographic structures of the protein in the absence of apixaban to identify multi-conformational regions that might bind other small molecules. Although the binding site was largely pre-organized to the shape of apixaban (*13*), multiple sidechain conformations were observed near the upper portion of the site (Fig. 2A). In particular, Tyr46 adopted two conformations in the drug-free state, only one of which was present in the apixaban complex. We define the conformer seen in the apixaban complex as "**A**" (for apixaban) and the alternate sub-state as "**B**". A similar conformation emerged from running multiple molecular dynamics simulations of the protein (see section 1.9.1-1.9.2 of the SI). In simulations, Tyr46 exchanged between both sidechain conformations in the drug-free state (fig. S1). Although there is a relatively modest difference in the chi1 and chi2 angles between the two conformers, this small change propagates to a larger displacement of its long aryl sidechain due to the lever arm effect. Other sources of conformational variability in this region included the sidechains of His49, which also polulates more than one rotamer (fig. S2). Collectively, this analysis suggests that the apixaban binding site displays limited sidechain flexibility, particularly at Tyr46 and His49, in the apo state.

Conformational plasticity and binding specificity of ABLE from crystallographic fragment screening

We next used X-ray crystallography to map regions of ABLE's site that were capable of binding to a diverse set of "fragment" (MW < 300 Da) molecules (*52*), which span a range of aliphatic and aromatic character, a logP value between -2.3 and 2.6, and up to four heteroatoms. (see section 1.1-1.2 of the SI). We screened a modest-sized library of 320 small fragments, which represent drug-like moieties, for their ability to bind to ABLE when soaked for two hours into ABLE crystals at about 10 mM concentration (Fig. 2B). Of the 242 compounds where high-quality X-ray diffraction datasets were collected, 43 unique fragments were modeled (Fig. 2B). The resulting hit rate (18%) is similar to the reported hit rates of 7% and 19% for Nsp3 macrodoamin of SARS-CoV-2 and Chikungunya virus, respectively, using the same fragment library and screening method (*27*, *28*) (Fig. 2B). All but four fragments bound within the apixaban binding site. Thus, by this criterion, ABLE has a specificity within the range seen in natural proteins.

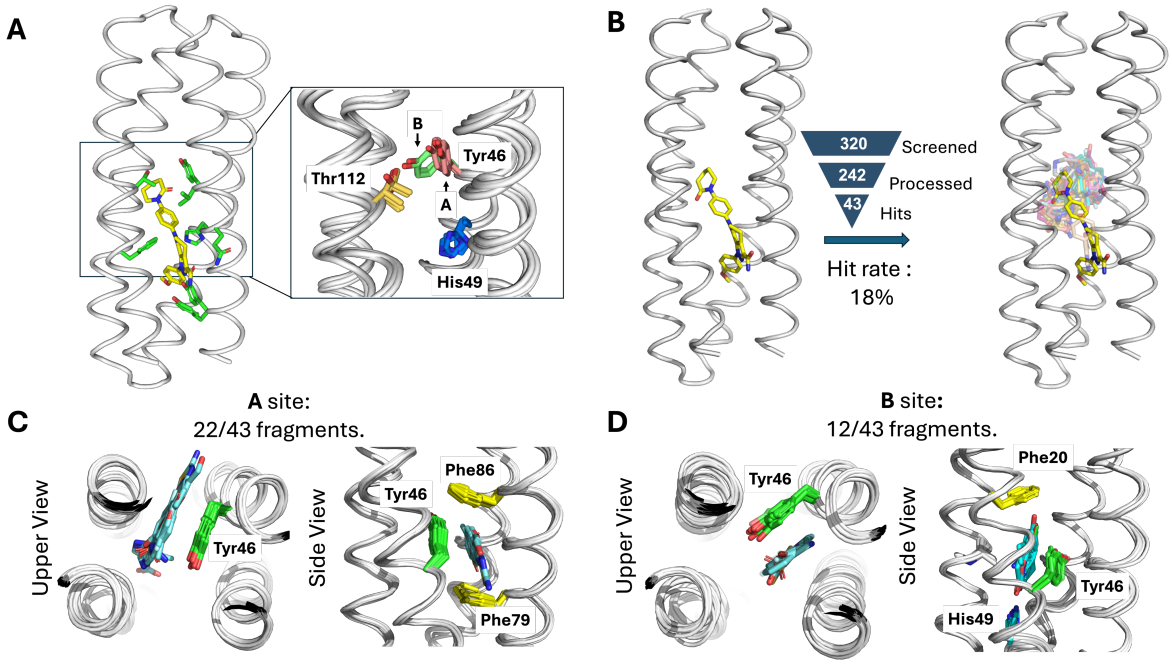

Fig. 2. ABLE binds multiple fragments with small alterations of the binding sites. (**A**) Binding pockets in the apixaban-bound ABLE (PDB: 6W70) and the ligand-free forms (PDBs: 6W6X and 6X8N). The crystal structures have multiple monomers in the asymmetric unit, each of which was superimposed. (**B**) Crystallographic fragment screening reveals expanded chemical space of weak binders; the crystal structures of ABLE in complex with 43 fragments were each solved to to between 1.3-1.6 Å resolution, using Pan-Dataset Density Analysis. The structures were superposed onto the structure of the ABLE-apixaban complex. The backbone structure shown is from chain A of PDB: 6W70, the carbon atoms from the structure of apixaban are shown in yellow sticks, and the remaining residues' carbon atoms in a different color for different fragments. (**C-D**) Most fragments interact with ABLE at one of two binding sites, designated **A** and **B**, which differ by a conformation shift of Tyr46. The complexes are shown looking down the axis of the bundle (left) and rotated by approximately 90° (right). **(C)** 22/43 fragments bind ABLE in an aromatic box formed by Tyr46, Phe79, Phe86, and the backbone of one helix (site **A**). **(D)** 12/43 fragments interact with ABLE at site **B**, where Tyr 46 adopts a different rotamer than in the ABLE-apixaban complex. Site **B** is formed by Phe20, Tyr46, and the backbone of two helices. His49 sits at the bottom of the pocket, forming hydrogen bonds with polar atoms of the fragments. The presence of the fragments in the binding site had only a small effect on the overall tertiary structure of the protein (sub-Å Cα RMSD).

The 39 fragments that bound in ABLE's apixaban-binding site represented diverse chemotypes. The hits collectively have a small but statistically significant tendency to be larger, more apolar, and richer in atoms that are part of aromatic rings when compared to the overall library. (fig. S3) While apixaban has a primary carboxamide (–CO–NH_2) that is bound near the surface of the protein in the ABLE-drug complex. However, the fragments in the 39 complexes were bound more deeply into the pocket and none were found to contain this polar functional group.

Almost all of the bound fragments slot into one of two boxes formed by the distinct conformations of Tyr46 (figs. S4-5). About two-thirds of the fragments bound to conformer **A**, characterized by

an aromatic box comprised of the sidechains of Tyr46 (conformer **A**), Phe79, Phe86, and the backbone of **helix 3**. (Fig. 2C) The other third bound to conformer **B**, which is also an aromatic box comprised of a distinct Tyr46 side chain conformation, Phe20, His 49, and the backbone of **helix 1** (Fig. 2D). The great majority of the fragments also form polar interactions with residues adjacent to the aromatic boxes: namely, Thr112 in conformer **A** and His49 in conformer **B**. (fig. S5) This malleability of ABLE enables adjustment to the shape and properties of the fragments by conformational selection, which is a property of generalist binders (*1*).

Designing Proteins to Bind Fluorogenic Ligands

We next asked whether the newly discovered site defined by conformer **B** would be a good starting point to design a protein with altered binding specificity. Site **B** of ABLE bound the fragment 7-hydroxycoumarin (Fig. 3A), which represents to core of a large class of fluorophores. This suggests that it would be possible to redesign ABLE to bind environment-sensitive, turn-on fluorophores that are larger than the starting fragments. We therefore redesigned the B site to accommodate the larger environment-sensitive coumarin, Cou485 (1, 7-(dimethylamino)-4-(trifluormethyl)-coumarin) using the 7-hydroxycoumarin complex as the starting structure (Fig. 3A) (*53*). The goal of the design was to: 1) create more space to accommodate the additional trifluoromethyl and dimethylamino groups of Cou485, and 2) fill in the pockets that had been used to bind apixaban but were no longer needed for binding Cou485. (Fig. 3A) Using a previously described protocol (*44*, *54*), we selected 43 of ABLE's 126 residues to vary during redesign. Fig. 3A illustrates the gradual migration of the binding site, which accompanied binding to the larger ligand. OmegaFold (*55*) was used to determine whether the new designs would be preorganized in a conformation capable of binding Cou485; other selection metrics are described in the supplement (see section 1.3 of SI).

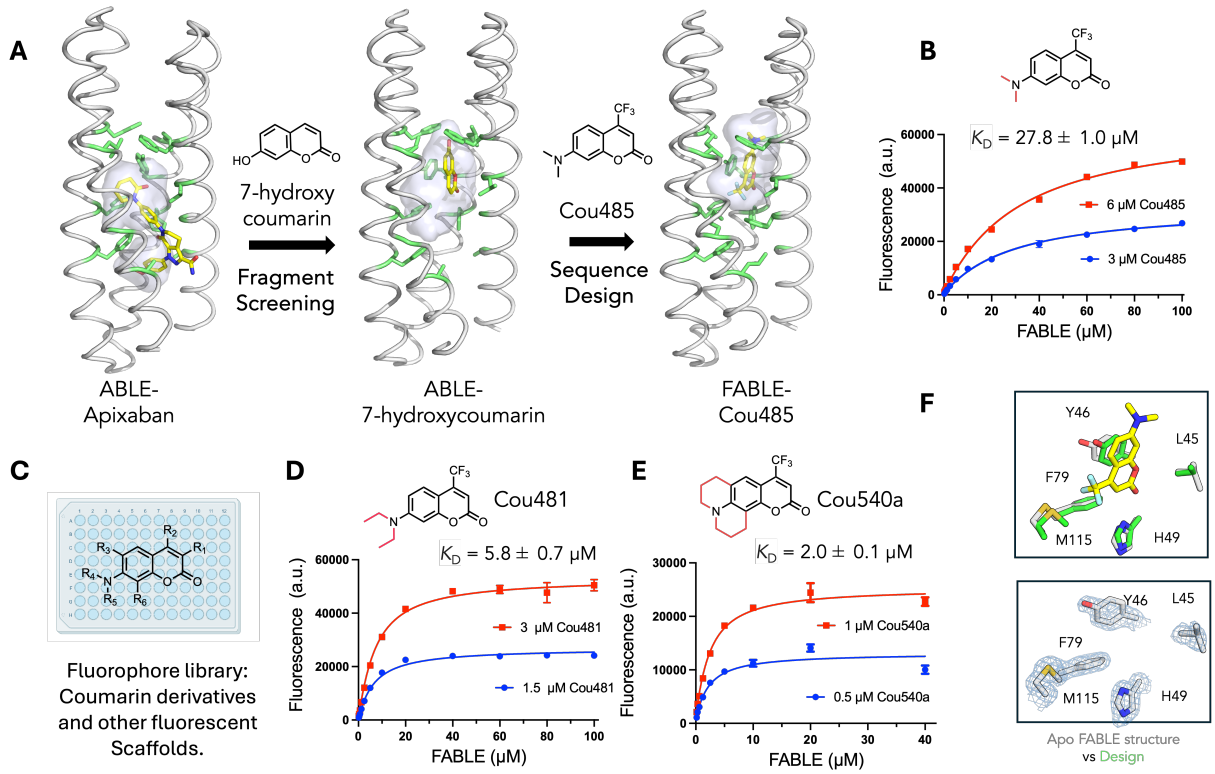

Fig. 3. Design of a fluorescent ABLE (FABLE) binding to fluorogenic coumarins. (**A**) 7-hydroxycoumarin was found from crystallographic fragment screening to bind ABLE. The **B** box (Fig. 2D) was used to design five sequences for binding to Cou485. The positions of the apixaban-interacting residues (green sticks) and the binding cavity (grey surface) show how the size and location of a binding site change as the site transitions from binding apixaban, to a small coumarin, and then to a Cou485. **(B)** A titration of FABLE into Cou485 shows a single-site binding isotherm. The dissociation constant was obtained by globally fitting a single-site binding model to data obtained by titrating FABLE into Cou485 at two fixed fluorophore concentrations, 3 and 6 μM. **(C)** Returning to the exploration of chemical space of FABLE's binding properties using a set of 37 fluorophores, including coumarin derivatives and other fluorophore scaffolds. Two additional FABLE-binding coumarin derivatives were identified. **(D-E)** The binding constants for FABLE's interaction with Cou481 **(D)** and Cou540 **(E)** were obtained at the indicated fixed fluorophore concentrations and variable FABLE concentrations as in **B**. **(F)** Upper: Overlay of the designed FABLE-cou485 complex with the uncomplexed FABLE crystal structures (PDB: 9DWC, comparison with 9DWA and 9DWB are in fig. S10). Lower: $2mF_O$-DF_C electron density (1 σ) contoured around the active site residues of FABLE (PDB: 9DWC). Error bars in B, D and E represent standard deviations of three independent measrements.

Five of the designed proteins with sequence pairwise identity ranging from 77% to 81% were selected for experimental characterization.(fig. S6) All five were helical based on far-UV circular dichroism spectroscopy and thermostable to 90 °C (fig. S7) (see section 1.4 and 1.10 of SI). They also all bound the target as assessed by fluorescence spectroscopy. The intensity of the emission spectra of Cou485 increases markedly and shifts towards lower wavelengths when bound in a rigid, hydrophobic binding site (*56*). Indeed, the fluorescence of Cou485 (6 μM) increased by 10 to 99-fold in the presence of 40 μM of the five different proteins (fig. S8). Attesting to their specificity, the starting ABLE protein did not show signs of binding to Cou485 based on the same fluorescence assay (fig. S8). Global analysis of the titration curves obtained at two fixed Cou485 concentrations and variable protein concentrations indicated that all five proteins bound Cou485 with K_D < 100 μM, and three exhibited K_D ranging from 28 μM to 38 μM (fig. S7). The design showing the most potent K_D (27.8 ±1.0 μM) was designated as FABLE (Fluorescent ABLE) (Fig. 3B) (see section 1.7 of SI).

Ligand efficiency is an empirical metric used to assess the effectiveness of a designed protein's interaction with a small molecule ligand (*57*, *58*). Large ligands have more opportunities to interact favorably, so ligand efficiency roughly normalizes for the size of the molecule by dividing the free energy of binding (1 M standard state) by the number of heavy atoms in the ligand. Most FDA-approved small molecule drugs have ligand efficiency around 0.3 kcal/(mol • heavy atom count) (*58*). The ligand efficiencies for the five proteins with Cou485 range from 0.31 to 0.35 kcal/(mol • heavy atom count) (table S1). This suggests that the quality of the interactions in the binding site is in the range of what is expected for designed small molecule interactions. To test this idea and address the question of whether FABLE had a well-defined, preorganized structure, we determined crystallographic structures of ligand-free FABLE in three different crystal forms (1.5-1.9 Å resolution) (see section 1.8 of SI). Each of the structures was in excellent agreement (< 1 Å Cα RMSD) with the designed model and the AlphaFold3-predicted structure. (Fig. 3F, figs. S9-10 and table S2).

Experimental exploration of the chemical space to probe the specificity of FABLE

Having explored sequence space to enhance specificity for Cou485 over the original apixaban, we next explored chemical space to evaluate specificity for related, larger, fluorophores. We evaluated 37 fluorophores that shared molecular features such as hydrophobicity and aromaticity (Fig. 3C and table S3) (see section 1.5 of SI). Of these compounds, only two showed a four-fold or greater increase in fluorescence intensity in the presence of FABLE, compared to their fluorescence in the presence of ABLE (fig. S11). The compounds with a large increase in fluorescence intensity were derivatives of cou485 with slightly larger apolar groups at the 7-amino position of the coumarin core (Fig. 3D-E). Fluorescence titrations showed that the dissociation constants for Cou481 and Cou540 were 5.8 ± 0.7 μM and 2.0 ± 0.1 μM, respectively (Figs. 3D and 3E), and stable by size exclusion chromatography (fig. S12) (see section 1.6 of SI).The corresponding ligand efficiencies are 0.35 and 0.34, similar to that of the original target Cou485 (0.34) (table S1). Thus, the increases in affinity for Cou481 and Cou580 were primarily driven by a larger interaction surface. The maximal fluorescence enhancement at saturating concentrations of FABLE was 48-fold for Cou485, 123-fold for Cou481, and 117-fold for Cou540 (fig. S10), suggesting that similar *de novo* proteins might be useful for future imaging and sensing applications (*8*, *59*) (fig. S12). Collectively, these results present a path for evolving new binding specificity and how related compounds can leverage an initial broad, low-affinity binding even when they were not part of the selection pressure or design calculation.

Design of an efficient Kemp eliminase

The ability of ABLE to bind small fragments suggested that its binding site might also accommodate similarly sized substrates for chemical reactions. We therefore explored whether ABLE might be redesigned to catalyze the Kemp elimination, which involves the concerted C–H deprotonation and ring-opening of 5-nitrobenzisoxazole (5NBI) to yield 2-hydroxybenzonitrile (Fig. 4A). This non-natural reaction is mechanistically similar to triosephosphate isomerase and ketosteroid isomerase (*38*, *39*), which use a carboxylate to abstract a proton from a C–H bond of their substrates. Kemp eliminase activity has also been the target of extensive studies in which the active sites of natural enzymes were first re-designed then optimized by directed evolution (*29–37*, *60*). The success rates and catalytic efficiency of such catalysts from the initial round of computational deisgn have been relatively low prior to rational redesign or directed evolution (0 – 200 $M^{-1}s^{-1}$) (*29*, *32*, *33*, *61*, *61–63*). Here we ask whether we might have a better success rate starting with a *de novo* scaffold and our knowledge of ABLE's potential binding interactions.

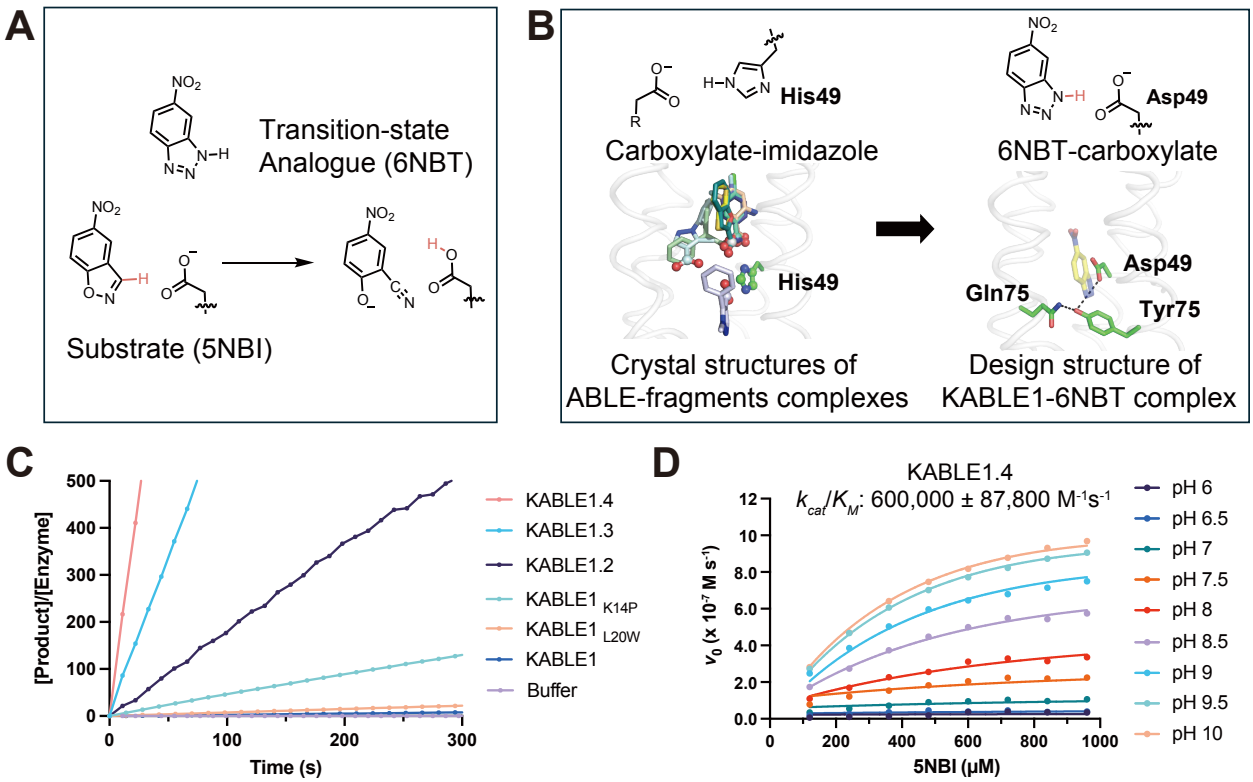

Fig. 4. Design of an efficient Kemp eliminase ABLE (KABLE) and its directed evolution. (**A**) The Kemp elimination reaction. (**B**) Fragment-inspired design of KABLE. This carboxylate-to-imidazole interaction is analogous to the carboxylate-to-isoxazole interaction at the active site of a kemp eliminase, suggesting that an active catalyst might be designed by changing His49 into an Asp. Left: Nine of the fragments contain carboxylates that bind to His49. Right: The active site was introduced into the ABLE backbone by substituting the His49 sidechain with the most frequently observed rotamer of Asp (*64*). 6NBT (sticks with yellow carbons) was positioned in the saddle point geometry of the transition state for the carboxylate-catalyzed reaction as determined by quantum mechanical calculations (*29*). Sequence design was next carried out with LigandMPNN and Rosetta FastRelax (*47*, *54*). The Asp triad (Asp49-Tyr9-Gln75) is shown in sticks. **(C)** Catalytic activity for the Kemp elimination reaction for the original sequence, designated KABLE1. Mutants arising from the combination of variants from site-saturation mutagenesis show a steady progression as more sites are included. The data are expressed as the number of turnovers (Y-axis) per unit time (X-axis). The mutations on KABLE1 are expressed at the subscript. KABLE1.2 is a KABLE1 double mutant carrying the two substitutions, Lys14Pro, and Leu20Trp. KABLE1.3 is a KABLE1 triple mutant carrying the three substitutions, Ile12Phe, Lys14Pro, and Leu20Trp. KABLE1.4 is a quadruple mutant that combines Ile12Phe, Lys14Pro, Leu20Trp, and Leu118Asn. The reaction was measured at pH 8 with a final substrate concentration of 240 μM. **(D)** Global fitting of kinetic parameters for KABLE1.4 in which the initial velocities at a series of substrate concentrations and pHs were used to fit a shared k_{cat}, K_M and pK_a. Error bars in D represent standard deviation of three independent measrements.

To design a Kemp eliminase, we targeted a transition state analogue, 6-nitro-benzotriazole (6NBT), in which the C–H group abstracted during catalysis is substituted with a stable N–H group. Similar

to previous work (*32*, *33*), we searched for backbone positions of ABLE, in which a Glu or Asp (in a low-energy rotamer) could position 6NBT in a catalytically competent orientation in the pocket delineated in fragment complexes. Leu108Glu was one site chosen because a low-energy rotamer of Glu108 placed the transition state analog inside the aromatic box (Fig. 2C) of the **A** conformer (see section 1.11.1 of SI). We also evaluated His49 as an attractive position for substitution of an Asp residue, because histidine has a similar size, shape and polarity as aspartic acid. Importantly, His49 is located near the bottom of the binding site, where it is a hotspot for interacting with carboxylate-containing fragments (Fig. 4B and fig. S13). As described in section 1.11.2 of SI, Modeling an Asp sidechain at residue 49 reverses the interactions and allows a strong hydrogen bond with 6NBT, using the Asp carboxylate's more acidic lone pairs of electrons (designated as anti) (*65*) (Fig. 4A) (see section 1.11.2 of SI). With these restraints in place, we used ligandMPNN and Rosetta FastRelax to optimize the sequence to bind 6NBT while stabilizing the conformation of either Glu108 or Asp49 (*47*, *54*). To increase their basicity, we introduced no more than one H-bond donor to the Asp49 or Glu108 carboxylates, selecting from the three possible sites for H-bonding to the side chain (*66*). Computed models were filtered based on the RMSD between the design model and that predicted for the unliganded protein computed by RaptorX (*67*) and ESM2 (*49*)(to assess preorganization), as well as their pLDDT scores (fig. S14).

We selected five proteins from each strategy for experimental characterization, with pairwise sequence identity ranging from 26% to 71% compared to ABLE (fig. S6). All of the ten proteins expressed well in soluble form (fig. S15) (see section 1.14 of SI). One of the sequences from the first strategy (**A** site) had modest catalytic activity (k_{cat}/K_M = 8 M^{-1} s^{-1} at pH 8), which is designated as KABLE0. (fig. S16) (see section 1.15 of SI) A second protein (designated KABLE1) with His49Asp as the base exhibited much greater activity in lysates, and the pH-rate profile of the purified protein had a sigmoidal shape typical of a single-site protonation (fig. S17). Analysis of the pH-rate data showed a maximal k_{cat}/K_M of 6600 ± 2100 M^{-1} s^{-1} and a pK_a 10.01 ± 0.10 (K_M = 0.99 ± 0.29 mM; Table 1, tables S4-5, figs. S17-18) (see section 1.15 of SI). An elevated pK_a for an Asp residue has previously been seen in a Kemp eliminase based on ketosteroid isomerase (*60*).

Table 1: Activities of kemp eliminases for decomposition of 5NBI.

Direct computational design			**Experimentally optimized**			**Reference**
Enzyme	k_{cat}/K_M, $M^{-1}s^{-1}$	k_{cat}, s^{-1}	Enzyme	k_{cat}/K_M, $M^{-1}s^{-1}$	k_{cat}, s^{-1}	
KE59	163	0.29	KE59 R13-3/11H	60,400	9.53	(*29*, *68*)
AlleyCat	5.8	ND	AlleyCat10	4,400	21.2	(*33*, *34*)
HG3	425	0.68	HG3.17	150,000	604	(*30*, *32*)
KABLE1[a]	**6,600**	**5.6**	**KABLE1.4[a]**	**600,000**	**800**	***This work***

[a]Error bars and methods are at table S4 and section 1.15 of SI. A more extensive table listing additional reported Kemp eliminases is in table S8.

To test that KABLE1 functioned as designed, we first mutated Asp49 to Asn, which eliminated activity (fig. S19). This finding identifies Asp49 as an essential active site residue and also supports its elevated pK_a (table S4). These findings are consistent with its placement in a hydrophobic environment as designed. Second, we tested whether the hydrogen bonding around Asp49, designed by LigandMPNN, was important. This Asp-triad (comprised of Asp49, Tyr9, and Gln75) stabilizes the carboxylate base while also forming hydrogen bonds with the substrate in the ground state and its leaving group in the transition state (Fig. 4C). Replacement of either Tyr9 and Gln75 also greatly decreased the eliminase activity of KABLE1 (fig. S19). Collectively, these findings strongly support the principles used in the design of KABLE1.
We next used saturation mutagenesis to improve the catalytic efficiency of KABLE1 from a value of k_{cat}/K_M from 6,600 $M^{-1}s^{-1}$ to 600,000 $M^{-1}s^{-1}$ (Table 1, tables S4, figs. S18 and S20). To explore the evolvability of KABLE1, we performed site-saturation mutagenesis of sidechains that line the binding site (within 5.0 Å of the substrate) (see section 1.12 -1.14 of SI). In addition, we mutated Lys14, Pro117, and Leu118 because they were proximal to slight kinks in **helices 1** and **4** that might therefore affect the positioning of key groups. Individual substitutions at four positions: Ile12Phe, Lys14Pro, Leu20Trp, and Leu118Asn increased k_{cat} by 2- to 5-fold (Fig. 4D, table S4, fig. S18). These substitutions were functionally complementary when combined (Fig. 4D, table S4, fig. S18), increasing the catalytic efficiency by two orders of magnitude in the quadruple mutant, KABLE1.4 (Table 1, Fig 4E, table S4, figs. S18). The improvement in the catalytic efficiency was primarily a result of increase in k_{cat}, with no significant change in K_M. (table S4, figs. S18).

Probing the structural and dynamic bases for KABLE's catalytic performance
To determine how these substitutions enhanced catalytic efficiency, we determined two structures by X-ray crystallography (see section 1.16 of SI). Although the high water-solubility of KABLE variants inhibited crystallization, we were able to promote crystallization by introducing substitutions on the surface of the protein. The structures of the variant containing the Lys14Pro and Leu20Trp mutants (designated KABLE1.2$_{cryst}$), which retained 50% of the enzymatic activity of the starting double mutant (fig. S21), in the absence and presence of 6NBT confirm the atomistic details of the designed interactions (< 1.1 Å Cα RMSD relative to the designed KABLE12, table S6). In particular, the hydrogen-bond network within the Asp triad is organized and Asp49 forms a strong (2.5 Å O – N distance) interaction with the transition state analog's NH group. Gln75 is also in hydrogen-bonded distance to N2 of the triazole (Fig. 5A), and the indole of Leu20Trp formed a weak hydrogen bond (3.3 Å) with the nitro group of 6NBT. Furthermore, Lys14Pro causes a deviation from ideal helix geometry, allowing the mainchain amides to form a hydrogen bond to a water molecule that is well oriented for stabilizing the substrate and transition state complexes (Fig. 5B). Similar catalytically important waters have been observed in other Kemp eliminases (*30*).

To probe the mechanism for the increase in activity between KABLE1 and KABLE1.4, we performed three independent 1µs molecular dynamics simulations for both proteins in complex with 6NBT. These simulations confirmed that the Asp49 sidechain was well situated to hydrogen bond with the NH group of 6NBT in both complexes. However, three other substrate-contacting sidechains, Gln75, Leu79, and Asn118 had increased rigidity in KABLE1.4 that appeared to quench non-productive dynamics in KABLE1.4.(Figs. 5C-5E, fig. S22). Leu79 helps position the aromatic ring of 6NBT (Fig. 5D), Gln75 is a member of the catalytic triad (Fig. 5E), and the

sidechain of the beneficial Leu118Asn mutant formed a hydrogen bond to Gln75. (Figs. 5C and S22). The MD simulations also confirmed the role of two other beneficial mutants seen in the crystal structure of KABLE1.2$_{cryst}$, including the positioning of a water molecule near a helical kink induced by Lys14Pro (fig. S23) and the hydrogen bond involving Leu20Trp (fig. S23). Finally, the mean number of water molecules in contact with 6NBT decreased markedly between KABLE1 to KABLE1.4 (Fig. 5F), consistent with the fact that the rate of the carboxylate-catalyzed Kemp elimination is increased by dehydration of the substrate and the carboxylate (*69–71*).

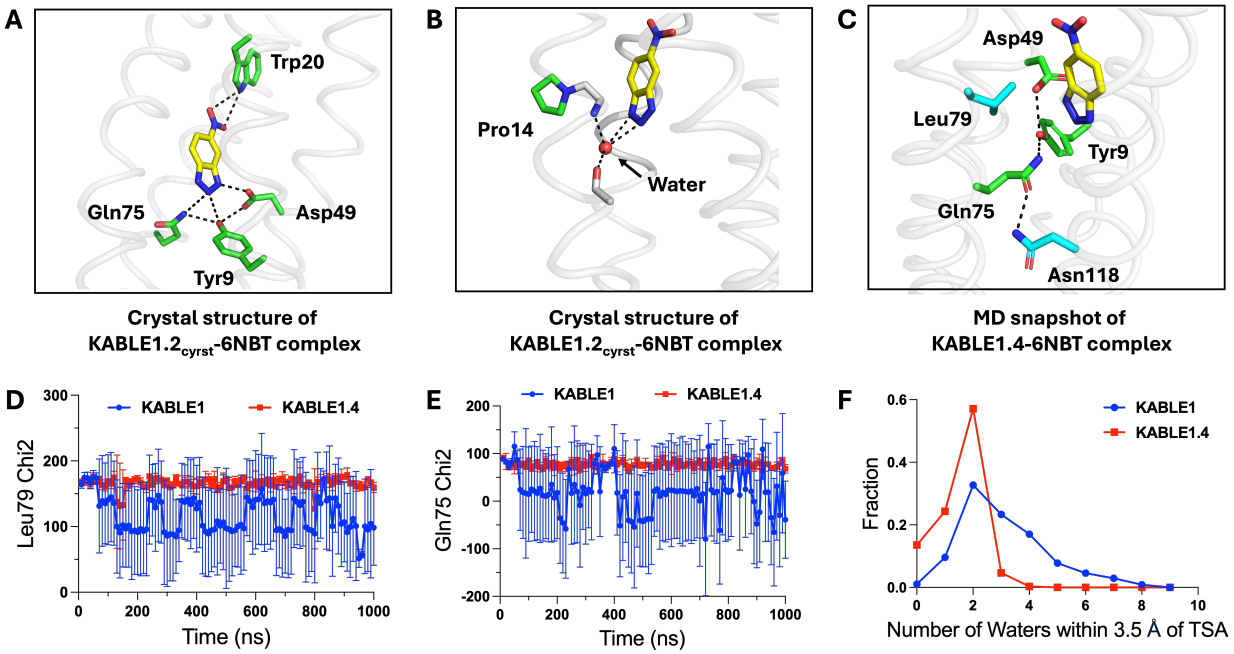

Fig. 5. The origin of KABLE's efficient catalysis probed by MD and X-ray crystallography. (**A**) Structure of the KABLE1.2cryst complex (PDB: 9N0J) showing the Asp-triad engaging the triazole and a Trp indole NH engaging the nitro group at opposite sides of the bound 6NBT. (**B**) Structure of the KABLE1.2cryst complex (PDB: 9N0J) showing Pro14 disrupts the helical geometry, thereby introducing a site to bind a water molecule, which, in turn, forms two additional interactions with the triazole. (**C**) Asp49-Tyr9-Gln75 Triad (green carbons) and key residues, Leu79 and Asn118 (blue carbons) The structure is a representative snapshot from the MD simulation of KABLE1.4 complex with 6NBT (yellow carbons). (**D**) The fluctuation of Gln75's Chi2 angle versus time during MD simulation. (**E**) The fluctuation of Leu79 Chi2 angle during MD simulation. (**F**) The number of waters within 3.5 Å of OD1 or OD2 of Asp49. Error bars represent standard deviation of three independent measrements.

Experimental exploration of the chemical space to probe the specificity of KABLE1.4

Finally, we again returned to chemical space to examine the specificity of KABLE1.4 for analogs of 5NBI. Investigations of previous Kemp eliminases showed that the value of k_{cat}/K_M for analogs of 5NBI scaled with the electron-withdrawing character of the leaving group (and hence the overall chemical reactivity of the substrate), rather than the shape and other molecular characteristics of the substrate (*60*, *68*, *72*). To determine whether this trend was also applies to KABLE1.4, we evaluated whether the rate of KABLE1.4-catalyzed elimination followed a linear Bronsted relationship over a wide range of electron withdrawing and releasing groups (section 1.17.1-1.17.2 of SI). In contrast to earlier Kemp eliminases, we found no correlation between k_{cat}/K_M vs. pK_a of

the corresponding leaving groups for a set of eight substrates (Fig. 6A and figs. S24-26, table S7). This suggests that KABLE1.4 is a specialist because k_{cat}/K_M is determined by molecular recognition and not only the intrinsic reactivity of the substrate.

Discussion: Inspired by previous evolutionary work (*1*, *5*), we combined chemical screening and *de novo* protein design to introduce new functions into a simple four-helical bundle protein. In Nature, proteins gain new activities by first binding to novel substrates with low affinity, followed by stepwise mutations to increase binding affinity and specificity. The availability of broad, low-level generalist binding activity enables the evolution of multiple specialized activities starting from a single precursor protein. Taking inspiration from this process we used crystallography to characterize ABLE's ability to weakly bind to a diverse set of fragments, followed by multi-site sequence design to convert ABLE into a specialist binding to turn-on fluorophores. While we used crystallography for screening, a number of other experimental and computational methods for fragment screening that are widely used in small molecule drug discovery (*26*, *73*), could be employed in future applications of our pipeline for protein design.

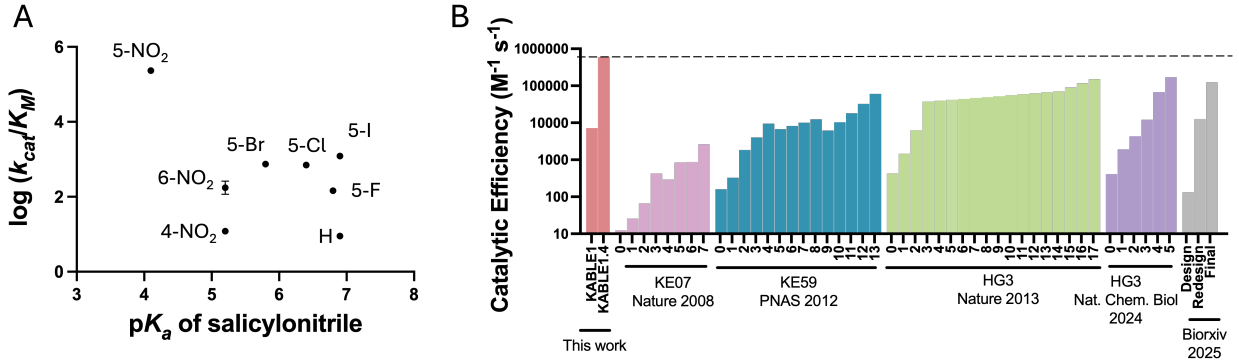

Fig. 6. Exploration of sequence and chemical space of *de novo* protein-ligand interactions for designing new functions. (**A**) Bronsted plot for ring-opening of substituted benzisoxazoles points to the unique specialist feature of KABLE1.4. Error bars stand for standard deviations. Error bars represent standard deviation of three independent measrements. (**B**) Catalytic efficiency of designed and evolved Kemp eliminases during experimental optimization. For each protein, the first to the right reflects the activity of the initial designs, which the subsequent bars reflect the activities after: combining mutants from saturation mutagenesis (KABLE); combining favorable mutants in each round of directed evolution (KE07, KE59, HG3), or computational redesign (far right).

Using larger moves in sequence space, we also converted ABLE into a Kemp eliminase KABLE1.4, which has 28 % sequence identity to ABLE. The catalytic efficiency of KABLE1.4 (k_{cat}/K_M = 600,000 M^{-1} s^{-1}, k_{cat} = 800 s^{-1}) compares favorably to the median of natural enzymes (k_{cat}/K_M = 125,000 $M^{-1}s^{-1}$, k_{cat} = 13.7 s^{-1}) (*74*) and mechanistically similar enzymes such as triosephosphate isomerase (k_{cat}/K_M = 440,000 $M^{-1}s^{-1}$) (*39*). It also compares favorably to both rationally designed (*30*, *31*, *36*, *60*, *68*) and computationally designed Kemp eliminases (*29*, *32*, *33*, *61–63*) in terms of the success rate, the catalytic efficiency of the proteins after direct design and the ease of experimental optimization to high level (Fig. 6B, Table 1, and table S8).

While Kemp eliminases were elaborated from natural protein scaffolds, the combination of a simple *de novo* scaffold and the knowledge of ABLE's binding proclivities proved to be helpful for design of a Kemp eliminase. In keeping with a first principles approach we considered a

number of features hypothesized to be important for catalysis of this reaction (*75–77*), including the need to match the template to the reaction. The active site carboxylate of the KABLE1 series of proteins is placed within a deep cavity of the protein, which enhances the dehydration and increases the basicity of the carboxylate (*69*). This placement is made possible by the high stability of ABLE in two ways: First, following the entatic (*78*) concept of a trade-off between stability and function (*79*), we used the stability of the fold of KABLE1 to force Asp49 into an apolar environment. The kinetically-derived pK_a of Asp49 is four units higher than the unperturbed pK_a of Asp in water, corresponding to a free energy cost of 5.5 kcal/mol. KABLE1's high thermodynamic stability also allowed the incorporation of four additional substitutions that were functionally beneficial but structurally destabilizing. Lys14Pro introduced a substitution that destabilizes alpha-helices by approximately 3 kcal/mol (*80*); Leu20Trp introduced a steric clash that required conformational rearrangements; and Leu118Asn replaced a hydrophobic interaction for an H-bonded interaction, which tends to be energetically unfavorable in analogous systems (*80*, *81*). Despite these changes KABLE1.4 remained highly stable (fig. S27).
This work advances at once the *de novo* design of proteins and our understanding of how proteins evolve from generalists to specialists. Here, we used: 1) information from fragment screening; 2) a deep mechanistic understanding of the reaction catalyzed (*29*, *60*, *76*, *81*), and 3) state-of-the-art computational tools (*47*, *48*, *54*) as full partners at each step of our work, from conception to realization of novel function. Thus, blending physical understanding with modern methods for computation design provides a powerful strategy for the design of sensors and catalysts.

Acknowledgments: We are grateful for helpful discussions with Sam Schneider and Hyunil Jo. We thank members of the DeGrado lab and Fraser lab for support. The synchrotron X-ray diffraction data used to determine crystal structures reported in this work were collected at beamline 8.3.1 of the Advanced Light Source (ALS) and beamlines 12-1 and 12-2 of the Stanford Synchrotron Radiation Lightsource (SSRL). We acknowledge the use of the Wynton high-performance compute cluster at UCSF.

Funding: We are grateful to National Science Foundation (CHE-2108660 and MCB- 2306190 to W.F.D.), the National Institutes of Health (R35GM122603 to W.F.D.). J.S.F is supported by a Sanghvi-Agarwal Innovation Award and NIH GM145238. Use of the SSRL, SLAC National Accelerator Laboratory, is supported by the U.S. Department of Energy, Office of Science, Office of Basic Energy Sciences under Contract No. DE-AC02-76SF00515. The SSRL Structural Molecular Biology Program is supported by the DOE Office of Biological and Environmental Research, and by the National Institutes of Health, National Institute of General Medical Sciences (P30GM133894). The ALS, a U.S. DOE Office of Science User Facility under contract no. DE-AC02-05CH11231, is supported in part by the ALS-ENABLE program funded by the NIH, National Institute of General Medical Sciences, grant P30GM124169. S.B. is the Connie and Bob Lurie Fellow of the Damon Runyon Cancer Research Foundation (DRG-2522-24). N.F.P acknowledges funding from NIH (R00GM135519).

Author contributions: Y.C., S.B., N.F.P., J.S.F., and W.F.D. formulated the project; L.B., G.J.C.and J.B. perfomed the fragment-screening, Y.C. performed the computational design and experimental characterization of FABLE; Y.C. conducted the computational design of KABLE. S.B. and Y.C. carried out experimental optimization and characterization of

KABLEs. S.B. conducted the substrate specificity study of KABLE1.4, L.B., G.J.C. and Y.C. obtained the crystal structure of the FABLEs and KABLEs. Y.C. and S.T. perfomed MD simulation. K.H., L.L. and I.B. assisted with computational design. Y.C., S.B., G.J.C., K.H., N.F.P., J.S.F., and W.F.D wrote the paper with input from all authors.

Diversity, equity, ethics, and inclusion: We are committed to fostering diversity, equity, and inclusion in our research and collaborations.

Competing interests: JSF has equity in and is a compensated consultant for Profluent Bio. Authors declare that they have no competing interests.

Data and materials availability: All data are available in the main text or the supplementary materials.

1. Materials and Methods

1.1 ABLE expression and purification

Plasmid DNA encoding His_6-tagged ABLE with a Tobacco Etch Virus (TEV) protease cleavage site for tag removal (pET11a) was transformed into BL21 (DE3) *Escherichia coli* (*13*). After overnight growth at 37°C (LB-agar, 100 µg/ml carbenicillin), single colonies were used to inoculate small-scale cultures (10 ml LB, 100 µg/ml carbenicillin). Following overnight growth at 37°C, large-scale cultures (1 L LB, 100 µg/ml carbenicillin) were inoculated and grown at 37°C until an OD600 = 0.7, at which point protein expression was induced with 0.2 mM IPTG for 4 hours at 37°C. Cells were harvested by centrifugation (4000 g, 20 min, 4°C) and cell pellets were briefly washed with phosphate-buffered saline before being re-centrifuged (4000 g, 20 min, 4°C). The cell pellets were frozen at -80°C until further purification. Thawed cell pellets were resuspended in 25 ml lysis buffer (50 mM sodium phosphate pH 7.4, 150 mM NaCl, 20 mM imidazole) and 1/2 tablet of protease inhibitor (EDTA-free complete, Roche). Cells were lysed by sonication (2 min) and cell debris was collected by centrifugation (30,000 g, 30 min, 4°C). The supernatant was filtered (0.45 µm cellulose acetate) and incubated with Ni-NTA beads (pre-washed with lysis buffer) for 4 hrs at 4°C with gentle rolling. Beads were thoroughly washed with lysis buffer before protein was eluted from the beads with elution buffer (50 mM Tris pH 8.0, 100 mM NaCl, 0.5 mM EDTA, 1 mM DTT, 300 mM imidazole). Eluted protein was supplemented with TEV protease (mass ratio: 1:10 = TEV: ABLE) and dialyzed against TEV reaction buffer (50 mM Tris pH 8.0, 100 mM NaCl, 0.5 mM EDTA, 1 mM DTT) overnight at 4°C. After tag cleavage, the protein was incubated with Ni-NTA beads (pre-washed with TEV reaction buffer) for 2 hrs and the cleaved ABLE was eluted with TEV reaction buffer. The eluted fractions were concentrated to 4 ml and further purified via HPLC (C4 reverse phase column, 30-70% acetonitrile in water). Fractions containing protein were collected and lyophilized for 72 hrs. Lyophilized ABLE was stored at -80°C.

1.2 ABLE crystallization and fragment Screening

Lyophilized ABLE was dissolved in water to a concentration of 18 mg/ml. Crystals were grown using sitting drop vapor diffusion in SwissCI 3-well plates (HR3-125, Hampton) with 200 nl protein and 200 nl reservoir (220 mM sodium malonate pH 5, 20% PEG 3350 and 3% DMSO). Needle-shaped crystals grew overnight at 19°C. We screened the 320 compound Enamine Essential fragment library against ABLE. Fragment solutions (40 nl of 100 mM stocks prepared in DMSO) were added to crystal drops using an acoustic liquid handler (Echo 650, Beckman Coulter) (*82*). Crystals were incubated with fragments for 2-4 hours before being looped and vitrified in liquid nitrogen. X-ray diffraction data were collected at beamline 8.3.1 of the Advanced Light Source (ALS) and beamlines 12-1 and 12-2 of the Stanford Synchrotron Radiation Lightsource (SSRL). Data collection strategies are summarized in **Supplementary File 1**.

Diffraction images were indexed, integrated, and scaled with XDS and merged with Aimless(*83*, *84*). In total we mounted 447 crystals soaked with fragments and were able to obtain high quality datasets from 321 crystals (resolution limit <2.2 Å based on $CC_{1/2} < 0.3$, R_{free} of initial model <35%). Replicate soaks were performed for some fragments: the total number of unique fragments with high-quality datasets was 242 (**Supplementary File 1**). We initially refined a model of ABLE against a dataset collected from a crystal soaked only in 10% DMSO. Phases were obtained by molecular replacement using Phaser (*85*) and chain A of the previously published ABLE X-ray crystal structure as the search model (PDB code 6W6X) (*13*). The initial model was improved by

iterative cycles of refinement with *phenix.refine* (version 1.21.1-5286) (*86*) and manual model building with COOT (*87*). Waters were placed automatically in early-stage refinement using *phenix.refine* into peaks in the F_O-F_C difference map >3.5 σ. In the later stages of refinement, waters were manually added/deleted, and hydrogens were refined with parameters constrained by those of the non-hydrogen atom (the riding hydrogen model). Data collection and refinement statistics are reported in **Supplementary File 1**. Coordinates and structure factor amplitudes were deposited in the PDB with accession code 9DW2. Refinement of the fragment-soaked datasets was performed using a pipeline based on Dimple as described previously using the DMSO-soaked ABLE model (PDB code 9DW2).(*88*, *89*) The pipeline consisted of initial rigid body refinement with refinement followed by two cycles of restrained refinement in Refmac: the first with harmonic distance restraints (jelly-body restraints, four cycles) and the second with restrained refinement (eight cycles).

Fragment binding was detected using the PanDDA algorithm (*90*) packaged in CCP4 version 7.0 (*91*). The background electron density map was calculated from 30 datasets (**Supplementary File 1**): six datasets were from crystals soaked in 10% DMSO and the remaining datasets came from fragment-soaked crystals where no fragment was detected. We collected multiple datasets for selected fragments. If fragments were detected in multiple datasets, we modeled the fragment with the highest occupancy based on the PanDDA event map and 1-BDC (Background Density Correction) value. Fragments were modeled into PanDDA event maps (**Supplementary File 1**) using COOT (version 0.8.9.2) (*87*) and changes in protein conformation and solvent near the fragments were modeled. Fragment restraint files were generated with *phenix.elbow* (*92*) from 3D coordinates generated by LigPrep (Schrödinger, version 2022-1) or Grade 2 (Global Phasing Ltd.). Structure refinement was performed with *phenix.refine* (version 1.20.1-4487) starting from the ABLE DMSO reference structure (PDB code 9DW2). Alternative conformations were modeled for residues when the RMSD exceeded 0.15 Å from the apo structure. The apo conformation was assigned alternative location (altloc) A and the fragment-bound conformation was assigned altloc B. Two fragments bound with alternative conformations that overlapped with the Tyr46 sidechain (PDB code 7HJK and 7HJX). For these fragments, residues 44-48 were modeled with a second conformation (altloc C). The multi-state models were initially refined with five *phenix.refine* macrocycles without hydrogens, followed by 10 macrocycles with riding hydrogens. Occupancy of the fragment- and apo-states was refined at either 2*(1-BDC) (*90*, *93*) or at fragment occupancy values from 10-90% at 10% increments. Fragment occupancy was determined by inspection of mF_O-DF_C difference map peaks after refinement. The occupancy at 2*(1-BDC) was appropriate for 41/43 fragments (**Supplementary File 1**). Coordinates and structure factor amplitudes have been deposited in the PDB with accession codes 7HIY, 7HIZ, 7HJ0, 7HJ1, 7HJ2, 7HJ3, 7HJ4, 7HJ5, 7HJ6, 7HJ7, 7HJ8, 7HJ9, 7HJA, 7HJB, 7HJC, 7HJD, 7HJE, 7HJF, 7HJG, 7HJH, 7HJI, 7HJJ, 7HJK, 7HJL, 7HJM, 7HJN, 7HJO, 7HJP, 7HJQ, 7HJR, 7HJS, 7HJT, 7HJU, 7HJV, 7HJW, 7HJX, 7HJY, 7HJZ, 7HK0, 7HK1, 7HK2, 7HK3 and 7HK4. Structure factor intensities (unmerged, merged, and merged/scaled), PanDDA input and output files including Z-map and event maps in CCP4 format, and refined models including the fragment-bound state extracted from multi-state models were uploaded to Zenodo (DOI: 10.5281/zenodo.13913848).

1.3 Computational design of fluorescent ABLE (FABLE)

With (7-hydroxylcoumarin)-ABLE structure (PDB: 7HIY) available from fragment-screening, we superimposed Cou485 to 7-hydroxycoumarin fragment based on shared heavy atoms to obtain the

initial pose, which contains the Tyr46 packing with 2H-1-benzopyran ring of coumarin and hydrogen bond between His49 and ketone of coumarin. This initial pose was used for Rosetta flexible backbone sequence design, using a previously reported script in our lab. (*44*) (Supplement text, Computational design of FABLE) During the sequence design, the side chain conformation of His49 and Tyr46 were fixed and the geometry constraint for the His49 interaction with ketone of Cou485 was applied. Out of the total 126 residues, 43 residues in the vicinity of apixaban and 7-hydroxylcoumarin binding site were chosen to be designed to reshape the binding pocket towards Cou485 while keeping the portion of the packing core of ABLE that is not involved in binding ligands unchanged. We selected the 100 best-scoring designs (lowest Rosetta energy score, using the Rosetta Ref2015 energy function) from 1000 design outputs. We next carried out structure prediction using OmegaFold (*55*) and ESMFold (*49*) to further filter out the designs whose predicted structures do not agree with the designed structures. Sequences with a less than 1.0 Å RMSD difference between the design model and prediction as well as a plDDT score over 90 were picked for detailed structural evaluation. Final sequences were selected by additional criteria: 1) No more than 2 unsatisfied side-chain hydrogen bonds in the interior of design; 2) Pre-organized binding pocket from the prediction, especially the side-chain conformation of Tyr46 and His49, which is quantified by the sub-Å RMSD of CA, CB, CG between the designed model and AF3 prediction. AF3 server (https://alphafoldserver.com) was used to predict the structures for selected designs, as indicated, although the program was not available at the time that the sequences were designed.(*48*)

1.4 Expression and purification for designed FABLE proteins

The designed FABLE proteins, with additional N-terminal His tag and TEV cleavage site, were subjected to codon optimization for *E. Coli.* using Integrated DNA Technologies (IDT) codon optimization tool. The optimized genes with additional sequences of (GTTTAACTTTAAGAAGGAGATATACAT) at 5' and (CTCGAGTGAGATCCGGCTGCTAAC) at 3' of gene were ordered as "clonal genes" from Twist Biosciences, which were assembled into pET29b vector digested with Nde1 and Xho1 using Gibbson assembly (*94*).

The plasmids were introduced into *Escherichia coli* BL21(DE3) cells (C2527H, New England Biolabs) via chemical transformation. The transformed cells were cultured in a 5 mL starter culture of Luria-Bertani (LB) medium supplemented with 50 μg ml^{-1} kanamycin at a temperature of 37°C. The starter culture was used for protein expression at 1 L LB supplemented with 50 μg ml^{-1} kanamycin. Protein expression was induced with 1 mM isopropyl β-D-1-thiogalactopyranoside (IPTG) (Apex Bioresearch Products) when the optical density at 600 nm (A_{600}) reached 0.8. After overnight expression at 30°C, the pellets were harvested by centrifugation, and their pellets were stored at -80°C.

For protein extraction, the cell pellets were resuspended in PBS buffer (119-069-13, Quality Biological) and lysed via sonication. The resulting cell lysates were clarified by centrifugation at 14,000 g for 30 min. The supernatants after centrifugation were purified with nickel-nitrilotriacetic acid (Ni-NTA) resin (Invitrogen), following the manufacturer's instruction.

After buffer exchange to PBS using PD-10 column (17085101, Cytiva), proteins were analyzed using sodium dodecyl-sulfate polyacrylamide gel electrophoresis (SDS-PAGE) and fast protein liquid chromatography (FPLC).

1.5 Screening fluorophore library with FABLE

Fluorophores dissolved in DMSO were added to FABLE in PBS to a final concentration of 38 μM FABLE and 50 μM coumarin fluorophores, including A1 to D4, whose individual structures are summarized in **Table S3**. Besides fluorophores with coumarin scaffolds, we also evaluated the interaction of FABLE with other environment-sensitive fluorophores, including L036 to TMR. Those fluorophores dissolved in DMSO were added to FABLE in PBS to a final concentration of 38 μM FABLE and 1 μM fluorophore. The fluorescence of each fluorephore was recorded with BioTek Synergy Neo2 Reader after incubating at room temperature for 30 minutes. The exact wavelength of excitation and emission for these fluorephores are in **Table S3**.

1.6 FPLC analysis

To confirm the coumarin dyes were firmly bound to the FABLE, we prepared the FABLE-coumain complexes and showed that the complexes were stable during chromatographic separation. To prepare the ligand-FABLE complex, 100 μM FABLE was mixed with 200 μM of Cou485, Cou481, and Cou540a, respectively. After incubation at room temperature for 30 min, the resulting complex was injected to the Fast Protein Liquid Chromatography (FPLC) equipped with a Superdex 75 Increase 5/150 analytical column. The ligand was monitored by their absorbance indicated in the plot (**fig. S12**).

1.7 Determining binding constants

We used fluorescence titration experiments to determine the binding dissociation constants of FABLE for Cou485, Cou481, and Cou540a with BioTek Synergy Neo2 Reader.
The excitation and emission wavelength with the largest shift upon FABLE interaction was used to quantify the the bound ligand, which is 395 nm (excitation) and 470 nm (emission) for Cou485, 410 nm (excitation) and 470 nm (emission) for Cou481, 440 nm (excitation) and 510 nm (emission) for Cou540a. For each ligand, FABLE in PBS was serially diluted while fixing the concentration of ligand at indicated values. Global fitting with 2 fixed ligand concentrations was used to fit K_D following the single-site binding model (Equation 1, N=1, L=indicated concentration, shared K_D) using GraphPad Prism. b_{free} was obtained by measuring the fluorescence of the ligand in PBS after serial dilution.

Equation 1

$$Fluorescence = b_{bound}[Ligand_{bound}] + b_{free}[Ligand_{free}]$$

- $Ligand_{total}$: total concentration of ligand
- $Ligand_{free}$: free ligand
- $Ligand_{bound}$: ligand binding to protein
- $Ligand_{free} = ligand_{total} - ligand_{bound}$
- b_{free} = brightness (fluorescence) of free ligand per μM
- b_{bound} = brightness (fluorescence) of bound ligand per μM

Equation 2

bound ligand =

$$\frac{1}{2}\left[K_{D}[Ligand_{\text{total}}] \frac{[Protein_{\text{total}}]}{N} \sqrt{\left(K_{\text{D}} + [Ligand_{\text{total}}] + \frac{[Protein_{\text{total}}]}{N}\right)^2 - 4\,[Ligand_{\text{total}}] \frac{[Protein_{\text{total}}]}{N}} \right]$$

- $Protein_{total}$: total protein concentration
- N: binding stoichiometry

- K_D: binding constant of protein-ligand interation

1.8 FABLE crystallization and structure determination

FABLE crystals were grown by sitting drop vapor diffusion using SwissCI 3-well crystallization plates with reservoir solutions containing: i) 100 mM Tris pH 8.0, 20% (v/v) MPD, ii) 200 mM sodium chloride, 100 mM CHES pH 9.5, 50% (v/v) PEG 400 or iii) 100 mM CHES pH 9.5, 30% (v/v) PEG 600. Crystal drops were set up with 200 nl reservoir and 200 nl protein. Crystals were looped and vitrified in liquid nitrogen without further cryoprotection. X-ray diffraction data were collected at SSRL beamline 12-2 (MPD condition) or ALS beamline 8.3.1 (PEG 400 and PEG 600 condition) with the strategy and data collection statistics summarized in **Supplementary File 1**. Data were reduced and models refined using the same procedure as described for ABLE, except phases were obtained for the MPD structure using molecular replacement and the previously published ABLE structure (PDB code 6W6X), while phases for the PEG 400 and PEG 600 structures were obtained using the structure from the MPD condition (PDB code 9DWA). Refinement statistics are reported in Table S1 and coordinates and structure factor amplitudes have been deposited in the PDB with accession codes 9DWA (MPD condition), 9DWB (PEG 400 condition) and 9DWC (PEG 600 condition).

1.9 Molecular dynamics (MD) simulation

1.9.1 General MD procedure

Proteins and ligands were parameterized using Gaussian09 and AmberTools's Antechamber program in Amber22(*95*, *96*). Ligand Partial charges for ligand were determined by first optimizing its geometries at the B3LYP/6-31G* level (*96*), and then calculating its electrostatic potentials using the Merz-Singh-Kollman method in Gaussian09 (*96*). Charge fitting was then performed using Antechamber's RESP program within AmberTools (*97*, *98*). All other small molecule parameters were assigned by Antechamber based on the GAFF2 database (*99*, *100*). The starting structures for the MD simulations are described in the following section. The simulation box was built by solvating protein with OPC-modeled waters (*101*) in a box with 8 Å padding from the protein, and sodium and chloride ions were added to reach a charge-neutral 137 mM NaCl concentration to match experimental conditions. Simulations began with 1,000 restrained steepest-descent minimization steps before switching to a maximum of 6,000 steps in conjugate gradient steps. The system was then heated up to 278 K over 50 ps in the NVT ensemble with Langevin thermostat control of temperature and 1 fs timestep. The simulation was then switched to the NPT ensemble, and pressure was maintained at 1 atm using the Monte Carlo barostat (*102*). Throughout equilibration steps, protein and ligand heavy atoms were initially restrained with harmonic potentials at 10 kcal/(mol·Å2) and ramped down to 0 kcal/(mol·Å2) over 9 equilibration steps, totaling 1 nanosecond. Each simulation was then carried out for an unrestrained production run under periodic boundary conditions with 2 fs timesteps. The SHAKE algorithm (*103*, *104*) was used to restrain hydrogens, short-range non-bonded electrostatic and Lennard-Jones interactions were cut off at 10 Å, and the Particle Mesh Ewald method (Ref*X13*) was used for long-range electrostatics.

1.9.2 MD for ABLE

The starting structures for the simulations were derived from the crystal structures of ABLE complexed with apixaban (PDB 6W70, chain B), and apo ABLE (PDB 6W6X, chain A) (*13*). Both

systems were prepared using the epsilon nitrogen-protonated state of H49 ("HIE"). The simulation was carried out at 278K for 2 independent runs with each run of 500 ns. The final trajectory was extracted with a 5 ns interval, which resulted in 100 states for each run of 500 ns. Chi1 and Chi2 angles of Tyr46 were extracted with an in-house script (**extract_chi1_chi2.py, supplemental text**) and manual inspection was also done to verify the calculation of Chi2 angle due to the symmetry of tyrosine sidechain. Chi1 and Chi2 of His49 were extracted with another script (**extract _chi1_chi2.py, supplemental text**). Contours were generated from the chi1-chi2 angles seen at the simulation using an in-house script (**generate_contour_from_tyr_chi1and2.py, supplemental text**) which utilizes the Gaussian kernel density estimate methods from scipy.stats module of SciPy Python Packages.

(1) MD for KABLE

The starting structures for the KABLE1simulations were derived from the design structures of KABLE1, in complex of 6NBT. For the simulation of KABLE1.4 with four mutations, Rosetta FastRelax was used to incorporate these mutations and the relaxed structures were used for MD simulation. The simulation was carried out at 300 K for 3 independent runs with Berendsen barostat and each run lasted for 1000 ns. The final trajectory was extracted with 1 ns intervals, which resulted in 1000 states for each run of 1000 ns. Chi1 and Chi2 of Gln75 and Leu79 were extracted using the script. (extract _chi1_chi2.py) The number of waters within 3.5 Å of 6NBT was calculated using the script (**count_water.py, supplemental text**)

1.10 Thermal stability

Proteins were prepared in 10 μM concentrations in PBS buffer. CD spectra were collected on a Jasco J-810 CD spectrometer in a 0.1 cm path-length quartz cuvette. The parameters for full spectra collections were set up as follows: the bandwidth was set to 2 nm, the scanning speed was set to 50 nm/min, and the average of accumulations was set to 3. Temperature-dependent data were collected at 222 nm from 20 to 95 °C with an interval of 5 °C and an increase rate of 2 °C/minute.

1.11 Computational design of KABLE (Kemp Eliminase)

Our goal was to use the information from the fragment complexes to inform the design of the active site. As the substrate was a bicyclic aromatic compound, it was logical to position it into the aromatic boxes of the A site, hosting 8 bicyclic fragments. This was followed by searching for a Glu or Asp sidechain that was well positioned to abstract a proton from the substrate to catalyze the elimination reaction (Strategy 1). The second strategy centered instead on using the information from fragment complexes to first identify a catalytically favorable position for a Glu/Asp transition state complex, followed by redesign of ABLE's binding site to stabilize the bicyclic ring, primarily through hydrophobic, aromatic interactions and van der Waals interactions.

In each case we considered theoretical suggestions that emphasize the location of a binding site relative bulk solvent. As early as 1967 Perutz stated: "The non-polar interior of enzymes provides the living cell with the equivalent of the organic solvents used by the chemists. The substrate may be drawn into a medium of low dielectric constant in which strong electric interactions between it and specific polar groups of the enzyme can occur." Thus, it is important to consider placement of the base in a pre-organized, solvent-inaccessible location well below the surface of the protein. This principle has been supported by a body of theoretical and computational studies, as well as through careful examination of evolved Kemp eliminases.(*30*, *32*, *33*, *70*) We satisfied Perutz's this principle by choosing designs in which the carboxylate base and the substrate were fully

inaccessible to a water-sized probe, the surrounding sidechains should be primarily hydrophobic (*32*, *61*) and the geometry of the carboxylate should be close to the saddle point for the computed transition state of the reaction.

1.11.1 Strategy 1: Aromatic box

Inspired by the aromatic boxes of conformer A, we used a similar procedure for design of a Kemp Eliminase. For the aromatic box in conformer A, we used 7HJQ as the starting structure. The plane of the ring of 6NBT was oriented as in 7HK4. The next step was to identify a position for incorporation of the active site Asp or Glu to satisfy the following criteria: **1)** When in a low-energy rotamer, its carboxylate should form a hydrogen bond to N3 of 6-nitrobenzotriazole (6NBT) in a geometry computed from previous quantum calculations (*29*, *105*, *106*) **2)** The benzisoxazole ring of the substrate should be fully buried (to increase the basicity of the carboxylate). Thus, the Asp/Glu carboxylate should be solvent-inaccessible. We also filtered out any examples where the C-alpha of the acidic residue is located at a surface position, but the sidechain reaches into the protein interior, because the burial of the carboxylate would need to compete with solvation. **3)** The introduced sidechain should not clash with the backbone or sidechains of the residues comprising the aromatic box. This left 3 positions to explore, namely 108, 112 and 115. After searching through low-energy sidechain rotamers of Asp and Glu at these locations, Glu at position 108 was found to uniquely fulfill these criteria. The resulting complex was used as an input structure for sequence design with either an 1) an iterative round of LigandMPNN (*47*) and Rosetta FastRelax (*54*) or a 2) classical flexible backbone Rosetta sequence design (*54*).

1) For iterative rounds of LigandMPNN and Rosetta FastRelax route, residue 46 was fixed to either Y or W and residue 86 was fixed to F to maintain the aromatic packing interactions discovered in fragment screening. In the Rosetta FastRelax step, geometric constraints from the reported crystallographic conformation sampling were applied (**supplementary text, constrain for active site 1 of kemp eliminase**).(*107*)
2) The second sequence design of the flexible backbone Rosetta sequence design proceeded with the same constraint applied (**supplementary text, constrain for active site 1 of kemp eliminase**) following the reported protocol from our lab (*44*).

Structure prediction with RaptorX was carried out for all designed sequences (*67*, *108*), to ensure that the designed structures would be preorganized to adopt the same active site geometry of the design model. Of 2000 sequences evaluated on 1), we chose designs (1, 4 and 5). Of 2000 sequences evaluated on 2), we chose designs 2 and 3. The selection criteria were the sub-Å backbone RMSD between designed complex and the predicted unliganded structures and also agreement of sidechain conformation of active site (108, 46, 79, 86) between design and prediction.

1.11.2 Strategy 2: Hotspot residue 49

In strategy 2 we focused on identifying a site that was well-positioned to accommodate a Glu/Asp as the general base. His49 was selected as a potentially ideal position, because it was situated at a central location near the bottom of the binding site where it donated a hydrogen bond to a carbonyl of apixaban in ABLE. His49 also formed hydrogen bonds to 35% fragments binding at the pocket of ABLE, and it formed imidazole-carboxylate salt bridges in 9 of the complexes, as well as with acetate in 6W6X (**fig. S13**). We reasoned that it should be possible to reverse the polarity of the interaction by replacing the His with an Asp, which is nearly isosteric to histidine, as this would place the sidechain in a good environment to form a strong hydrogen bond. 6NBT was docked to

the Asp49 of ABLE-fragment crystal structures (PDB: 7HJV) based on previously reported geometric constraints from DFT calculations, considering the more basic (trans) lone pairs of electrons on either OD1 or OD2 for proton abstraction(*29*).
All 3 resulting poses (**fig. S13**) were used as input structures for sequence design with 3 iterative rounds of LigandMPNN and Rosetta FastRelax, resulting in 1000 designs per input pose. In the Rosetta FastRelax step, geometric constraints from the reported crystallographic conformation sampling were applied (**supplementary text, constrain for versatile residue 49 of kemp eliminase**) (*107*). Structure prediction with RaptorX was carried out for all designed sequences (*67*, *108*). Five designs were picked based on the goodness of fit between the predicted model of the uncomplexed structure versus the design model for the complex as described in the section above.

1.12 Library design

The plasmid encoding the KABLE1 gene was used as the template for site-specific saturation mutagenesis, which was achieved using megaprimer PCR protocol with primer sets (Integrated DNA Technologies) that overlapped the 5' position of the randomized position, together with a flanking primer (T7 reverse). Saturation mutagenesis was performed using NNK codons (where N can be any base and K represents a mixture of G and T nucleotides) that cover the 20 genetically encoded amino acids (primer sequences were shown in **table S9**). There are 20 libraries with NNK codon at indicated residue (**table S9**). The size of the PCR product was checked using agarose gel (1%) electrophoresis. Product DNA was digested with DpnI (New England Biolabs) at 25 °C for 12-14 hours to eliminate the parental clone. The sample was transformed into *E. coli* NEB5α cells (C2987H, New England Biolabs) and plated on an LB agar plate containing kanamycin (50 µg ml^{-1}). Colonies obtained from the plate upon incubation at 37 °C for 12-14 hours were grown in LB media with kanamycin at 37 °C for 2-3 hours. Cells were collected by centrifugation at 6,500*g* for 10 min. Plasmids were extracted using a DNA plasmid extraction kit following the manufacturer's protocol (Monarch, New England Biolabs). Library quality was confirmed by Sanger sequencing (Azenta Life Sciences).

1.13 Library screening

Around 160 randomly picked independent colonies were screened for each library. The plasmid encoding the NNK library was transformed into *E. coli* BL21 cells and plated on LB agar containing kanamycin. Individual colonies were inoculated in LB media (200 µl) containing kanamycin in a 96-well plate. Cultures were incubated at 37 °C, 220 rpm for 5-6 hours. A replica deep 96-well plate (Costar) was generated, where cultures (20 µl) were inoculated in LB media (400 µl) containing kanamycin and IPTG (0.5 mM). Cultures were then allowed to grow at 30 °C, 220 rpm for 20 h. Cells were collected by centrifugation at 4 °C, 2,000*g*. Pellets were resuspended in buffer A (25 mM Tris, pH 8.0, 20 mM imidazole, 300 mM NaCl), centrifuged again, and the supernatant was discarded. Cells were lysed using a buffer containing 25 mM Tris, pH 8.0, 100 mM NaCl, 0.5% triton X and centrifuged to separate the supernatant. Kemp eliminase activity of the clones was tested using a 96-well plate in the buffer (20 mM Tris, pH 8.0, 100 mM NaCl) containing 1.5% acetonitrile. Reactions were initiated upon mixing cell lysate with 100 µM substrate in a 1:1 ratio (final substrate concentration of 50 µM). Product formation was observed by measuring absorbance at 380 nm at 25 °C on a plate reader for 10 min. The activities of the clones showing notable improvement in activity over the initial design were confirmed by rescreening them in triplicate. Plasmids extracted from the colonies demonstrating enhanced

activity were sequenced (Azenta Life Sciences) to determine the identities of beneficial mutations. Sequences of the design (KABLE1) as well as the final quadruple mutant (KABLE1.4) are provided in **table S10**.

1.14 Expression and purification of KABLEs

The plasmids encoding KABLE0, KABLE1, and its mutants, cloned into pET29b(+) vector with NdeI and XhoI restriction sites, were transformed into *E. coli* BL21(DE3) (C2527H, New England Biolabs) and plated on LB agar plate with 50 µg ml^{-1} kanamycin (Thermo Scientific). This same kanamycin concentration was used throughout the experiment. Single colonies were inoculated into 15 mL LB medium containing kanamycin and grown at 37 °C, 220 rpm for 5-6 hours. 10 ml of starter culture was then diluted into 1 L of LB with kanamycin and allowed to grow at 37 °C until A_{600} reached 0.6-0.8. The culture was induced upon the addition of 0.5 mM isopropyl-ß-D-1-thiogalactopyranoside (IPTG) (Apex Bioresearch Products) and grown at 30 °C for 20 hours. Cells were harvested by centrifugation (Sorvall Legend RT+, Thermo Scientific) at 4 °C, 4, 3500 rpm for 15 min., flash frozen in liquid nitrogen, and stored at -80 °C.

For protein purification, 200 mL cells were resuspended in 40 mL buffer A (25 mM Tris, pH 8.0, 20 mM imidazole, 300 mM NaCl). Cell lysis was done upon sonication (Sonic Dismembrator Model 500, Fisher Scientific) for 10 min. (20 s pulse, 20 s rest) at an amplitude of 30%. To isolate the soluble fraction, centrifugation was performed at 4 °C, 20,000*g* for 30 min. The lysate was loaded onto a Ni-NTA gravity column (Hispur, Thermo Scientific) pre-equilibrated with buffer A, washed, and eluted using buffer B (25 mM Tris, pH 8.0, 250 mM imidazole, 300 mM NaCl). Protein fractions identified by Bradford assay were combined, concentrated to 3 ml using 10K MWCO spin concentrator (Amicon Ultra, Millipore Sigma), and exchanged into TEV cleavage buffer (50 mM Tris, pH 8.0, 75 mM NaCl) using desalting column (BioRad, 10 DG). TEV protease (at protein-to-protease absorbance (A_{280}) ratio of 100:1) along with EDTA (0.5 mM) and DTT (1 mM) was added to cleave the N-terminal His_6-tag. Protein was incubated at 37 °C for 12-14 hours and exchanged into buffer C (20 mM HEPES, pH 7.0, 100 mM NaCl). Protein fractions were then passed through Ni-NTA column to remove the protease and any un-cleaved KABLE protein**.** Final purification was performed on GE Healthcare AKTA FPLC system with Superdex 75 Increase 10/300 column in buffer C. Protein concentrations were determined by measuring the absorbance at 280 nm using extinction coefficient determined by Expasy ProtParam tool (https://web.expasy.org/protparam/).

1.15 Kinetic characterization

The initial rates for Kemp elimination for all the kinetic assays were corrected for the background rates in the appropriate buffers without the enzyme. Product (2-hydroxy-5-nitro-benzonitrile) concentration was determined using an extinction coefficient of 15,800 $M^{-1}cm^{-1}$ at 380 nm. The individual kinetic parameters (k_{cat}, K_M, and pK_a) were determined by globally fitting the dependence of initial rates on both substrate concentration and assay pH. Substrate 5-nitrobenzisoxazole (5NBI, AK Scientific) concentration ranging from 100 µM to 1 mM and assay pH ranging from pH 6 to pH 10 were used. The substrate 5NBI was prepared in acetonitrile as 100 mM stock, which was further diluted in buffer to prepare working solutions of various substrate concentrations at each tested pH. To maintain the pH at different values, different buffers were used at 20 mM in the presence of 100 mM NaCl (MES at pH 6.0 and 6.5, HEPES at pH 7.0 and 7.5, Tris at pH 8.0 and 8.5, CHES at pH 9.0 and 9.5, and CAPS at pH 10.0). The reactions were initiated by mixing the enzyme in buffer and solutions of 5NBI in a 1:3 ratio in a 96-well plate

(Genesee Scientific). The final reaction mixtures contained enzyme (5-1000 nM, depending on the activity of the mutant) in buffer, 1.5% acetonitrile (to maintain the constant final concentrations of the substrate), and variable concentrations of substrate at its pH-specific buffer. Product formation was monitored on a plate reader (BioTek Synergy neo2, Serial: 22052011) at 25 °C for 10 min. with the minimum kinetic interval determined by manufacturer provided software (Gen 5, version 3.12).

For KABLE family of proteins, its $k_{cat,}$ K_M, and pK_a were fitted based on equation 3 where a pH-titratable catalytic base was considered in the reaction process. For a given protein, its initial velocities from a series of substrate concentrations and assay pHs were used to fit a shared set of $k_{cat,}$ K_M, and pK_a value for all these data using GraphPad Prism 9.3.1. A pH range covering the pKa $\pm$ 2 was used for each KABLE variant. No pH higher than pH 10 was used because of the increased background decomposition of 5NBI. To capture the initial velocity of KABLEs, less enzyme concentration was used for ones at higher pH and more active ones as summarized in **Table S5**. The data conform well to equation 3, and the least squares fit returned unique values of $k_{cat,}$ K_M, and pK_a for all tested proteins, except for KABLE1$_{K14P}$, KABLE1.2, KABLE1.3, and KABLE1.4. Although the values of k_{cat}/K_M were well-defined for these proteins, there was some covariation of the values for k_{cat} and K_M. Therefore, a single parameter (k_{cat}) was held constant, allowing the value of the pK_a and K_M to vary. A range of fixed k_{cat} was tested to find the k_{cat} allowing the maximal R-square > 0.99). As in **fig. S19**, the reported k_{cat} enables the best fit (maximal R-square) across a wide range of tested $k_{cat,}$ and the R-square decreases as the fixed k_{cat} moves away from the reported value. The value of K_M and pK_a were directly taken from the fitting with the reported k_{cat} held a constant based on the R-square analysis. For this set of KABLEs, its standard error of mean of k_{cat} was obtained by taking the highest ratio of standard error of mean to mean of the fitted k_{cat} among all the tested enzymes, considering that there may be more error for the values of the of k_{cat} from R-square analysis.

Besides globally fitting kinetic paramters and pK_a, we also fit the kinetic parametrs and pK_a using the individual kinetic parameters fitted at each pH as in reference (*60*) for KABLE1 and its most active variant, KABLE1.4. Specifically, for each pH, the initial rate, under a series of substrate concentrations, was used to fit the k_{cat} and K_M using the Michaelis-Menton equation in GraphPad Prism. The dependence of k_{cat}/K_M and k_{cat} on pH was fitted using the equation $k_{cat}/K_M = (k_{cat}/K_M)_{EH} \times (1-f_{E-}) + (k_{cat}/K_M)_{E-} \times f_{E-}$, in which f_{E-} is the fraction of the protein in the anionic state and is related to pH by: $f_{E-}=1/(1+10^{pKa-pH})$. Similarly, $k_{cat} = (k_{cat})_{EH} \times (1-f_{E-}) + (k_{cat})_{E-} \times f_{E-}$.

The values of $(k_{cat}/K_M)_{E-}$, $(k_{cat})_{E-}$ and pK_a are indicated in **fig. S17**. The values of $(k_{cat}/K_M)_{E-}$ and pK_a from this treatment agree with the k_{cat}/K_M from global fitting of all the variable substrate and pH data. The value of $(k_{cat})_{E-}$ is aound 3 times lower than the value obtained from global fitting (the values of K_M covaried, to keep k_{cat}/K_M constant). Considering the co-varibility of k_{cat} and K_M at individual pH, we used global fitting as our primary method to report kinetics parameters and p$K_{a.}$

Reaction process of Kemp elimination:

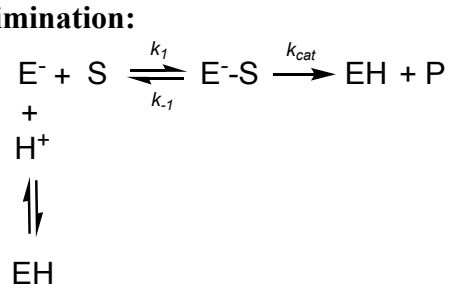

From Classical Michaelis-Menten Equation: $K_M=\frac{k_{-1}+k_{cat}}{k_1}$ $V_0=\frac{k_{cat}\cdot[E^-]\cdot S}{K_M+S}$

Incorporation of pH-titratable base: $K_a=\frac{[E^-][H^+]}{EH}$ $E_t=E^-+E^--S+EH$

Equation 3

Final Expression of V_0:

$$V_o=\frac{k_{cat}\cdot E_t\cdot S}{(K_M+S)(1+\frac{S}{K_M}+10^{(pK_a-pH)})}+c$$

- E*t* is the total concentration of enzyme.
- pK_a is the pK_a of the titratable catalytic base.
- c is the baseline correction.

1.16 KABLE crystallization and structure determination

LigandMPNN chose very polar and flexible surface residues for KABLE, which impeded crystallization. To improve the crystallization of KABLE1.2, we introduced 23 surface mutations to make KABLE12$_{cryst}$. Because ABLE crystallizes easily, we transplanted its surface residues to KABLE12$_{cryst}$ as indicated in **fig. S21**. Following the previous expression and purification procedures, both the histag-cleaved version and histag-uncleaved version at PBS buffer were used to screen crystals and prepare the complex with 6NBT. 100 mM 6NBT dissolved in DMSO was added to 2.5 mM KABLE12$_{cryst}$ for the final 6NBT concentration of 10 mM.

Apo crystals of KABLE12$_{cryst}$ with an intact His-tag were grown by sitting-drop vapor diffusion using SwissCI 2-well crystallization plates with reservoir solution containing 0.2 M sodium bromide, 0.1 M Bis-Tris propane pH 6.5, 20% PEG 3350. Crystals of KABLE12$_{cryst}$ in complex with 6NBT grew using His-tag cleaved protein from a reservoir containing 0.2 M zinc acetate, 0.1 M sodium cacodylate pH 6.5, 18% PEG 8000. Crystals were looped and vitrified in liquid nitrogen without further cryoprotection. X-ray diffraction data were collected at ALS beamline 8.3.1 with the strategy and data collection statistics summarized in **Supplementary File 1**. Data were reduced and models refined using the same procedure as described for ABLE. For the structure in complex with 6NBT, ligand restraints were generated with *phenix.elbow* (for 6NBT) and Grade2 (for cacodylate) (*92*). In addition to the 6NBT molecule present in the KABLE core, two additional 6NBT molecules were identified in complex with three zinc molecules and a cacodylate ion at a crystal packing interface (**fig. S28**). The metal identity was supported by the calculation of an anomalous difference density map showing large peaks for the zinc atoms and no peak for the cacodylate arsenic (**fig. S28**). B-factors for the zinc atoms were refined anisotropically to account for the observed disorder (**fig. S28**).

1.17 Specificity study of KABLE1.4 with different benzisoxazoles

1.17.1 pK_a determination

2-Hydroxy-5-iodo-benzonitrile and 2-Hydroxy-5-amino-benzonitrile substrates were obtained from A2B Chem. 100 mM stock solution of 2-hydroxybenzonitrile derivative was prepared in acetonitrile, which was subsequently diluted to 1 mM. 100 mM buffer solutions at various pH ranging from pH 3.0-10.0.0 were prepared: citrate (pH 3.0-5.8); MES (pH 6.0-6.5); HEPES (pH 6.8-7.8); TRIS (pH 8.0-9.0); CHES (pH 9.3-10.0) in presence of 100 mM NaCl. Substituted 2-

hydroxybenzonitrile (1 mM) was further diluted by 10-fold with buffer solutions and absorbance was measured using UV-Vis spectrophotometer (Agilent 8453). Absorbance at the wavelength maxima (λ_{max}) was plotted versus pH using Kaleidagraph (Synergy Software, v 5.0.6) to obtain the pKa of the corresponding 2-hydroxybenzonitrile. All measurements were performed at 22 ºC.

1.17.2 Kinetic characterization of KABLE1.4 for decomposition of different benzisoxazoles

The initial rates for Kemp elimination for all the kinetic assays were corrected for the background rates in buffer without the enzyme. Product concentration for the substituted benzisoxazoles was calculated using experimentally determined extinction coefficient at the respective wavelength maximum as mentioned in **table S7**. Catalytic efficiency (k_{cat}/K_M) as well as individual kinetic parameters (k_{cat} and K_M, where applicable) were determined by fitting the dependence of initial rates on substrate concentration ranging from 100 μM to 1 mM to the Michaelis-Menten equation $v_0 = k_{cat}[E][S]/(K_M+[S])$, where v_0 is the initial velocity, [E] and [S] are enzyme and substrate concentrations, respectively. Enzymes with high K_M values, where substrate saturation could not be achieved due to substrate solubility limits, catalytic efficiency was determined by fitting data to $v_0 = k_{cat}/K_M\,[E][S]$. All the substrates were prepared in acetonitrile as 100 mM stock, which was further diluted in buffer (20 mM HEPES, pH 7.0, 100 mM NaCl) to prepare working solutions of various substrate concentrations. The reactions were initiated by mixing enzyme in buffer and substrate solutions in 1:3 ratio in 96-well plate (Genesee Scientific). The final reaction mixtures contained 1 μM enzyme in buffer, 1.5% acetonitrile (to maintain the constant final concentrations of the substrate), and variable concentrations of substrate. Product formation was monitored on a plate reader (BioTek Synergy neo2, Serial: 22052011) at 25 °C for 15 min. with the minimum kinetic interval determined by manufacturer provided software (Gen 5, version 3.12).

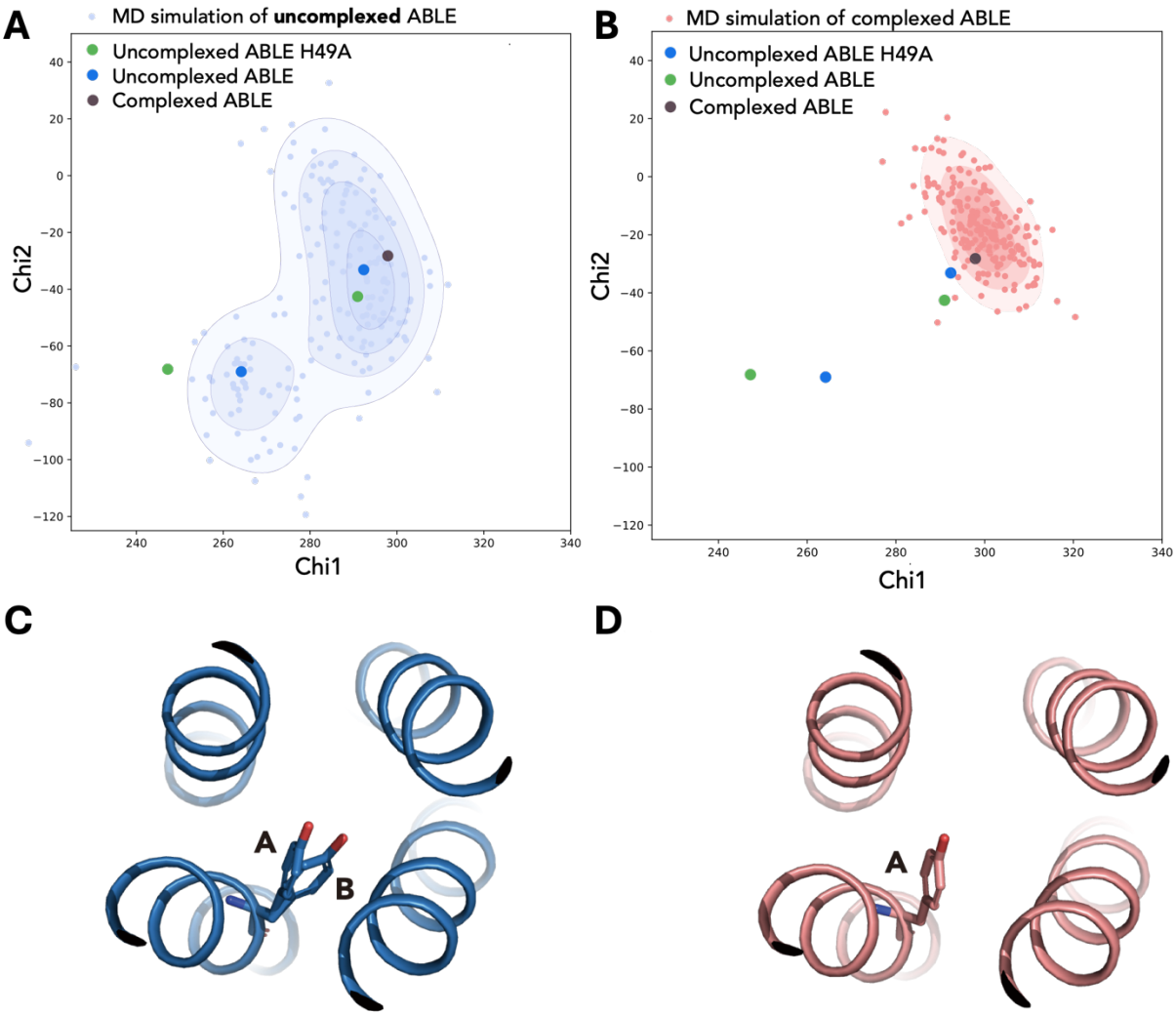

Fig. S1. Contour map of Tyr46 side chain conformation of ABLE from molecular dynamics simulation. (**A**&**B**) Dynamics of uncomplexed ABLE (PDB: 6W6X) and ABLE-apixaban (PDB: 6W70) were explored by doing molecular simulation at 278 K for 500 ns with amber. Chi1 and Chi2 from each state of these simulations and reported crystal structures of ABLEs (6W6X: uncompleted ABLE; 6W70: ABLE-Apixaban Complex; 6X8N: uncomplexed ABLE His49Ala) were extracted for plotting. Contours were generated from the points of uncomplexed ABLE (**A**) and ABLE-apixaban complex contours were generated using an in-house script that utilizes the Gaussian kernel density estimate methods from scipy.stats module of SciPy Python Packages. (**C**&**D**) **A** and **B** conformations of Tyr46 sidechain were present in the uncomplexed ABLE crystal structure (PDB: 6W6X) while only A conformation of Tyr46 sidechain conformations was present at ABLE-apixaban complex(PDB: 6W70).

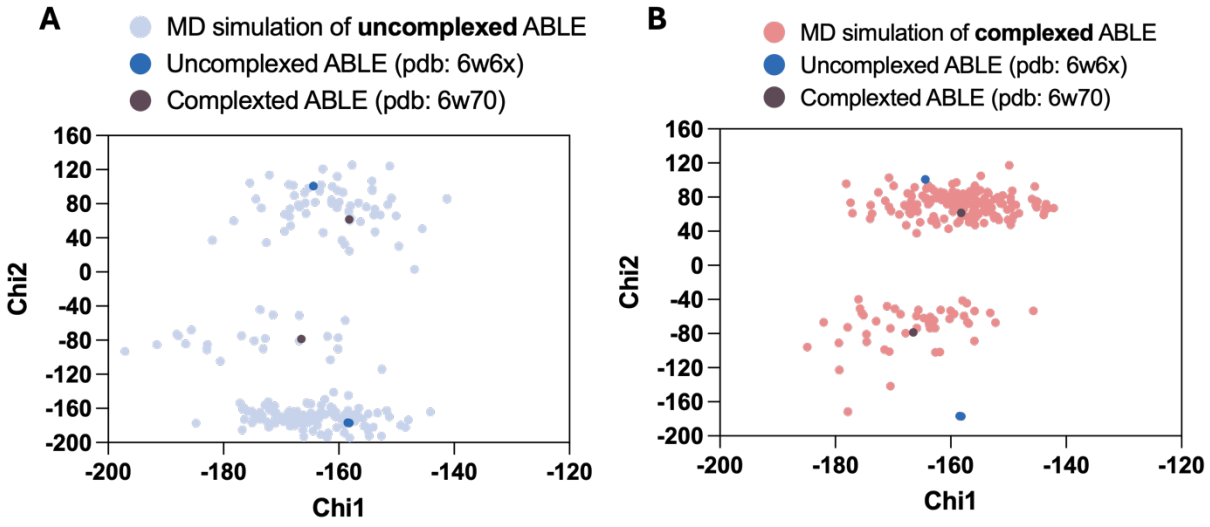

Fig. S2. Contour map of His49 side chain conformation of ABLE from molecular dynamics simulation. (**A**-**B**) Dynamics of uncomplexed ABLE (PDB: 6W6X, **A**) and complexed ABLE (PDB: 6W70, **B**) were explored by doing molecular simulation at 278 K for 500 ns with amber. Chi1 and Chi2 of His49 from each state of these simulations and reported crystal structures of ABLE were extracted for plotting.

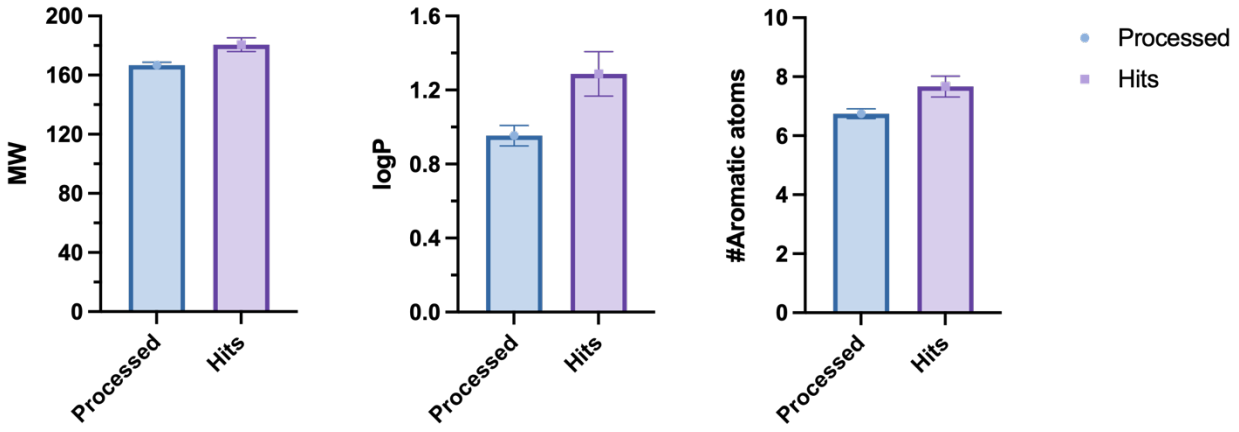

Figure S3: Chemical properties of fragments in the processed diffraction dataset and hits binding at apixaban-binding pocket of ABLE. For each chemical, its MW, logP and the number of aromatic atoms were generated using "calculate properties" function of DataWarrior. The error bars represent standard error of mean. Processed: n=242; Hits: n=39. Z scores are all over 3.

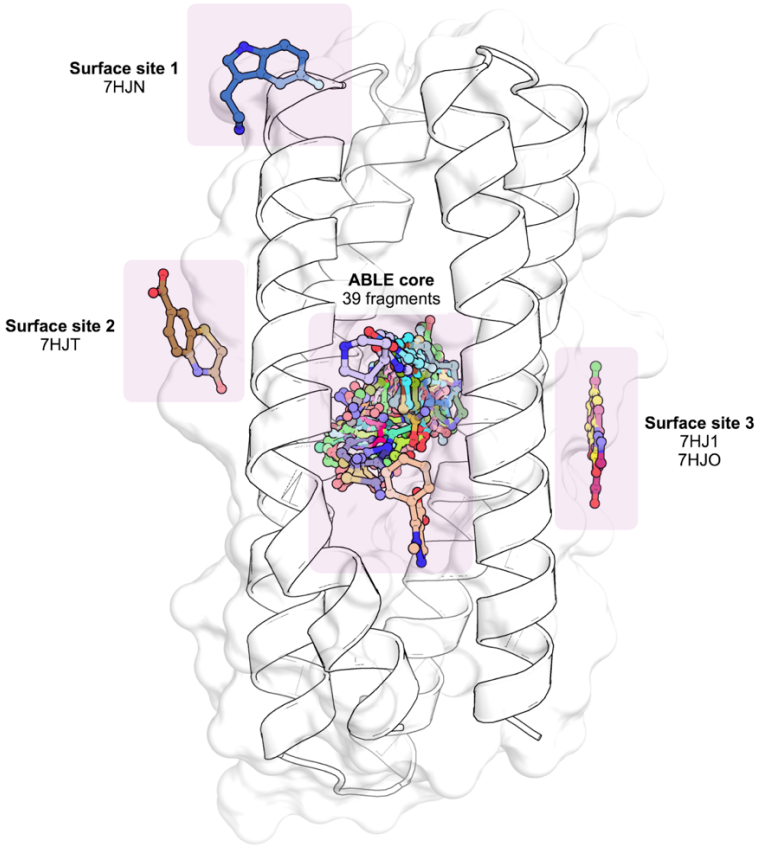

Figure S4: X-ray crystal structure of ABLE showing binding sites for 43 fragments. The structure of apo ABLE (PDB: 9DW2) with white cartoon and transparent white surface.

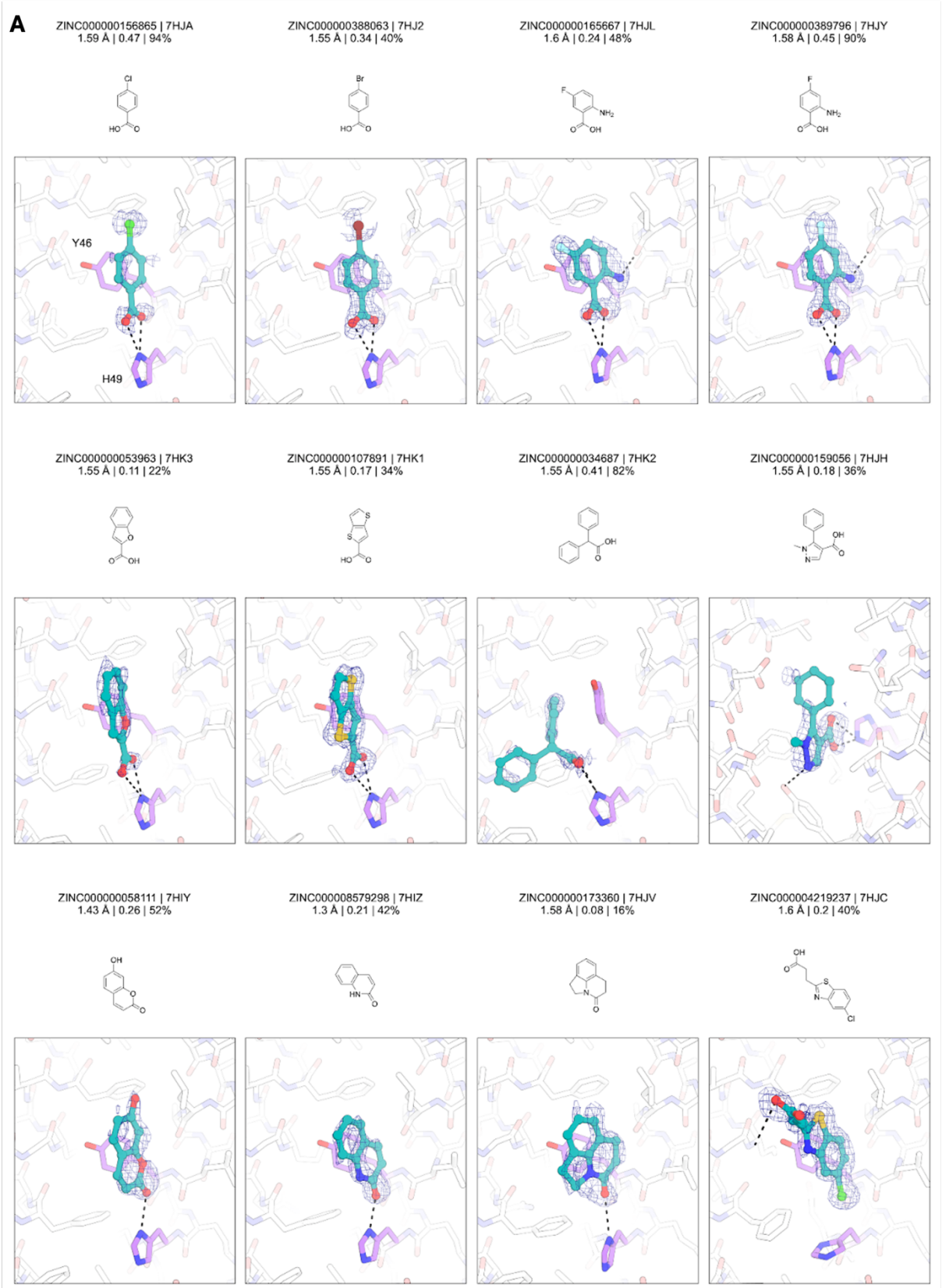
A
ZINC000000156865 | 7HJA
1.59 Å | 0.47 | 94%
ZINC000000388063 | 7HJ2
1.55 Å | 0.34 | 40%
ZINC000000165667 | 7HJL
1.6 Å | 0.24 | 48%
ZINC000000389796 | 7HJY
1.58 Å | 0.45 | 90%
Y46
H49
ZINC000000053963 | 7HK3
1.55 Å | 0.11 | 22%
ZINC000000107891 | 7HK1
1.55 Å | 0.17 | 34%
ZINC000000034687 | 7HK2
1.55 Å | 0.41 | 82%
ZINC000000159056 | 7HJH
1.55 Å | 0.18 | 36%
ZINC000000058111 | 7HIY
1.43 Å | 0.26 | 52%
ZINC000008579298 | 7HIZ
1.3 Å | 0.21 | 42%
ZINC000000173360 | 7HJV
1.58 Å | 0.08 | 16%
ZINC000004219237 | 7HJC
1.6 Å | 0.2 | 40%

ZINC000000404314 | 7HJI
1.55 Å | 0.24 | 48%

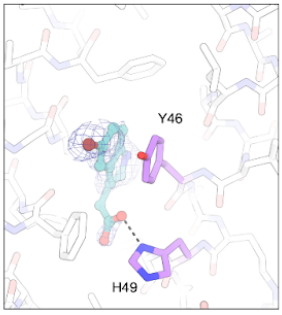

ZINC000006657973 | 7HJ0
1.39 Å | 0.37 | 74%

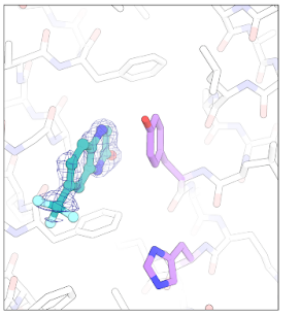

ZINC000017744334 | 7HJQ
1.58 Å | 0.19 | 38%

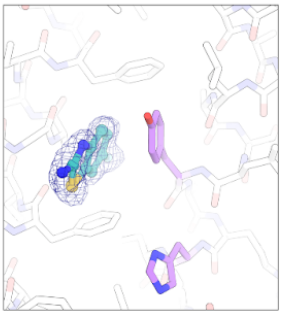

ZINC000000162015 | 7HJ4
1.57 Å | 0.31 | 62%

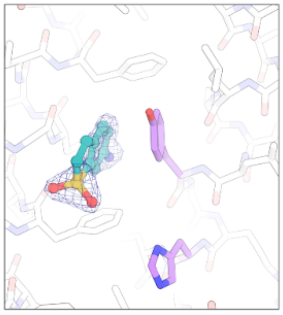

ZINC000001612349 | 7HJ5
1.55 Å | 0.21 | 42%

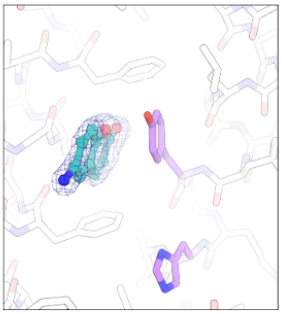

ZINC000016697555 | 7HJZ
1.6 Å | 0.35 | 70%

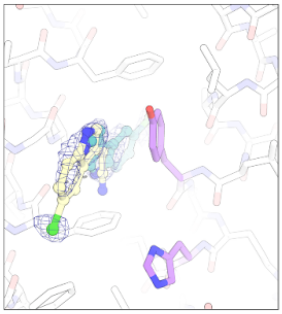

ZINC000004774482 | 7HK0
1.59 Å | 0.21 | 42%

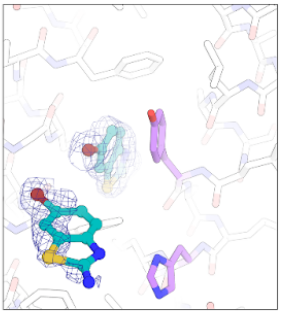

ZINC000038866729 | 7HK4
1.59 Å | 0.14 | 28%

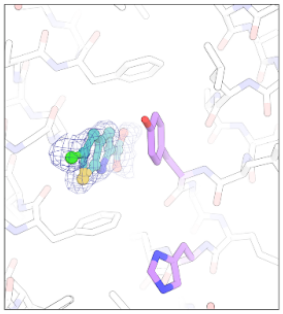

ZINC000001394131 | 7HJG
1.57 Å | 0.26 | 52%

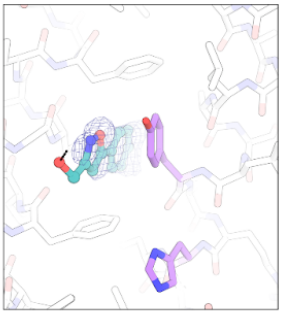

ZINC000000158815 | 7HJJ
1.59 Å | 0.43 | 86%

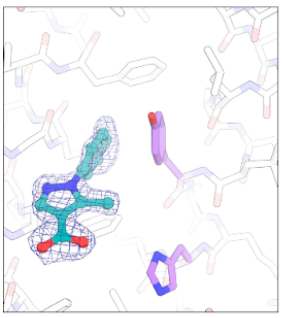

ZINC000000066090 | 7HJX
1.55 Å | 0.19 | 38%

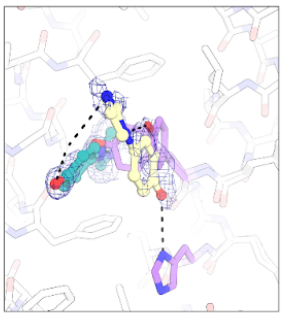

ZINC000012370416 | 7HJF
1.58 Å | 0.23 | 46%

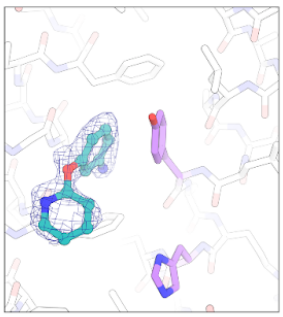

ZINC000002583439 | 7HJK
1.56 Å | 0.12 | 24%

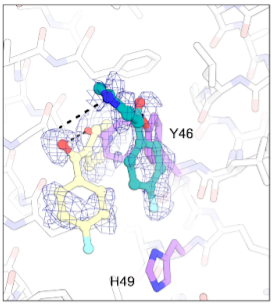

ZINC000002567980 | 7HJE
1.59 Å | 0.13 | 26%

ZINC000000155614 | 7HJ9
1.56 Å | 0.16 | 32%

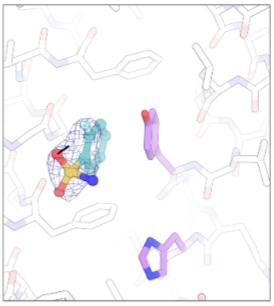

ZINC000002571408 | 7HJW
1.58 Å | 0.22 | 44%

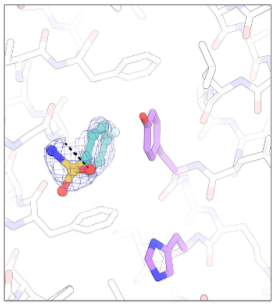

ZINC000000154564 | 7HJB
1.58 Å | 0.11 | 40%

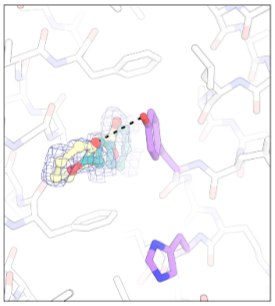

ZINC000000403990 | 7HJ7
1.6 Å | 0.31 | 62%

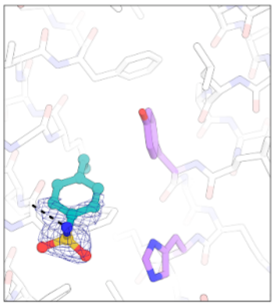

ZINC000000270975 | 7HJ8
1.59 Å | 0.42 | 84%

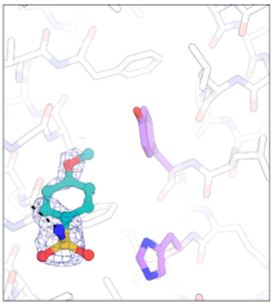

ZINC000002941706 | 7HJ3
1.54 Å | 0.38 | 76%

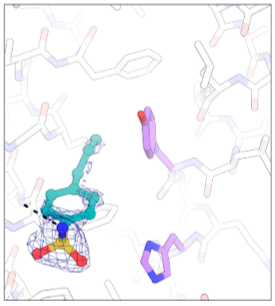

ZINC000004271832 | 7HJ6
1.58 Å | 0.36 | 72%

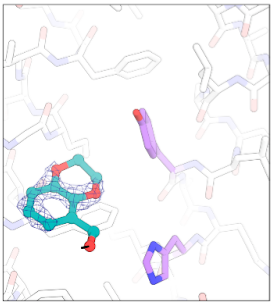

ZINC000000164504 | 7HJD
1.58 Å | 0.38 | 76%

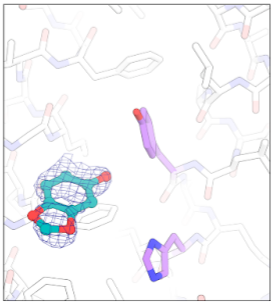

ZINC000000163774 | 7HJM
1.55 Å | 0.11 | 22%

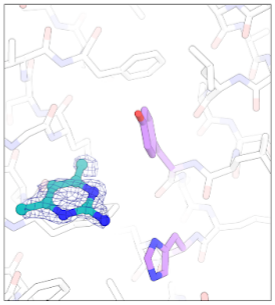

ZINC000000109930 | 7HJS
1.57 Å | 0.41 | 82%

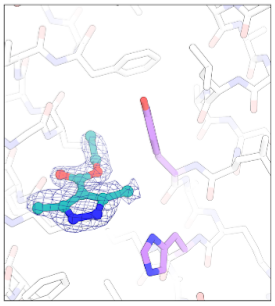

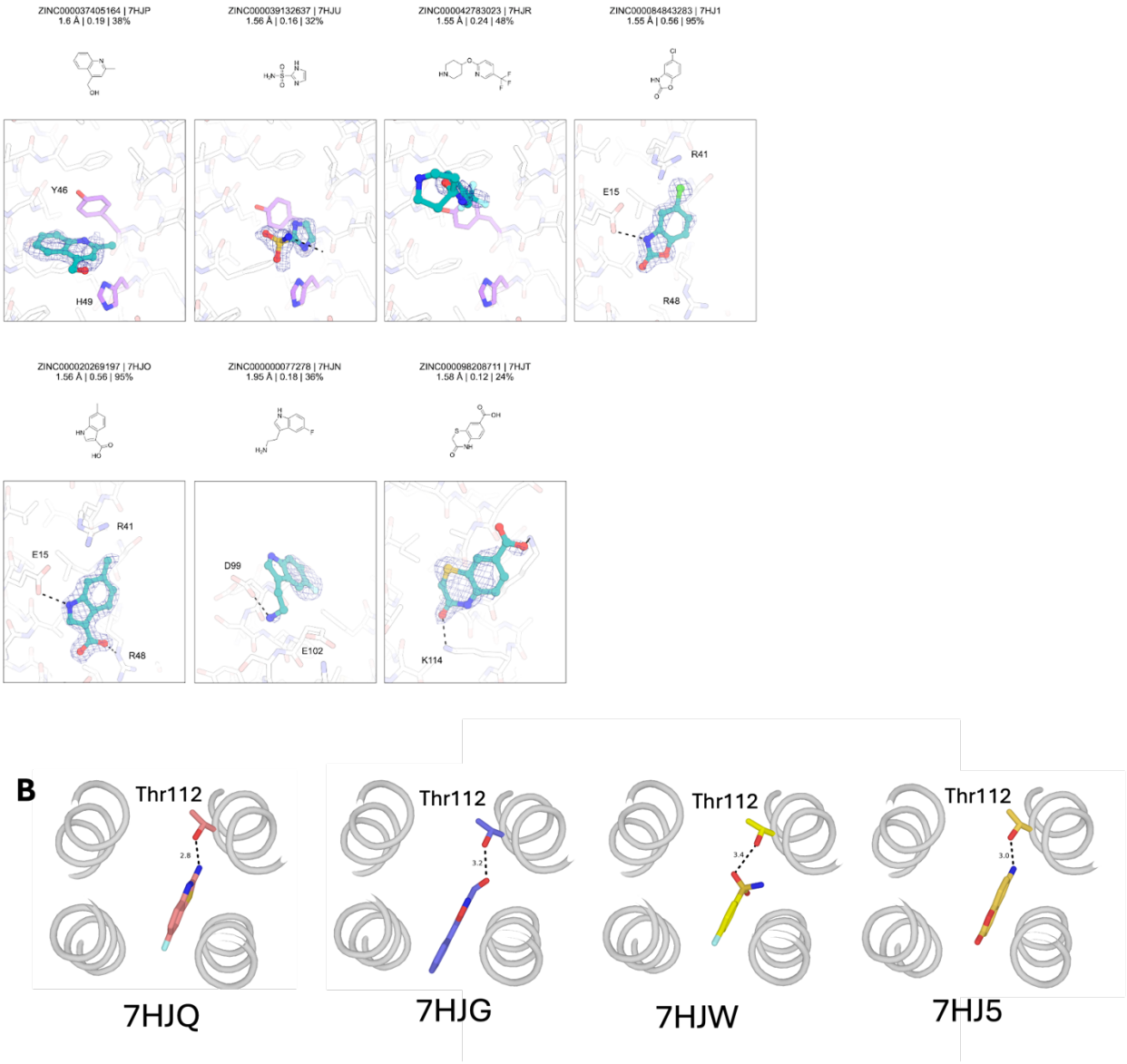

Figure S5: Chemical structures and electron density maps for the 43 fragment structures reported in this work. (**A**) PanDDA event maps (blue mesh, 2 σ) are contoured around fragments (teal/yellow sticks). The sidechains of residues Tyr46 and His49 are shown with purple sticks. Fragment names, PDB codes, resolution, 1-BDC value and refined occupancies are indicated. Hydrogen bonds are shown with dashed black lines. For clarity, residues 10-23 and 105-118 are hidden for fragments binding in the ABLE core. His49-mediated polar interaction could be found in majority of fragments at site B. (**B**) Another view to show the Thr112-mediated polar interactions in many fragments at site A, whose PDB codes are labelled at the bottom.

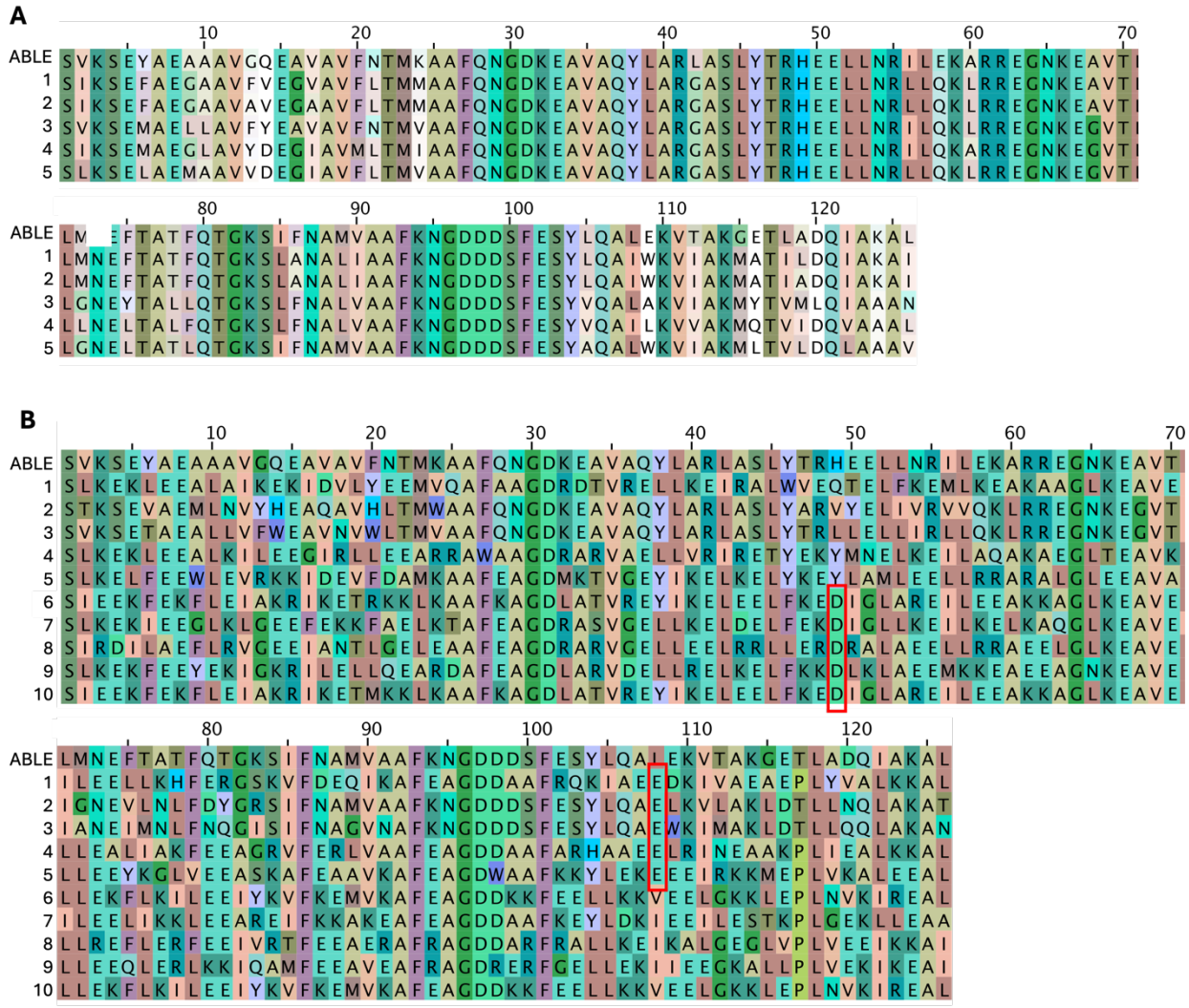

Figure S6. Sequence comparison between ABLE and FABLEs/KABLEs. (A) Amino acid sequence of all 5 FABLE designs ($FABLE_{D1}$ to $FABLE_{D5}$), with ABLE shown on the top. (**B**) Amino acid sequence of all 10 KABLE designs ($KABLE_{D1}$ to $KABLE_{D10}$), with ABLE shown on the top. The designed base Glu108 in the first strategy ($KABLE_{D1}$ to $KABLE_{D5}$) and Asp49 in the second strategy ($KABLE_{D6}$ to $KABLE_{D10}$) are highlighted in the red box.

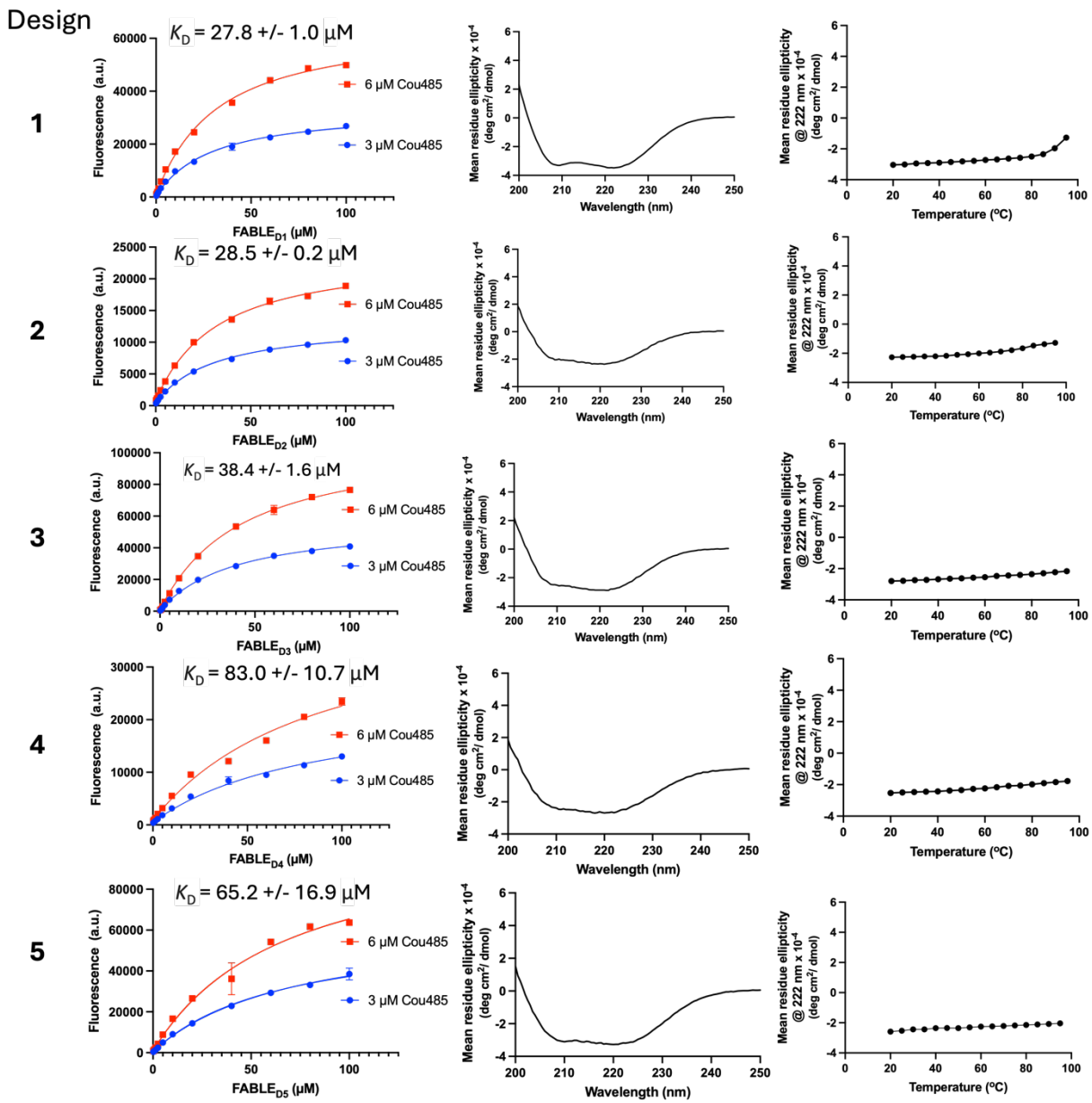

Figure S7. Characterization of five FABLE Designs. Left column: Fluorescence of Cou485 at 2 fixed concentrations of 3 μM and 6 μM were measured in the presence of increasing amounts of each protein. The binding constants were obtained by fitting with the equation in the section 1.7 of SI. The error bars represent standard deviations. Middle Column: circular dichroism spectra shows that all the designs are helical proteins. Right column: temperature-dependent circular dichroism signals measured at 222 nm show that all designs are thermostable. The design 1 was designated as FABLE.

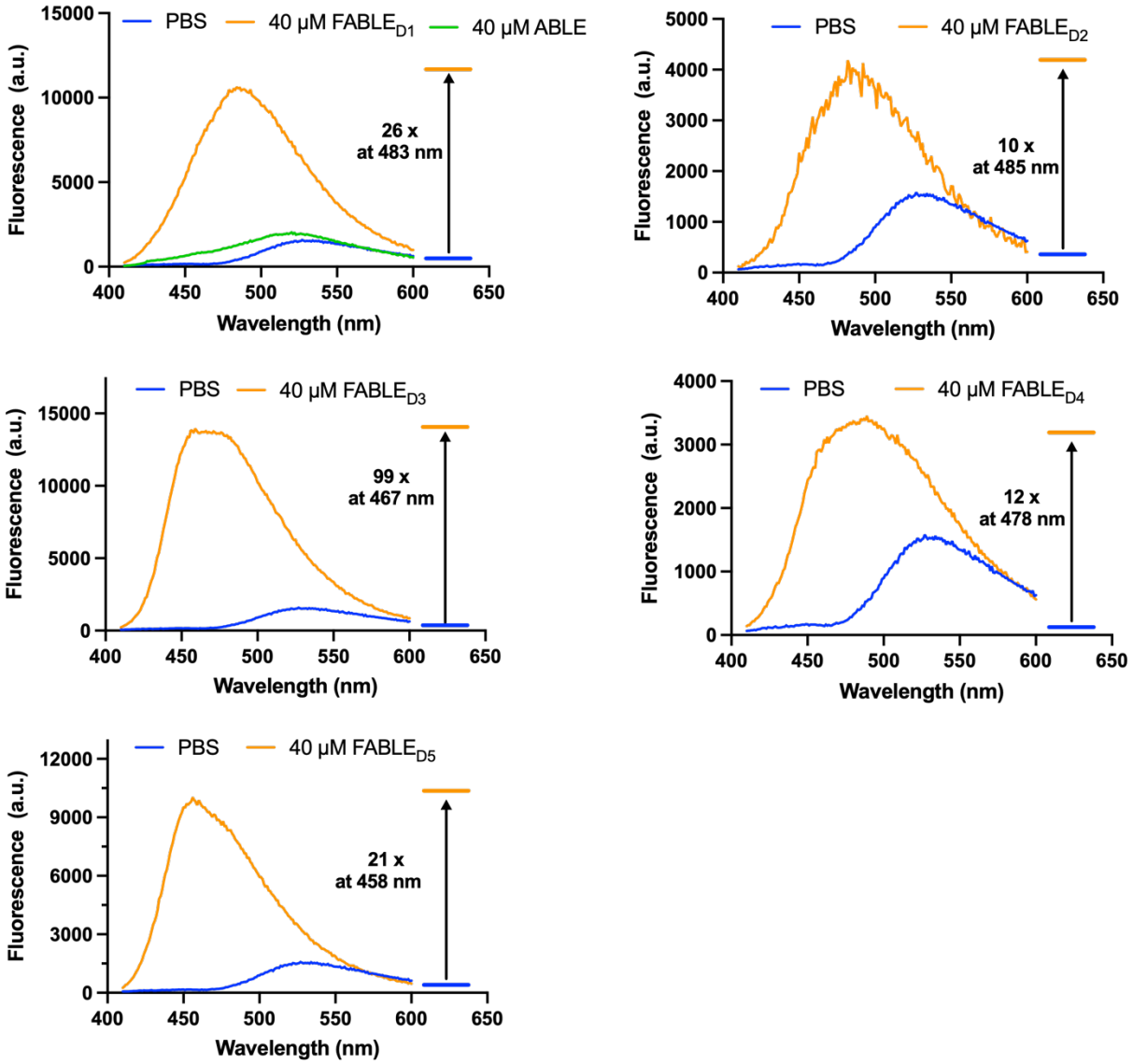

Figure S8. Emission Spectra of Cou485 in the presence of FABLE protein derivatives. The fluorescence emission spectrum of 6 μM Cou485 was recorded using BioTek Synergy Neo2 Reader with an excitation of 395 nm. The indicated FABLEs or ABLE (control) were present at 40 μM.

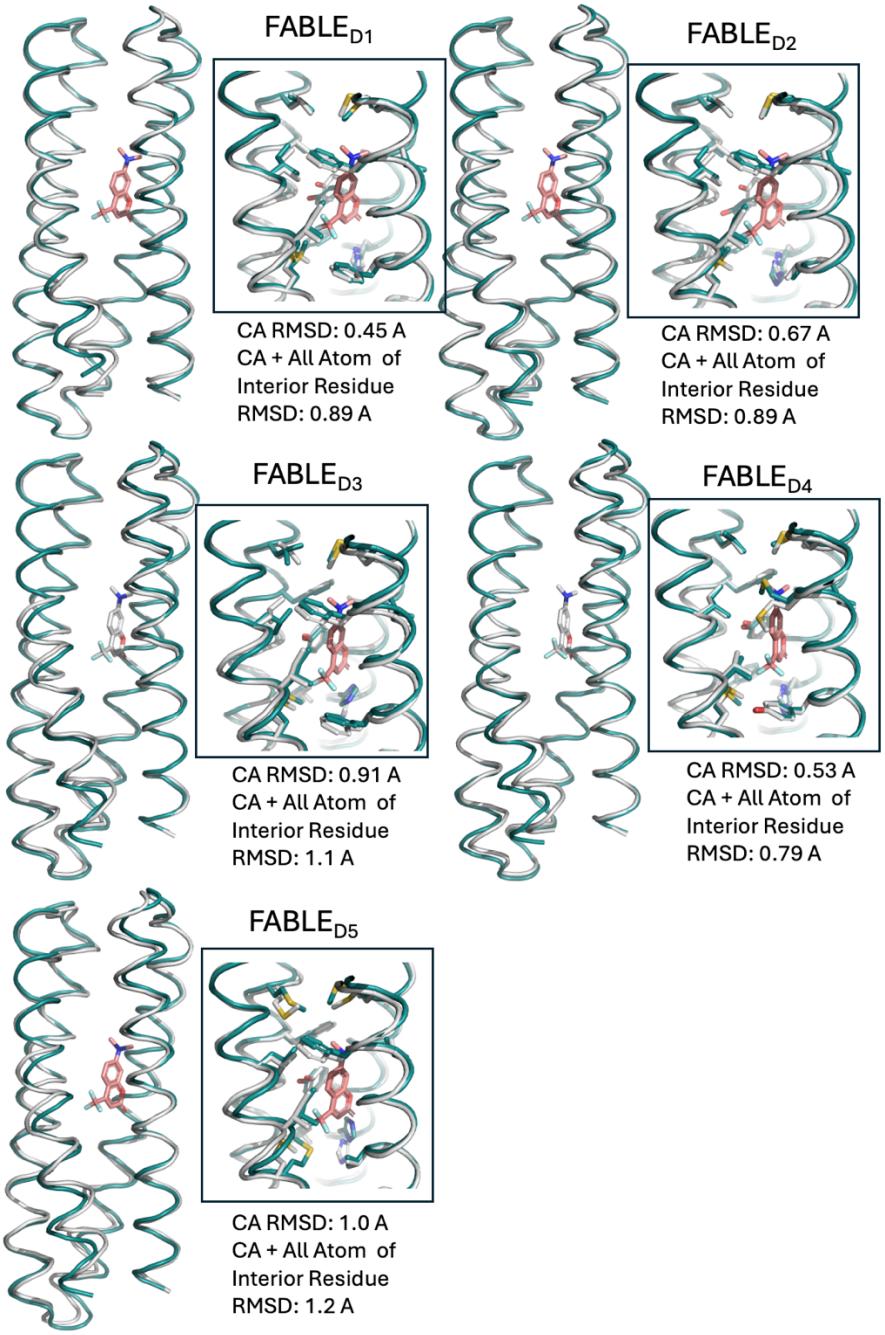

Fig. 9: AF3 prediction agrees with all 5 FABLE designs. Left: Designed structure (protein in teal cartoon and ligand in pink stick) and predicted structure (protein in grey cartoon). Right: Zoom in view of active site with carbon in designed structures shown as the teal stick and carbon in predicted structures shown as a grey stick.

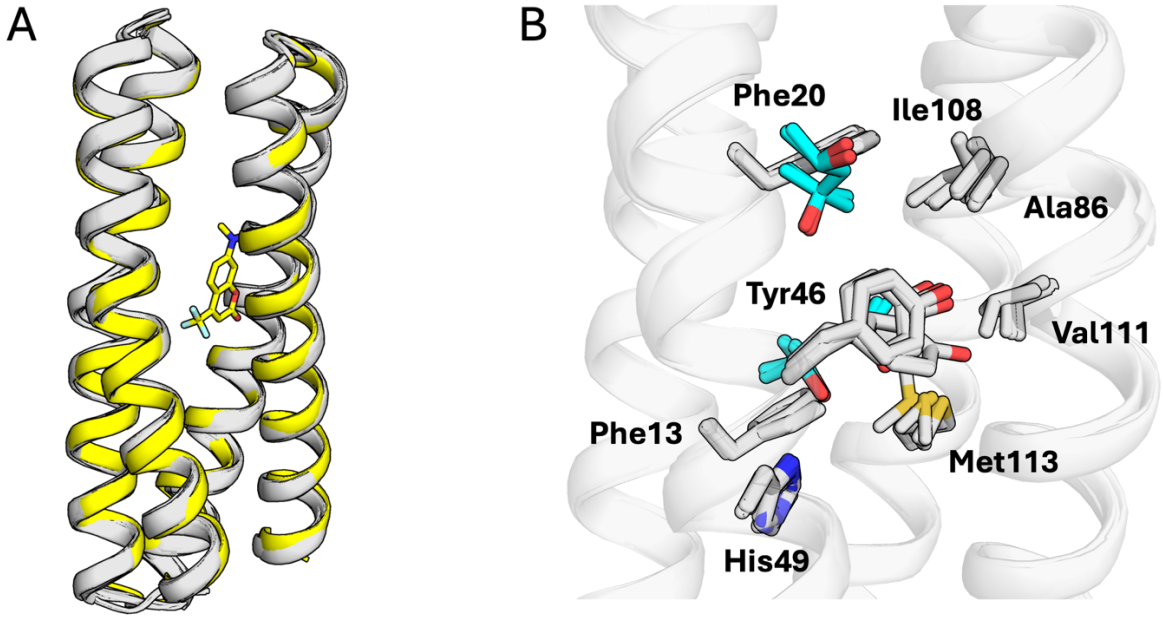

Fig. 10: The crystal structure of apo FABLE agrees with the designed structure. (A) Overlay of designed structure (yellow carbon) with structures from the individual asymmetric unit in the three crystal structures (9DWA, 9DWB, 9DWC) of FABLE (grey carbon). The Cou485 in the designed structure are shown in yellow sticks. The low solubility of Cou485 under crystallization conditions limited our ability to obtain a co-crystal structure. However, the un-complexed structures are in excellent agreement with the model of the complex (with sub-Å of Cα RMSD, table S1). (B) Active site view of structures from the individual asymmetric units in three crystal structures (9DWA, 9DWB, 9DWC) of FABLE. The sidechains of active site residues are shown in sticks. Two methylpentanediol molecules from the crystallization buffer, which occupy the binding site in 9DWA, are shown in blue carbons. Most residues are very well organized, including Met23. Tyr46 shows some variability in the different crystal environments

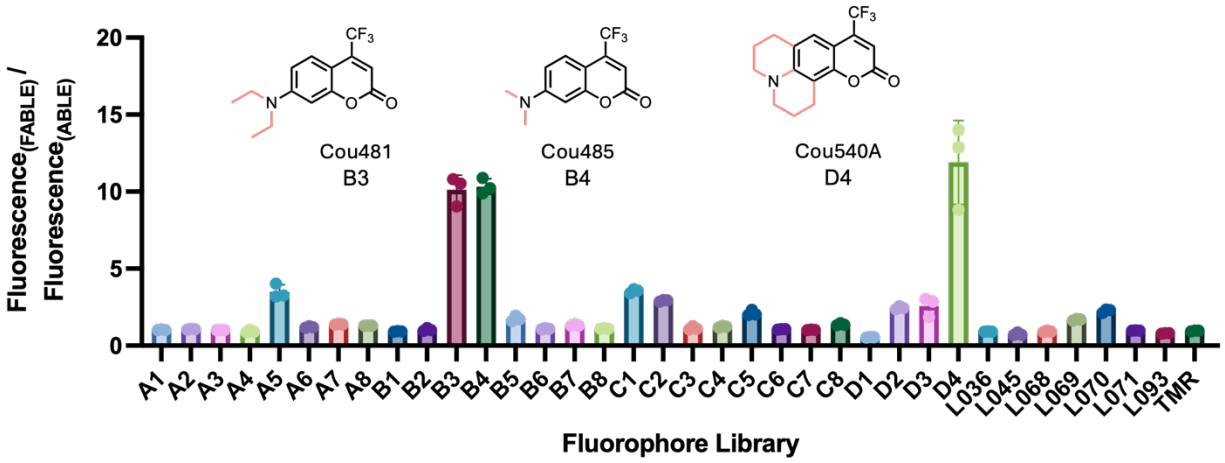

Figure S11: Exploring the chemical space of FABLE. The excitation and emission of fluorophores are in **Table S3**. The error bars represent standard deviations. (see section 1.5 of SI for experimental details)

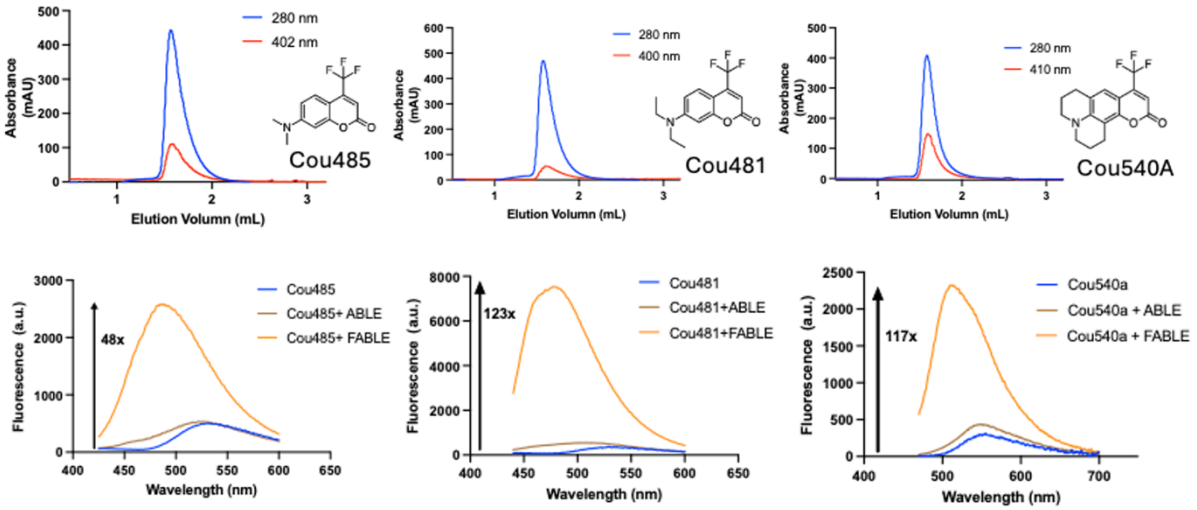

Fig. S12: FABLE interacts with Cou485, Cou481 and Cou540a as evidenced by SEC and an increase in fluorescence intensity by 48-123 fold. SEC analysis of 100 µM FABLE mixed with 200 µM indicated coumarin revealed a monomeric peak for FABLE, with the protein coeluting with the coumarin at the same time. Incubation of 1.5 µM Cou485 and Cou481 with 40 µM FABLE increased fluorescence intensity at 470 nm by 48 and 122 fold, respectively. Similarly, incubation of 0.5 µM Cou540a with 6 µM FABLE resulted in a 117-fold increase in fluorescence at 510 nm.

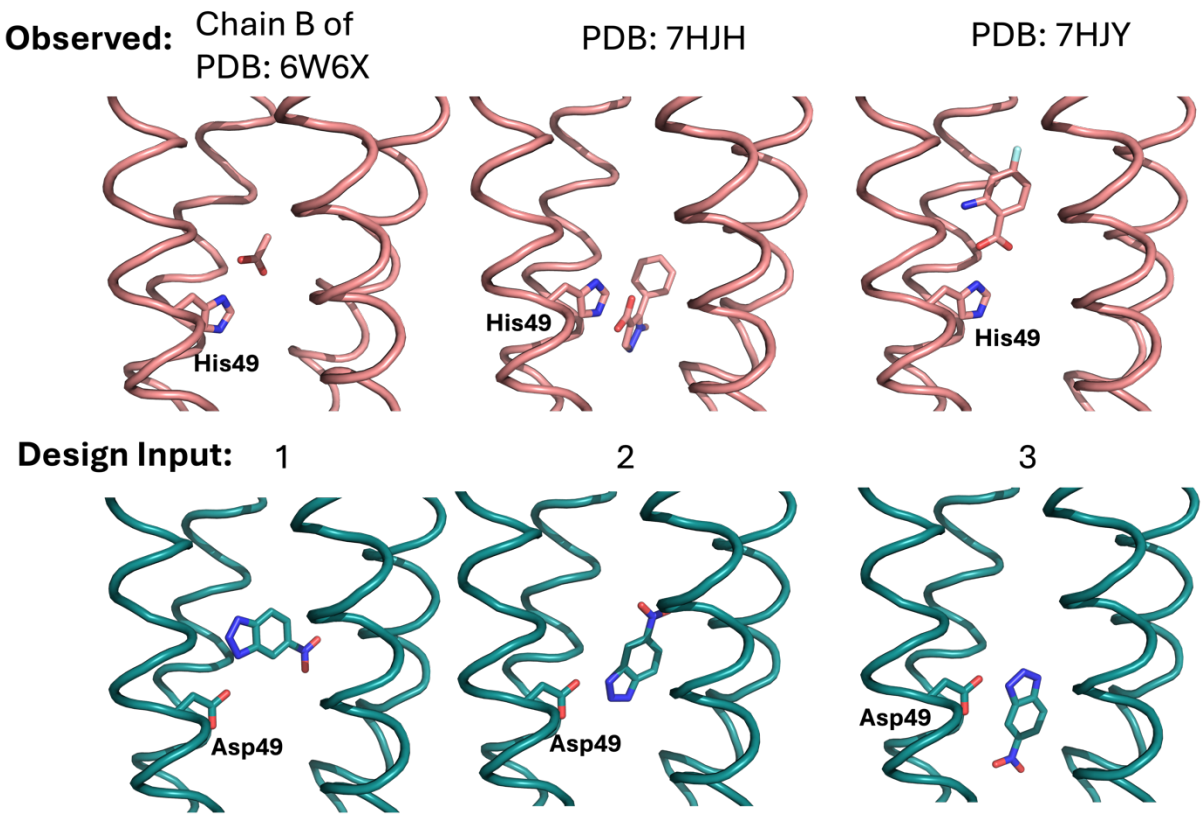

Figure S13. Observed His49-carboxylic interactions in ABLE-fragment complexes and the Asp49-6NBI interactions used as starting points to design KABLE1. Top: Examples of observed ABLE-fragment interactions with indicated PDB code, carbon of His49 and fragments are shown in pink sticks. Bottom: three initial input structure for designing KABLE1 with each utilizing one distinctive lone pair of electron on either OD1 or OD2 of Asp49 (see see section 1.11.2 of SI). Carbon of Asp49 and fragments are shown in teal sticks. Similar observed orientations of residue 49 and fragment are used as input to design KABLE1.

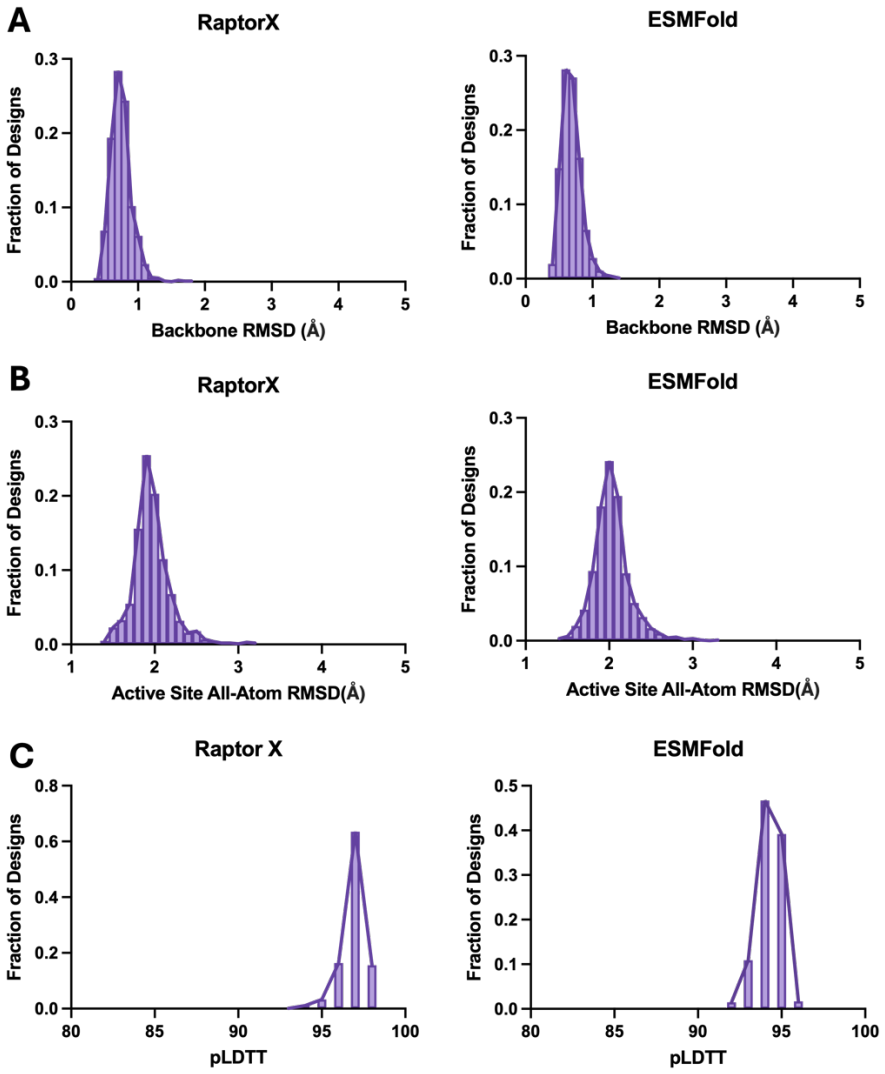

Figure S14: Structure prediction metrics of KABLE designs bearing Asp49. All 1000 sequences were subjected to structure prediction with both RaptorX and ESMFold. (**A**) Backbone RMSD between either prediction and design shows most of designs are within 1 Å backbone RMSD. (**B**) All-atom RMSD of active site residues (< 3.5 Å of TSA) between either prediction and design shows the median of active site RMSD at 2 Å. (**C**) pLDTT scores from both prediction methods show all the designs are with pLDTT score over 90.

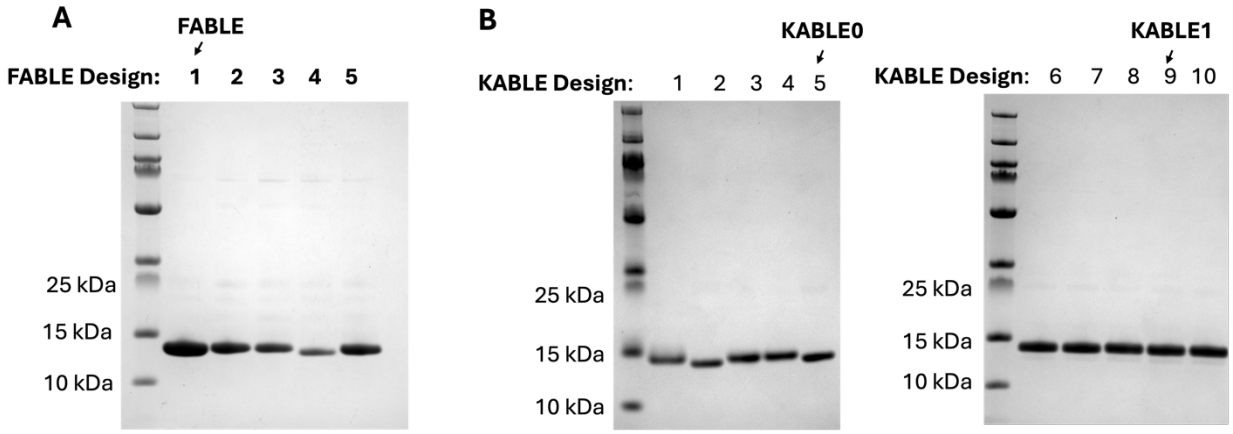

Figure S15. SDS-PAGE Characterization of all designed proteins. **(A)** SDS-PAGE analysis of the purified form of all 5 FABLE designs ($FABLE_{D1}$-$FABLE_{D5}$), with the $FABLE_{D1}$ designated as FABLE. **(B)** SDS-PAGE analysis of all 10 KABLE designs from the first design strategy of aromatic box ($KABLE_{D1}$-$KABLE_{D5}$) and the second design strategy of versatile residue 49 ($KABLE_{D6}$-$KABLE_{D10}$), with the $KABLE_{D5}$ highlighted as KABLE0 and $KABLE_{D9}$ highlighted as KABLE1.

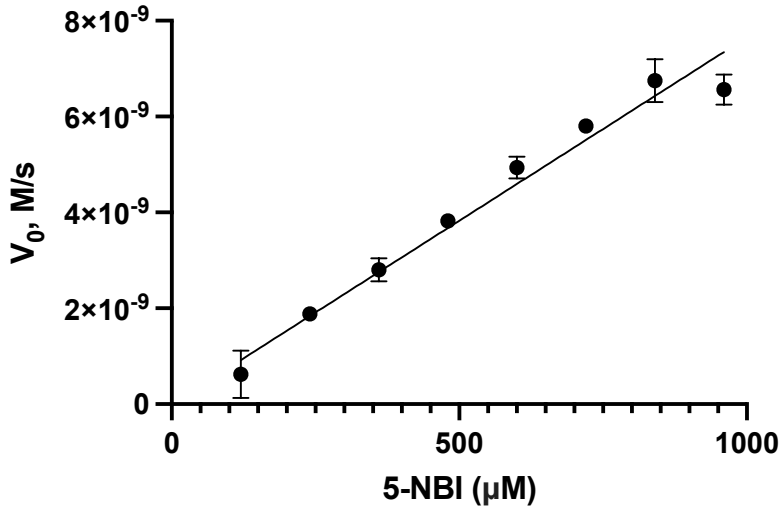

Figure S16: Substrate concentration dependence versus rate data for KABLE0. The reaction was measured with 1 μM KABLE0 in pH 8 buffer. Background reaction at the same condition without enzyme was subtracted and data were analyzed by least squares analysis to the linear portion of the Michaelis-Menten model ($v_0 = (k_{cat}/K_M)[E_0][S]$), and k_{cat}/K_M was deduced from the slope. Error bar stands for standard deviations.

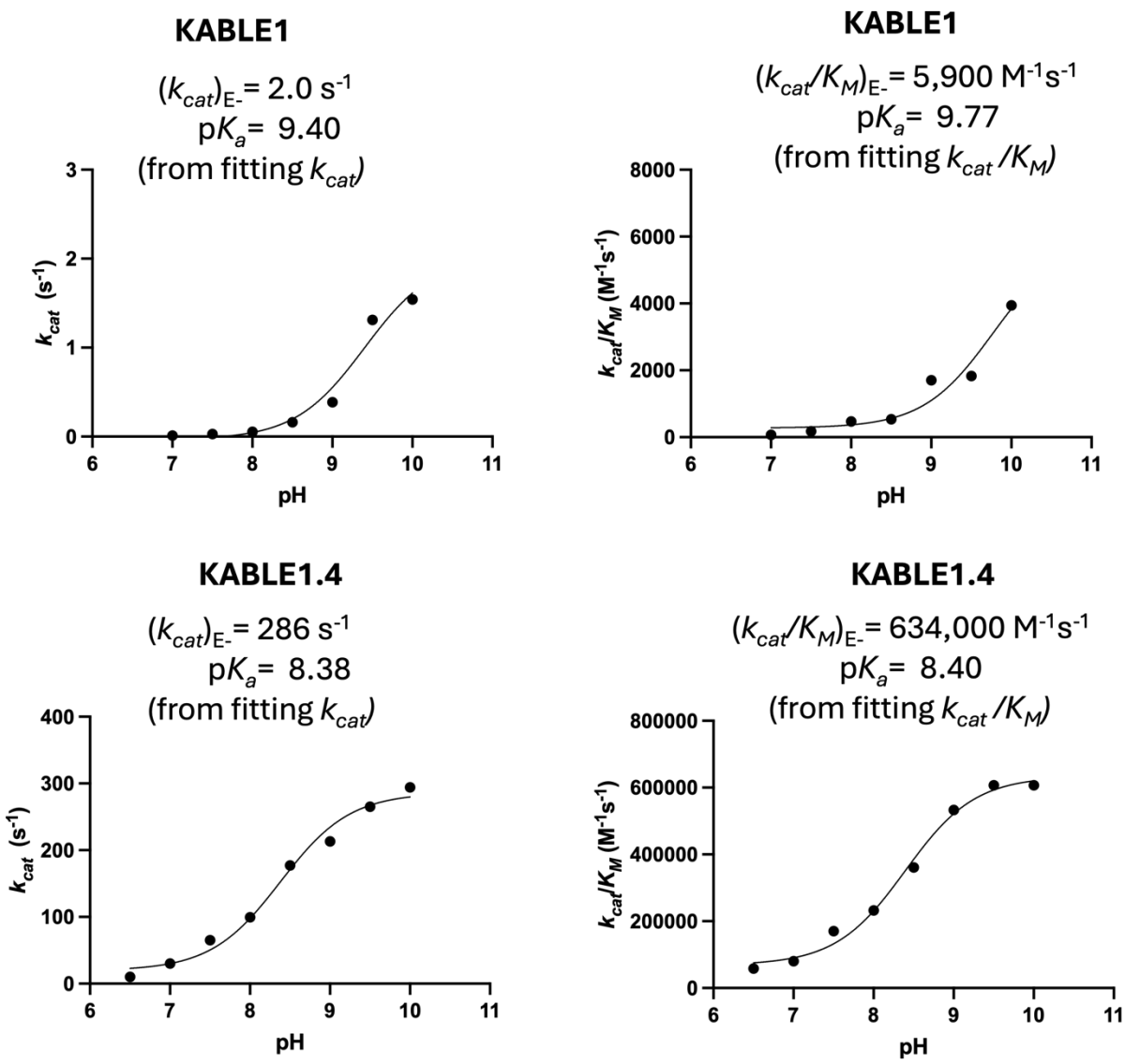

Figure S17: Dependence of k_{cat}/K_M and k_{cat} on pH. For each pH, its initials rate under a series of substrate concentration was used to fit the k_{cat}/K_M and k_{cat} for each pH using Michaelis-Menton equation at GraphPad Prism. The dependence of k_{cat}/K_M and k_{cat} on pH was fitted using the equation $k_{cat}/K_M = (k_{cat}/K_M)_{EH} \times (1-f_{E-}) + (k_{cat}/K_M)_{E-} \times f_{E-}$ or $k_{cat} = (k_{cat})_{EH} \times (1-f_{E-}) + (k_{cat})_{E-} \times f_{E-}$, where f_{E-} is the fraction of enzyme in deprotonated form. See **section 1.7** of SI for details

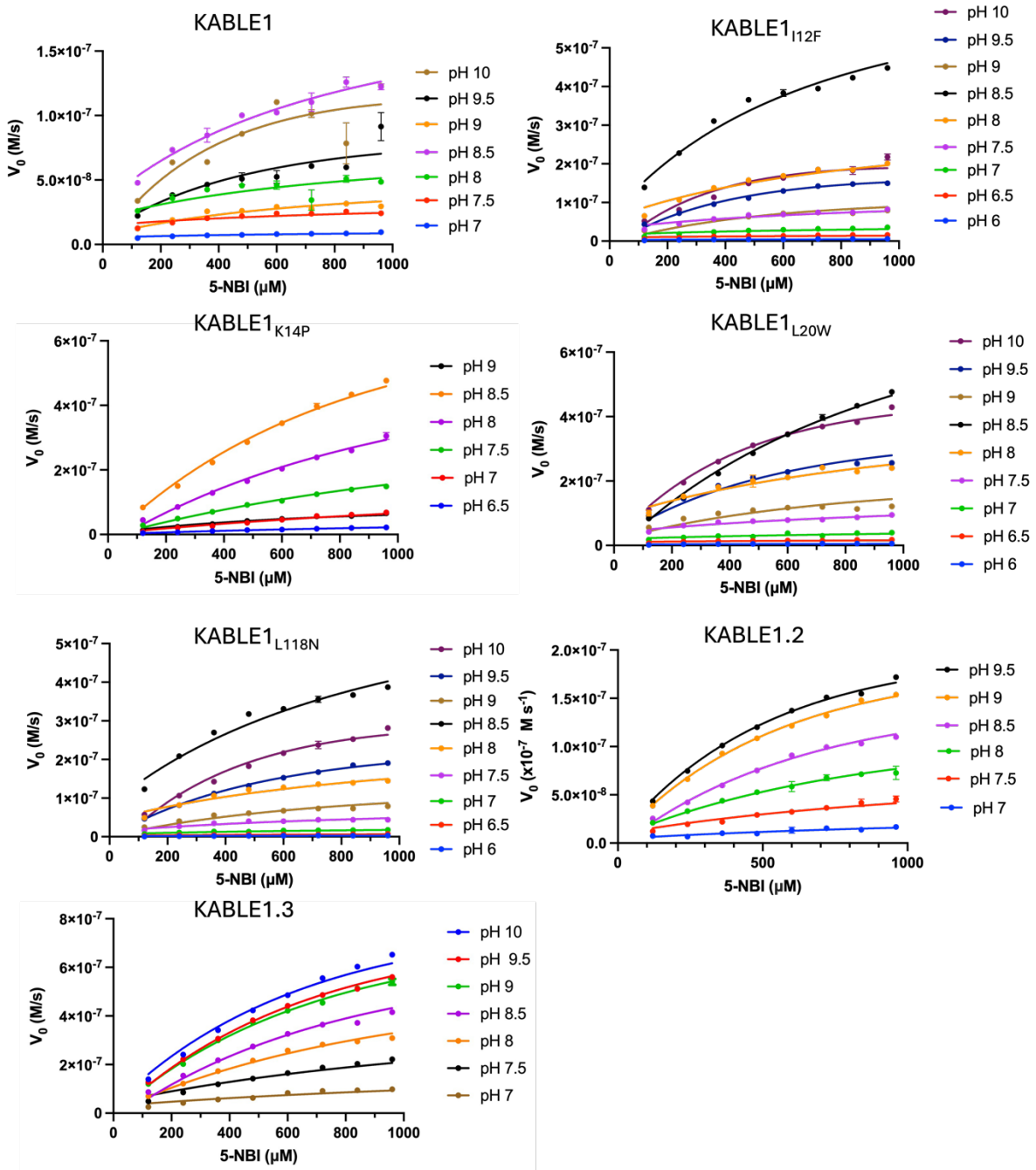

Figure S18: Global fitting of k_{cat}, K_M and pK_a for the Kemp eliminases.. The initial velocities at all substrate concentrations and pH were used to fit a shared k_{cat}, K_M and pK_a at each pH. For KABLE1$_{K14P}$, KABLE1.2, KABLE1.3, KABLE1.4, The value of k_{cat}/K_M was well described, but the fit values of k_{cat} and K_M tended to covary. The optimal shared value of k_{cat} was therefore obtained from an R^2- analysis, which is shown in Fig. S15. The optimal k_{cat} was used to fit the shared K_M and pK_a. Its standard deviation was obtained by taking the highest ratio of standard deviation to mean of the fitted k_{cat}, considering that there may be more error for the values of the of k_{cat} from R^2 analysis. Protein concentrations used for different pH are summarized in Table. S5. The error bar represents the standard error of the mean. Kinetic parameters and pK_a are summarized in table S4.

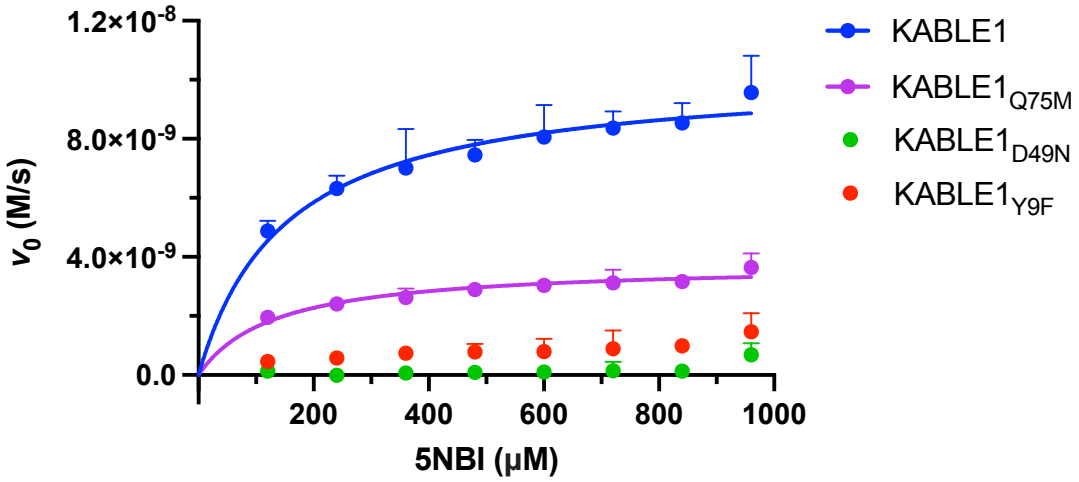

Figure S19. Substrate concentration versus rate data for KABLE1 mutants at Q75 and Y9 and D49. Reactions were measured at pH 7.0 buffer (20 mM HEPES,100 mM NaCl) with 1 μM KABLE1, 2.5 μM KABLE1$_{Q75M}$, 2.5 μM KABLE1$_{Y9F}$ and 2.5 μM KABLE1$_{D49N}$, respectively. Fitting the data with Michaelis-Menten model yielded KABLE1 (k_{cat}/K_M = 68 ± 28 M^{-1} s^{-1}, k_{cat} = 1.0 ± 0.10 x10^{-2} s^{-1}, K_M = 0.15 ± 0.023 mM^{-1}) and KABLE1$_{Q75M}$ (k_{cat}/K_M = 11 +7.3 M^{-1} s^{-1}, k_{cat} = 0.15 ± 0.013 x10^{-2} s^{-1}, K_M = 0.13 ± 0.083 mM^{-1}). For KABLE1$_{Q75M}$ and KABLE1$_{D49N}$, the fitting was not able to return reliable parameters. Error bar represents standard deviation.

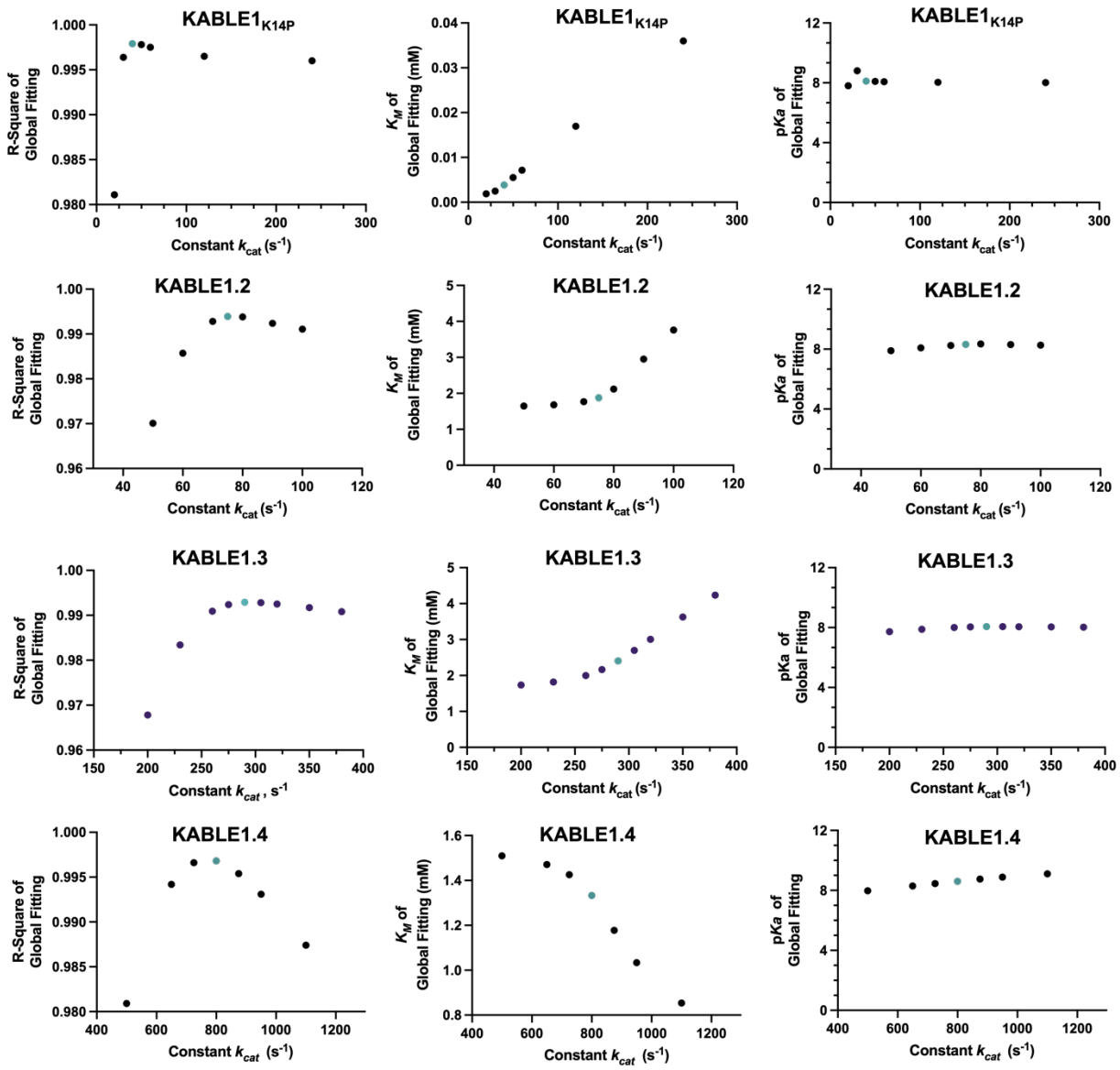

Figure S20. R-square analysis of KABLE1$_{K14P}$, KABLE1.2, KABLE1.3, KABLE1.4. A series of constant k_{cat} was used to globally fit the K_M and pK_a. The constant k_{cat} (in green) with the highest R-square was selected as the optimal k_{cat}. K_M covaries to the constant k_{cat} and minimal effect of constant k_{cat} on pK_a indicates the pK_a is stable over a wide range of constant pK_a around the optimal pK_a.

A

```
ABLE             SVKSEYAEAAAVGQEAVAVFNTMKAAFQNGDKEAVAQYLARLASLYTRHEELLNRILEKA 60
KABLE1.2         SLKEKFEEYEKIGPRILELWQEARDAFEAGDLARVDELLRELKELFKKDLKLAEEMKKEA 60
KABLE1.2.crystal SLKEKFAEYEAIGPRILELWQAARNAFEAGDLARVANLLAELKELFKKDLNLANAMAAEA 60

ABLE             RREGNKEAVTLMNEFTATFQTGKSIFNAMVAAFKNGDDDSFESYLQALEKVTAKGETLAD 120
KABLE1.2         EEAGNKEAVELLEEQLERLKKIQAMFEEAVEAFRAGDRERFGELLEKIIEEGKALLPLVE 120
KABLE1.2.crystal AEAGNKEAVALLAEQLERLKKIQAMFAAAVNAFRAGDREAFGALLEAIINEGKALLPLVE 120

ABLE             QIAKAL 126
KABLE1.2         KIKEAI 126
KABLE1.2.crystal AIKEAI 126
```

B

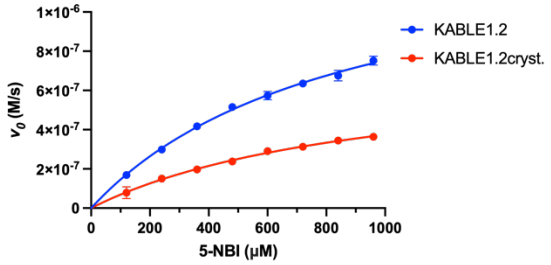

Figure S21. Substrate concentration versus rate data for KABLE1.2 and KABLE1.2$_{cryst}$. (A) Amino acid sequence alignment of ABLE with KABLE1.2 and KABLE1.2$_{cryst}$, shows the surface residues of ABLE were grafted to KABLE1.2$_{cryst}$. **(B)** Reactions were measured at pH 8.0 buffer (20 mM Tris,100 mM NaCl) with 0.1 μM KABLE1.2 and KABLE1.2$_{cryst,}$ respectively. Error bars represent standard deviations.

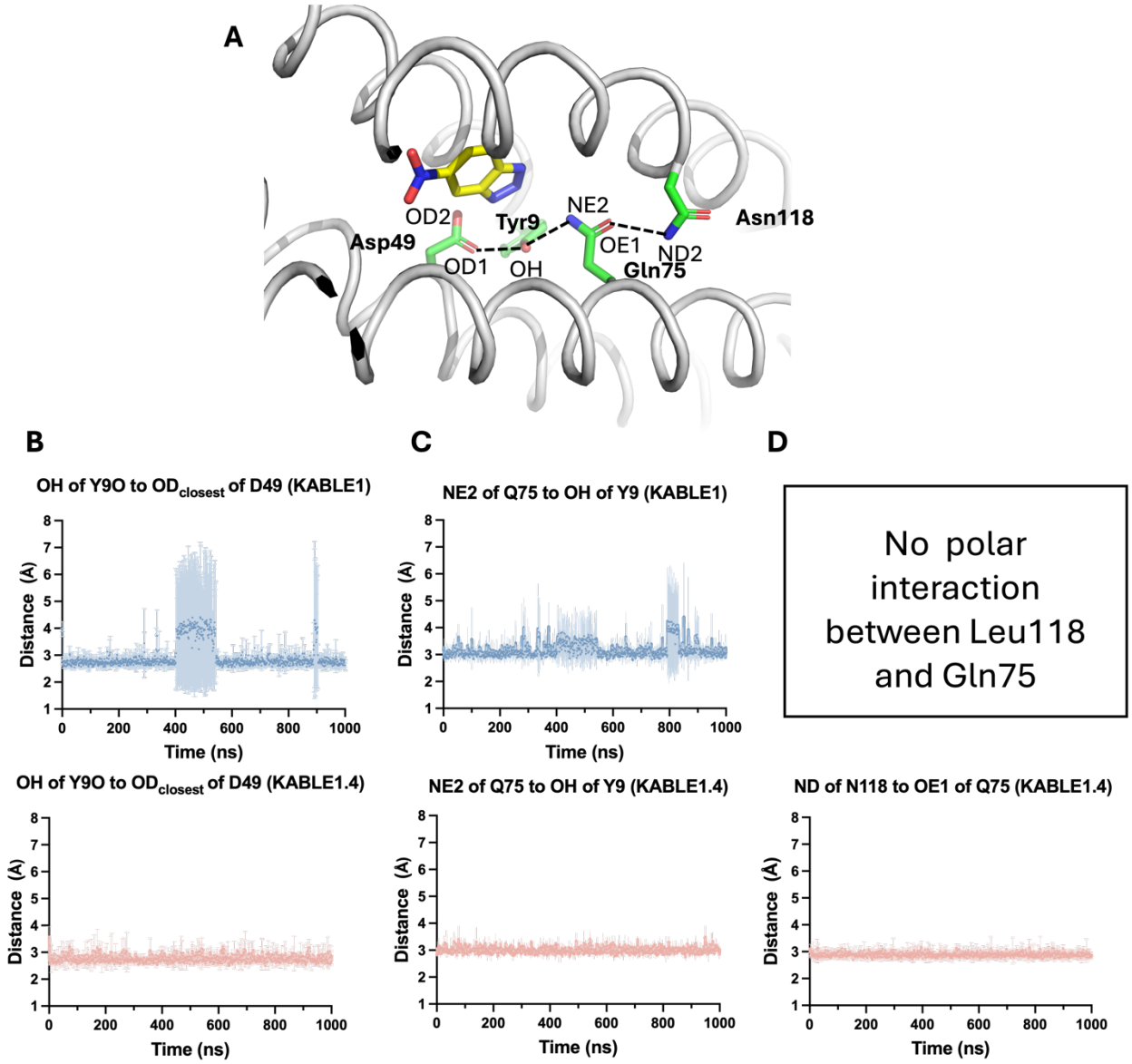

Figure S22. Stabilization of triad by Leu118Asn.
(A) A Representative snap shot of MD simulation of KABLE1.4-6NBT complex showing the triad consisting of Asp49, Tyr9, Gln75 and its stabilization residue Asn118, whose sidechain are shown in green sticks. The hydrogen bonding between these 4 residues are annotated with dotted line and their distance are within 2.8-3.2 Å. **(B-D)** The fluctuation of indicated distances between indicated atoms at the process of 1000ns MD simulation of KABLE1.4-6NBT (pink) complex, in comparison with KABLE1-6NBT (blue) complex. The distances are extracted using the *label bond* function of VMD. The mean of 3 replicates are shown as symbols with dark colors, and the standard deviations are shown as error bars with light colors.

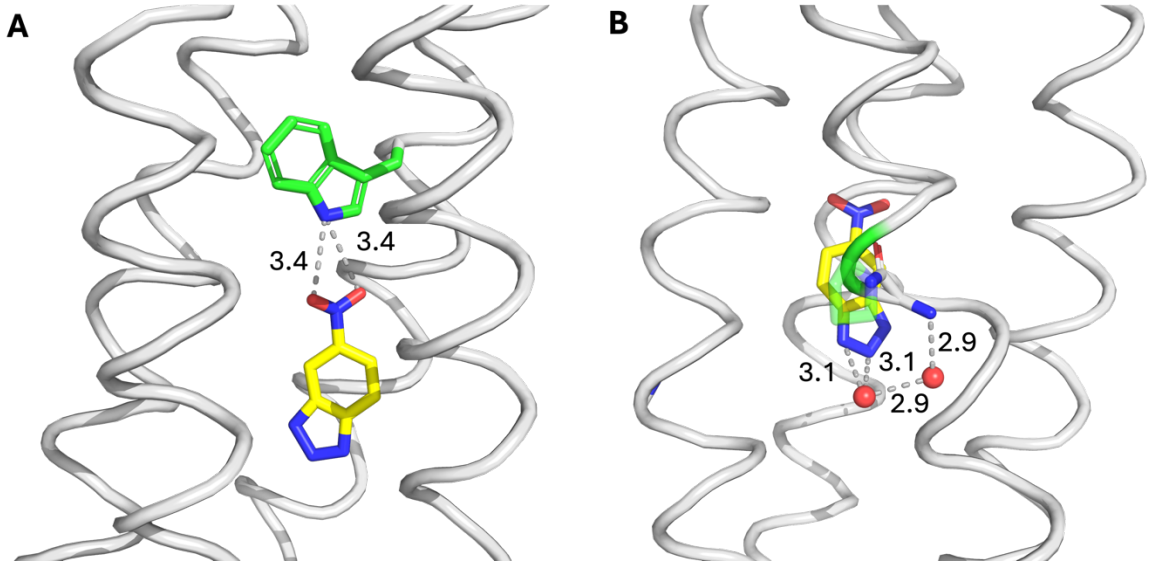

Figure S23: Representative MD snapshots showing the hydrogen bond introduced by Leu20Trp and the active site water introduced by Lys14Pro. **(A)** Representative MD snapshot showing the hydrogen bond between Trp20 and 6NBT. Trp20 is shown in green stick and 6NBT is shown in yellow stick. **(B)** Representative MD snapshot showing the water-mediated interaction to 6NBT, introduced by Pro14-mediated backbone kink. Distances are shown in Å with dashed lines.

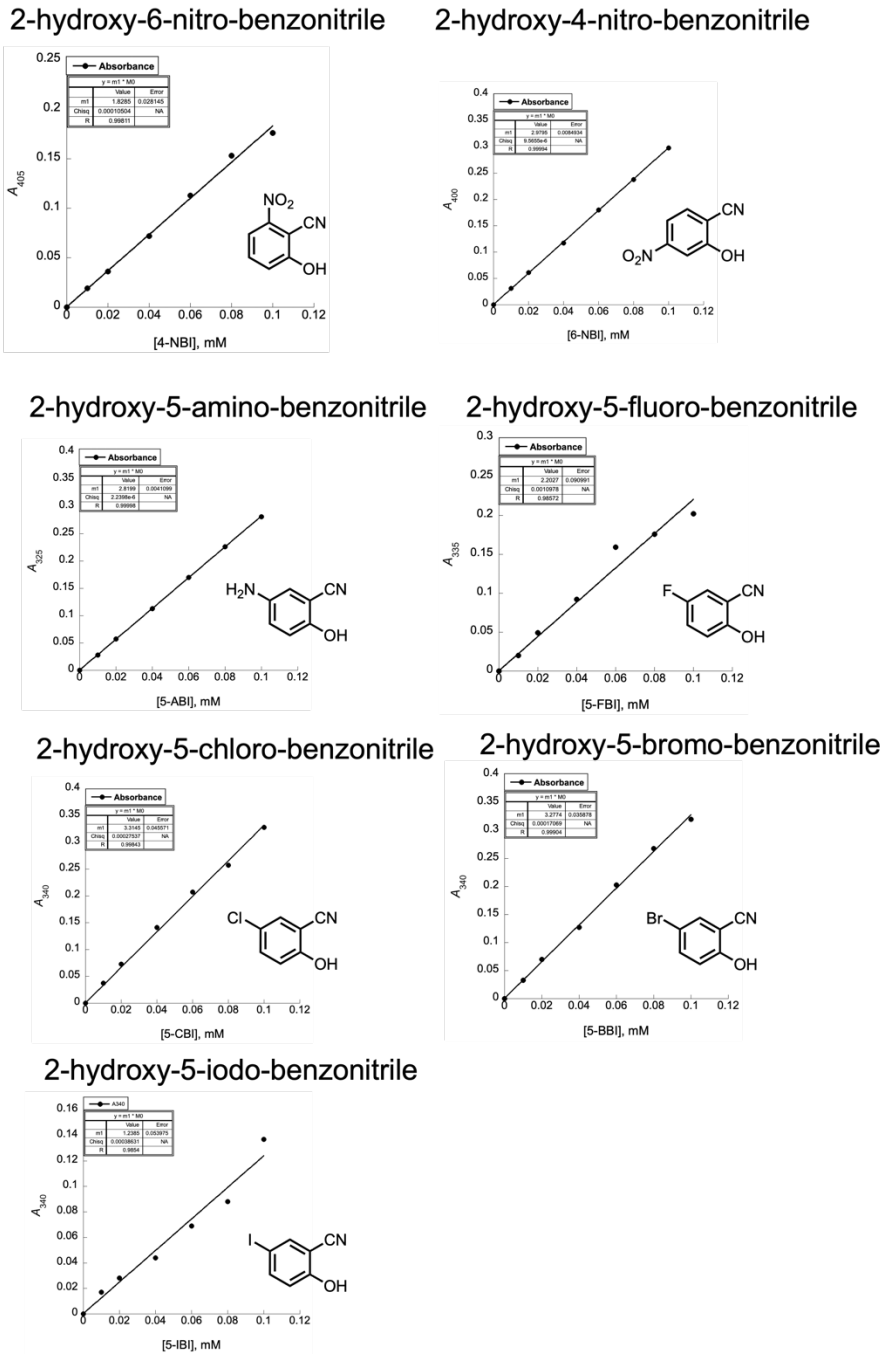

Figure S24. Extinction coefficient determination for products of benzisoxazole substrates using Beer-Lambert law. Data are presented as the mean values and the error bars represent standard deviations obtained from three independent measurements.

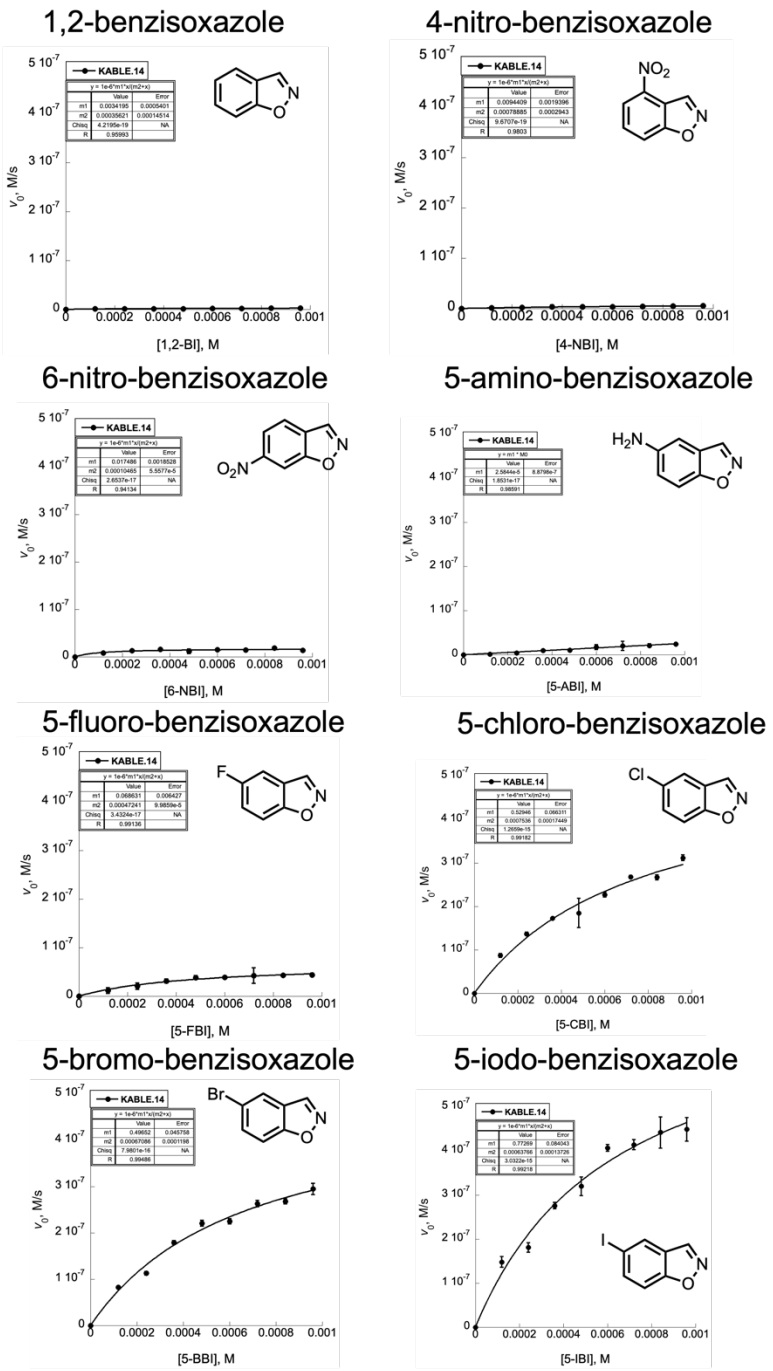

Figure S25. Ring opening of benzisoxazole analogues catalyzed by KABLE1.4. The activity of 1 μM KABLE1.4 was tested with 0.12-0.96 mM substrate in 20 mM TRIS, pH 8.0, 100 mM NaCl (black circle). Data are presented as the mean values and the error bars represent standard deviations obtained from three independent measurements.

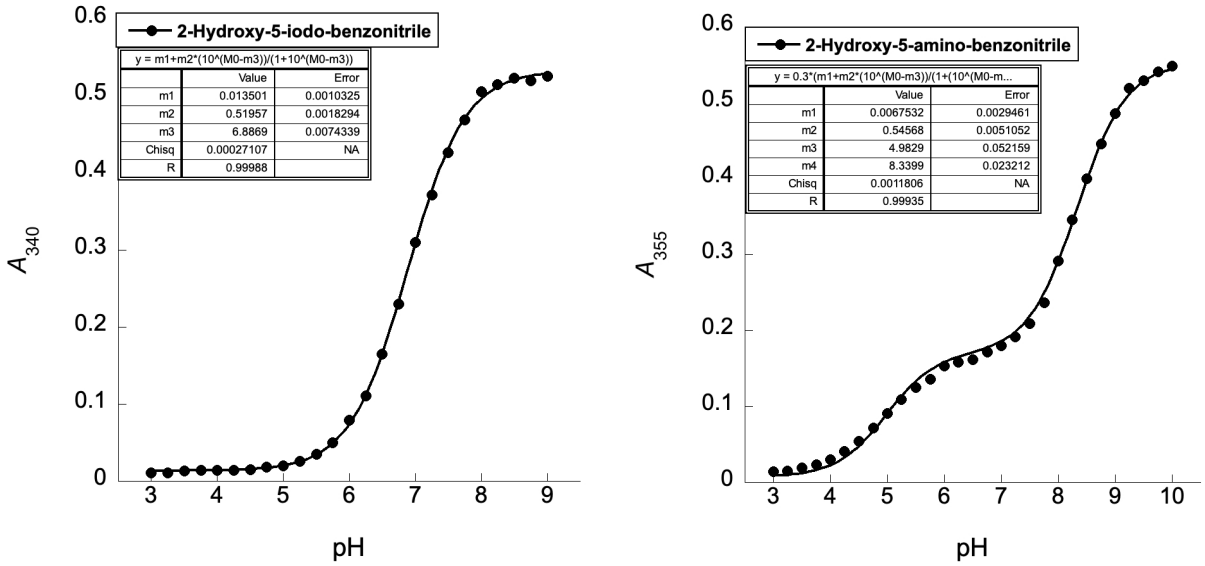

Figure S26. pK_a determination for 2-Hydroxy-5-iodo-benzonitrile (left) and 2-Hydroxy-5-amino-benzonitrile (right) using UV-vis spectrophotometric analyses. Absorbance at wavelength maximum was measured with 100 μM substrate in 100 mM buffer solutions at various pH ranging from 3.0-10.0.

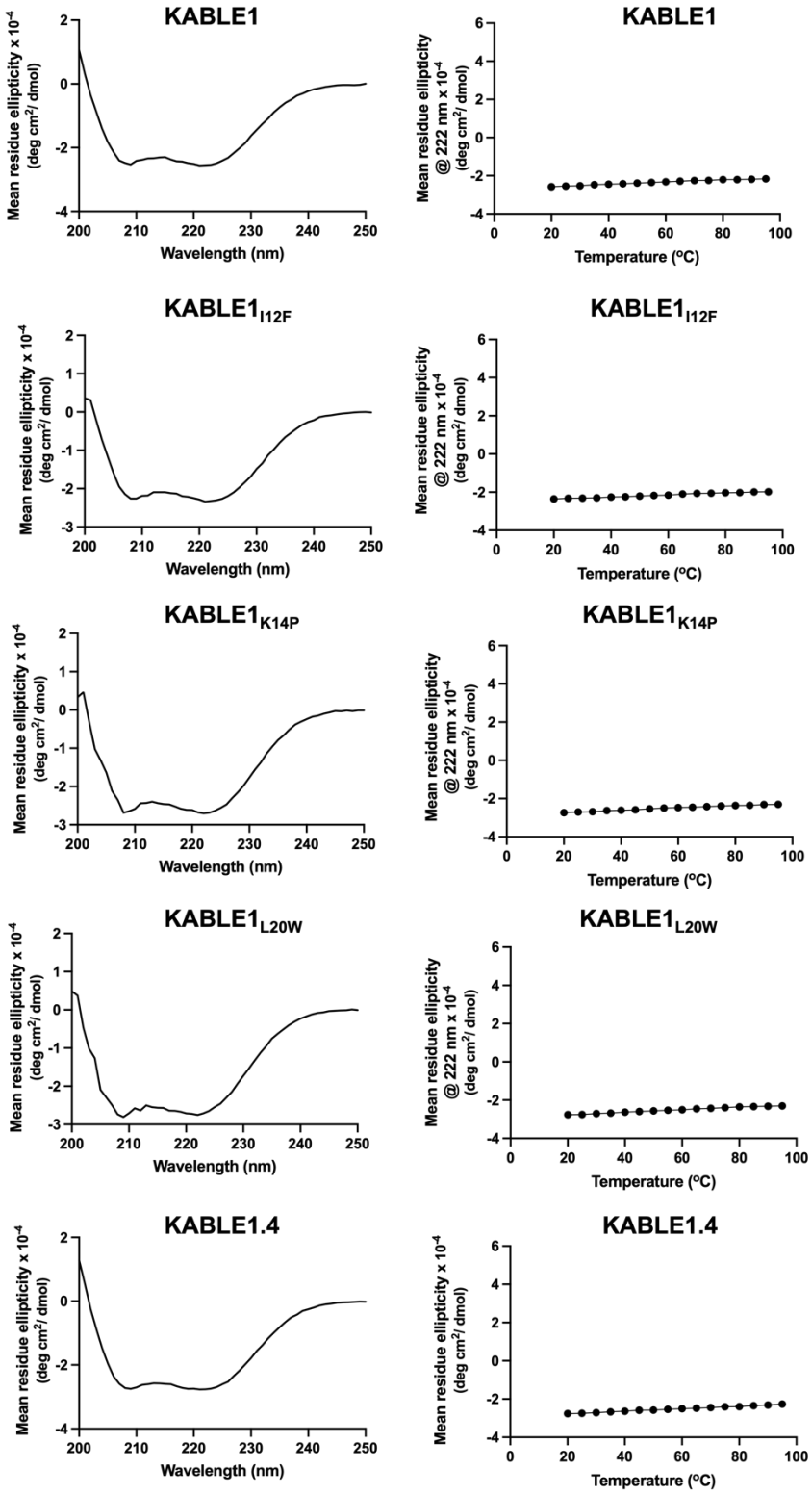

Figure S27. Thermostability of KABLEs. Proteins were prepared in 10 μM concentrations in PBS buffer. CD spectra were collected on a Jasco J-810 CD spectrometer in a 0.1 cm path-length quartz cuvette. Temperature-dependent data were collected at 222 nm from 20 to 95 °C with an interval of 5 °C and an increase rate of 2 °C/minute.

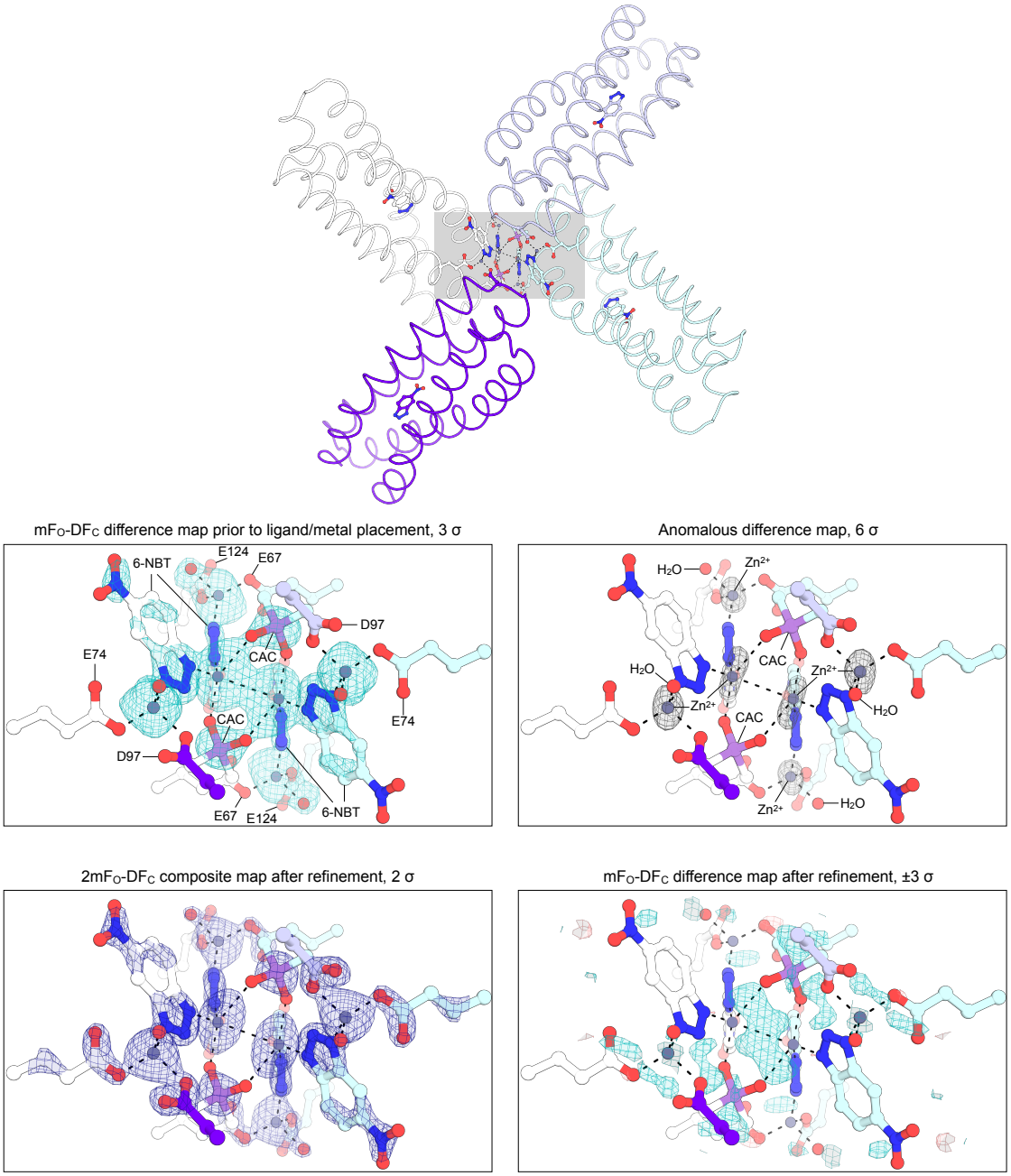

Figure S28. Stabilization of the KABLE12$_{cryst}$ crystal lattice by a 6NBT/zinc/cacodylate complex. The interface between four symmetry-related molecules is shown in the top panel. The gray shaded region is shown in the bottom panels with electron density maps used for assignment and modeling. The modeling of zinc (Zn) complexed by cacodylate (CAC) is supported by the anomalous difference map that shows strong peaks corresponding to the zinc positions and no peaks at the arsenic position, as expected for anomalous scattering for the two elements at 11111 eV. Although all features are supported by the mF$_O$-DF$_C$ difference map prior to complex modeling and the 2mF$_O$-DF$_C$ composite map after refinement, there are residue positive peaks in the mF$_O$-DF$_C$ difference map after refinement.

Table S1. Ligand efficiency for starting ABLE-apixaban and FABLE-coumarin interactions.

	Protein	Ligand	ΔG (kcal/mol)	#Heavy Atoms	Ligand Efficiency
1	ABLE	Apixaban	-7.23	34	0.213
2	$FABLE_{D1}$[a]	Cou485	-6.21	18	0.345
3	$FABLE_{D2}$	Cou485	-6.19	18	0.344
4	$FABLE_{D3}$	Cou485	-6.02	18	0.334
5	$FABLE_{D4}$	Cou485	-5.56	18	0.309
6	$FABLE_{D5}$	Cou485	-5.70	18	0.317
7	$FABLE_{D1}$[a]	Cou481	-7.14	18	0.357
8	$FABLE_{D1}$[a]	Cou540a	-7.77	18	0.353

[a]$FABLE_{D1}$ was designated as FABLE.

Table S2. Cα RMSD (Å) of FABLE design with AF3 prediction and each monomer of its 3 crystal structures. (PDB: 9DWA, 9DWB, 9DWC)

	Design	9DWA_A	9DWA_B	9DWB_A	9DWB_B	9DWC_A	9DWC_B	9DWC_C	9DWC_D	AF3
Design		0.78	0.79	0.93	0.91	0.91	0.99	1.01	0.93	0.61
9DWA_A	0.78		0.11	0.49	0.53	0.46	0.66	0.66	0.47	0.55
9DWA_B	0.79	0.11		0.51	0.54	0.47	0.67	0.67	0.48	0.57
9DWB_A	0.93	0.49	0.51		0.19	0.32	0.52	0.53	0.34	0.69
9DWB_B	0.91	0.53	0.54	0.19		0.32	0.49	0.50	0.36	0.70
9DWC_A	0.91	0.46	0.47	0.32	0.32		0.43	0.42	0.13	0.74
9DWC_B	0.99	0.66	0.67	0.52	0.49	0.43		0.14	0.44	0.88
9DWC_C	1.01	0.66	0.67	0.53	0.50	0.42	0.14		0.42	0.89
9DWC_D	0.93	0.47	0.48	0.34	0.36	0.13	0.44	0.42		0.78
AF3	0.61	0.55	0.57	0.69	0.70	0.74	0.88	0.89	0.78	

Table S3. Fluorophore library used to probe the specificity of FABLE.

Location	Name	Excitation	Emission	Structure
A1	Coumarin440	350	440	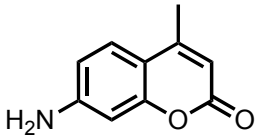
A2	Coumarin445	355	445	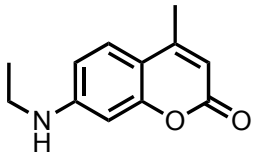
A3	Coumarin450	360	450	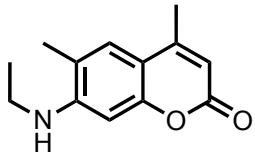
A4	Coumarin456	366	456	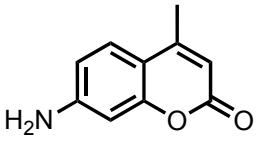
A5	Coumarin460	370	460	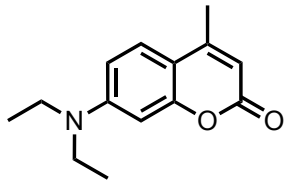
A6	Coumarin461	371	461	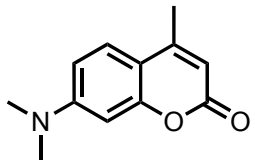
A7	Coumarin466	376	466	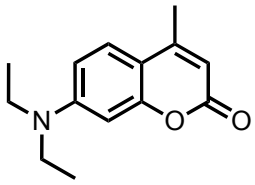

A8	LD473	383	473	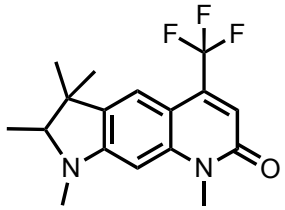
B1	Coumarin478	388	478	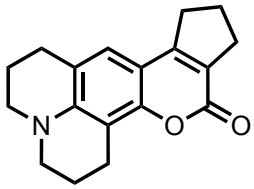
B2	Coumarin480	390	480	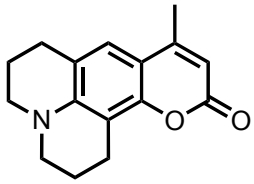
B3	Coumarin481	391	481	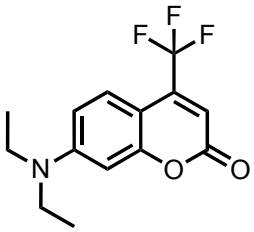
B4	Coumarin485	395	485	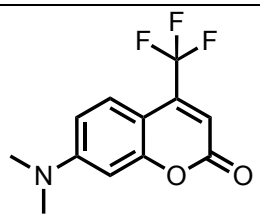
B5	LD489	399	489	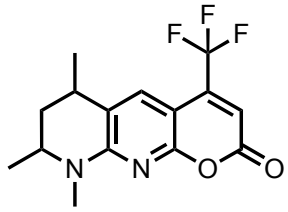
B6	Coumarin490	400	490	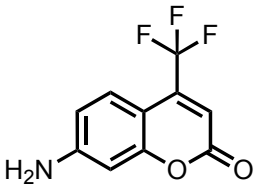
B7	LD490	400	490	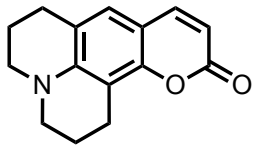

B8	Coumarin498	408	498	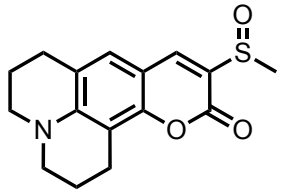
C1	Coumarin500	410	500	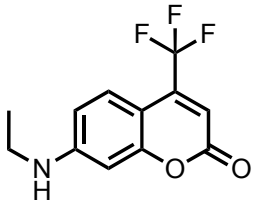
C2	Coumarin503	413	503	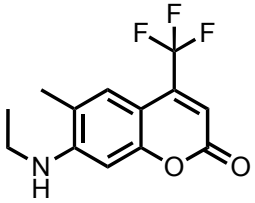
C3	Coumarin504	414	504	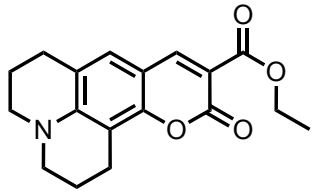
C4	Coumarin510	420	510	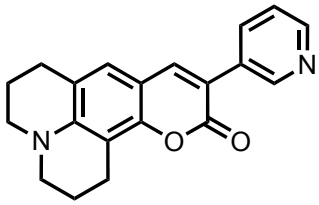
C5	Coumarin515	425	515	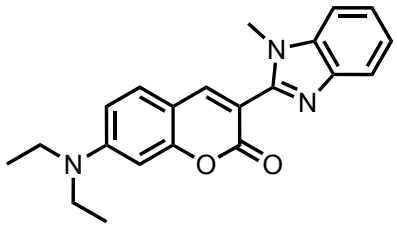
C6	Coumarin519	429	519	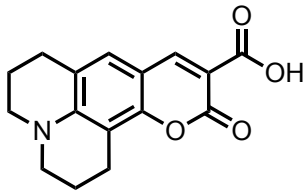
C7	Coumarin521	431	521	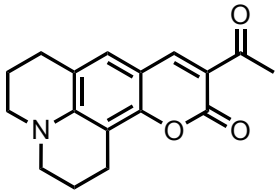

C8	Coumarin523	433	523	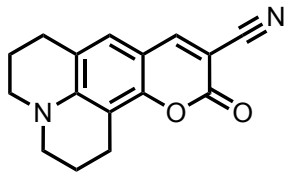
D1	Coumarin525	435	525	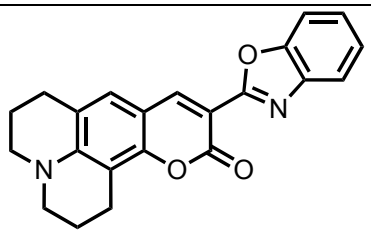
D2	Coumarin535	445	535	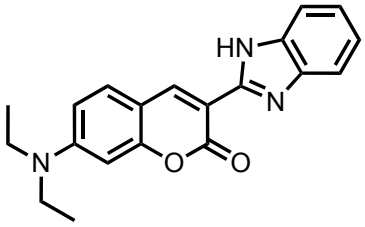
D3	Coumarin545	455	545	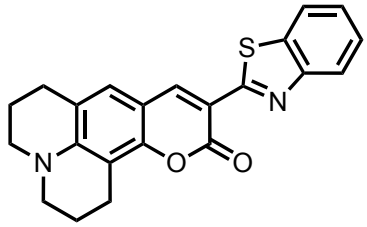
D4	Coumarin540a	460	540a	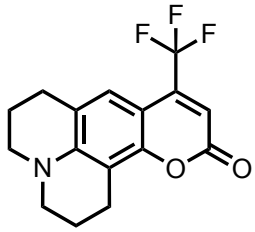
L036	Pyrromethene556	492	518	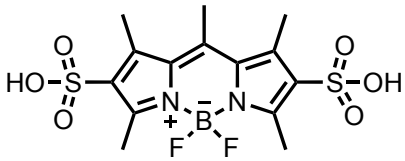
L045	FluoroI555	460	559	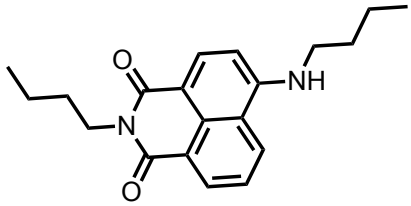
L068	Phenoxazone680	586	670	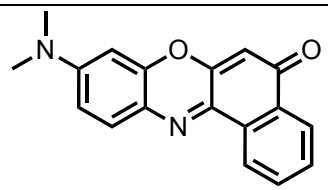

L069	CresylViolet670Perchlorate	592	628	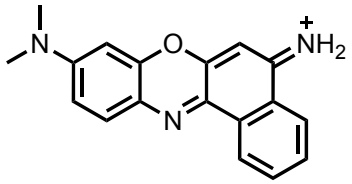
L070	NileBlue690Perchlorate	636	682	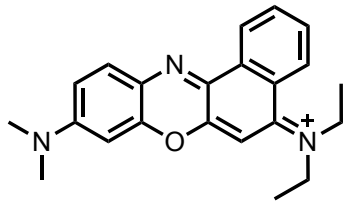
L071	LD690Perchlorate	616	638	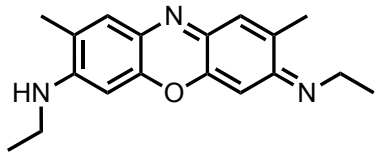
L093	HICl	539	569	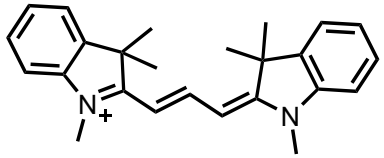
TMR	TMR	550	575	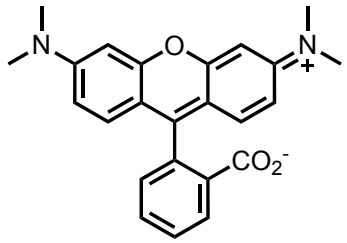

Table S4. Kinetic parameters of KABLEs[a].

Protein	k_{cat}, s^{-1}	K_M, mM	(k_{cat}/K_M), $M^{-1}s^{-1}$	pK_a
KABLE1	6.6 ± 0.9	0.99 ± 0.29	6,600 ± 2,100	10.01 ± 0.10
KABLE1$_{I12F}$	10.4 ± 0.5	0.99 ± 0.08	10,500 ± 900	9.53 ± 0.53
KABLE1$_{K14P}$[b]	30.0 ± 4.3	2.47 ± 0.10	12,200 ± 1,800	8.08 ± 0.02
KABLE1$_{L20W}$	20.9 ± 0.6	1.33 ± 0.10	15,800 ± 1,300	9.71 ± 0.03
KABLE1$_{L118N}$	17.3 ± 0.6	1.88 ± 0.09	9,200 ± 900	9.85 ± 0.03
KABLE1.2[b]	75 ± 10.7	1.88 ± 0.10	39,900 ± 6,000	8.31 ± 0.03
KABLE1.3[b]	290 ± 41	2.41 ± 0.08	121,000 ± 17,600	8.06 ± 0.03
KABLE. 1.4[b]	**800 ± 110**	**1.33 ± 0.05**	**600,000 ± 87,800**	**8.60 ± 0.02**

[a]Error bars represent the standard errors of the mean of 3 independent measurments. (See **section 1.7** of SI for details)
[b]Kinetic parameters are from the R^2 analysis of global fitting. (See **section 1.7** of SI for details)

Table S5. Protein concentrations (nM) used in kinetic assay of Kemp eliminase.

pH	KABLE1	KABLE1 I12F	KABLE1 K14P	KABLE1 L20W	KABLE1 L118N	KABLE1.2	KABLE1.3	KABLE1.4
6		1000		1000	1000	100	100	5
6.5		1000	100	1000	1000	100	100	5
7	1000	1000	100	1000	1000	10	10	5
7.5	1000	1000	100	1000	1000	10	10	5
8	1000	1000	100	1000	1000	10	10	5
8.5	1000	1000	100	1000	1000	10	10	5
9	100	100	10	100	100	10	10	5
9.5	100	100		100	100	10	10	5
10	100	100		100	100	10	10	5

Table S6. Ca RMSD of designed KABLE1, Chai1 prediction of 6NBT-bound structures, and each monomer of its 2 crystal structures. (PDB: 9N0I,9N0J)

	9N0I_A	9N0I_B	9N0I_C	9N0I_D	9N0I E	9N0I F	9N0J_A	KABLE1_Chai1	KABLE12cryst_Chai1	KABLE1_Design
9N0I_A		0.5	0.4	0.6	0.5	0.6	0.6	0.7	0.6	0.8
9N0I_B	0.5		0.3	0.5	0.5	0.6	0.4	0.7	0.6	0.9
9N0I_C	0.4	0.3		0.4	0.5	0.5	0.4	0.7	0.5	0.8
9N0I_D	0.6	0.5	0.4		0.3	0.3	0.6	0.7	0.4	1.1
9N0I_E	0.5	0.5	0.5	0.3		0.4	0.7	0.7	0.5	1.0
9N0I_F	0.6	0.6	0.5	0.3	0.4		0.7	0.7	0.4	1.1
9N0J_A	0.6	0.4	0.4	0.6	0.7	0.7		0.8	0.7	0.9
KABLE1_Chai1	0.7	0.7	0.7	0.7	0.7	0.7	0.8		0.5	0.7
KABLE12cryst_Chai1	0.6	0.6	0.5	0.4	0.5	0.4	0.7	0.5		0.9
KABLE1_Design	0.8	0.9	0.8	1.1	1.0	1.1	0.9	0.7	0.9	

Table S7. Catalytic efficiency of KABLE1.4 for benzisoxazole derivative at pH 8.0 with the extinction coefficient at the wavelength maximum. pK_a values for salicylonitriles are listed at 30 ºC unless stated otherwise.

Benzisoxazole	pK_a of salicylonitrile[a]	λ_{max} (water)[c], nm (ϵ)	Catalytic efficiency, $M^{-1}s^{-1}$
1,2-benzisoxazole	6.9	325 (5,056)[d]	9 ± 4
4-nitrobenzisoxazole	5.2	405 (1,829)	12 ± 5
5-nitrobenzisoxazole	4.1	380 (15,800)	(2.32 ± 0.42) x 10^5
6-nitrobenzisoxazole	5.2	400 (2,980)	175 ± 107
5-aminobenzisoxazole	5.0, 8.3[b]	325 (2,820)	26 ± 1
5-fluorobenzisoxazole	6.8	335 (2,203)	145 ± 33
5-chlorobenzisoxazole	6.4	340 (3,315)	707 ± 191
5-bromobenzisoxazole	5.8	340 (3,277)	746 ± 157
5-iodobenzisoxazole	6.9[b]	340 (1,239)	1222 ± 293

[a]measured at 30 ºC unless otherwise mentioned (*69*).

[b]measured at 22 ºC in this research.

[c]measured in this research otherwise mentioned.

[d]measured at reference (*68*).

Table S8. Kinetic parameters of reported proteins catalyzing the Kemp elimination of 5-nitrobenzisoxazole with base-mediated mechanism.

Protein	Description	k_{cat}/K_M, $M^{-1}s^{-1}$	k_{cat}, s^{-1}	K_M, mM	Amino acid efficiency[a]	Ref
34E4	Catalytic antibody	5500	0.66	1.2	26	(*72*)
BSA	Natural lipid carrier	6500	6.02	ND	11	(*109*)
KE07	Computational redesign	12.2	0.018	1.4	0.05	(*29*)
KE59	Computational redesign	163	0.29	1.8	0.66	(*29*)
KE70	Computational redesign	78	0.16	2.1	0.31	(*29*)
KE07 R7 10/11G	7 round DE of KE07	2590	1.37	0.54	10	(*66*)
KE59 R13_3/11H	13 round DE of KE59	60,430	9.53	0.16	240	(*68*)
KE70 R8 15/11E	8 round DE of KE70	34,900	5.3	0.15	140	(*110*)
HG3	Computational redesign and rational engineering	425	0.68	1.6	1.4	(*32*)
HG3.17	17 round DE of HG3	150,000	604	3.5	500	(*30*, *31*)
HG3.R5	5 round DE of HG3	170,000	702	4.8	560	(*31*)
HG4	Ensemble-based redesign of HG3	103,000	ND	ND	340	(*35*)
HG649	Ensemble-based redesign of HG3	32,000	ND	ND	110	(*107*)
AlleyCat	Single mutation of Calmodulin	5.8	ND	ND	0.08	(*33*)
AlleyCat10	NMR-guided DE of AlleyCat7	4378	21.2	4.8	59	(*34*)
Lysozyme L99A/M102H	Double mutation of Lysozyme	1.8	ND	ND	0.01	(*111*)
GNCA4 W229D F290W	Double mutation of GNCA4	5497	10	ND	21	(*36*)
V4	DE of GNCA4 W229D F290W	200,000	635	3.14	710	(*112*)
KE15	Computational redesign	35	0.022	0.63	0.14	(*29*)
KE15 Tyr167Lys+ R4	Electrical field-guided design of KE15	403	0.31	0.77	1.6	(*63*)
tKSI	Natural enzyme	2.5	ND	ND	0.02	(*60*)

D38N tKSI	Single mutation of tKSI	17,000	ND	ND	140	(*60*)
Des27	Computational design	130	0.07	0.5	0.52	(*61*)
Des27.7	Computational redesign	12,700	2.85	0.21	51	(*61*)
F113L Des27.7	Single mutation on Des27.7	123,000	30	ND	490	(*61*)
KABLE1	De Novo Design	**6,600**	**6.6**	**0.99**	**57**	This work
KABLE1.4	Quadruple mutant of KABLE1	**600,000**	**800**	**1.33**	**4,800**	This work

[a]Amino acid catalytic efficiency, which is the quotient of catalytic efficiency (k_{cat}/K_M, $M^{-1}s^{-1}$), by the total number of amino acid for each proteins.

S9. Primer sequences used in this study.

Primer	Sequence
T7	TAATACGACTCACTATAGGG
T7_term	GCTAGTTATTGCTCAGCGG
Y9NNK	AAGTTTGAGGAG**NNK**GAGAAAATCGGG
I12NNK	GAGTATGAGAAA**NNK**GGGAAGCGTATT
K14NNK	GAGAAAATCGGG**NNK**CGTATTCTCGAA
I16NNK	ATCGGGAAGCGT**NNK**CTTGAACTGTTA
L17NNK	GGGAAGCGTATT**NNK**GAACTGTTACAG
L20NNK	ATTCTCGAACTG**NNK**CAGGAAGCCCGT
L42NNK	TTACTTCGGGAA**NNK**AAGGAGCTTTTT
F46NNK	TTAAAGGAGCTT**NNK**AAGAAGGATCTC
L50NNK	TTTAAGAAGGAT**NNK**AAGTTAGCTGAA
L52NNK	TTTAAGAAGGATCTCAAG**NNK**GCTGAA
Q75NNK	CTGCTGGAAGAA**NNK**CTCGAACGTCTC
L79NNK	CAGCTCGAACGT**NNK**AAGAAAATCCAG
I82NNK	CGTCTCAAGAAA**NNK**CAGGCGATGTTC
G112NNK	ATCATCGAGGAG**NNK**AAAGCACTTTTA
K113NNK	ATCGAGGAGGGG**NNK**GCACTTTTACCT
L115NNK	GAGGGGAAAGCA**NNK**TTACCTCTTGTG
L116NNK	GGGAAAGCACTT**NNK**CCTCTTGTGGAG
P117NNK	GGGAAAGCACTTTTA**NNK**CTTGTGGAG
L118NNK	GCACTTTTACCT**NNK**GTGGAGAAGATC
V119NNK	CTTTTACCTCTT**NNK**GAGAAGATCAAA

Table S10. Amino acid sequences of designed proteins and their mutants.

Protein	Amino acid sequence	DNA Sequence
FABLE	MHHHHHHENLYFQSIKSEFAEGAAVFVEG VAVFLTMMAAFQNGDKEAVAQYLARGASL YTRHEELLNRLLQKLRREGNKEAVTLMNE FTATFQTGKSLANALIAAFKNGDDDSFES YLQAIWKVIAKMATILDQIAKAI	ATGCACCACCACCACCACCACGA AAACCTGTACTTCCAGTCAATCA AGAGCGAGTTCGCCGAGGGGGCG GCTGTATTTGTAGAAGGCGTCGC CGTGTTTCTGACCATGATGGCCG CATTTCAGAACGGCGATAAGGAG GCTGTCGCACAGTACCTCGCGCG GGGGGCTTCCCTGTACACCCGTC ACGAGGAGTTGCTGAACCGGCTT TTACAAAAGTTGCGGCGCGAAGG GAACAAAGAAGCAGTGACTCTTA TGAACGAATTTACCGCCACTTTT CAAACTGGTAAGTCCTTAGCTAA TGCTCTGATCGCGGCATTCAAAA ATGGTGACGATGACTCCTTTGAA AGTTACCTTCAAGCAATCTGGAA GGTCATCGCCAAGATGGCAACTA TTTTGGATCAAATTGCAAAAGCA ATT
KABLE0	MHHHHHHENLYFQSLKELFEEWLEVRKKID EVFDAMKAAFEAGDMKTVGEYIKELKELYK EYLAMLEELLRRARALGLEEAVALLEEYKG LVEEASKAFEAAVKAFEAGDWAAFKKYLEK EEEIRKKMEPLVKALEEAL	ATGCACCACCACCACCACCACGA AAACCTGTACTTCCAGAGCTTAA AAGAGTTATTTGAAGAGTGGTTG GAAGTTCGTAAGAAGATTGATGA AGTATTCGATGCAATGAAGGCCG CTTTCGAGGCCGGGGATATGAAA ACAGTGGGGGAGTATATCAAAGA ATTGAAGGAACTTTATAAAGAAT ACTTAGCTATGCTTGAGGAGTTG CTCCGGCGTGCTCGTGCCTTAGG TCTTGAAGAGGCAGTCGCATTAC TGGAAGAGTACAAAGGGTTAGTC GAGGAGGCATCGAAGGCTTTTGA AGCTGCCGTAAAAGCTTTCGAGG CTGGGGACTGGGCCGCCTTCAAA AAATACCTTGAGAAGGAAGAGGA GATCCGCAAAAAGATGGAACCGC TCGTCAAAGCCCTGGAAGAGGCA CTC
KABLE1	MHHHHHHENLYFQSSLKEKFEEYEKIGKRI LELLQEARDAFEAGDLARVDELLRELKELF KKDLKLAEEMKKEAEEAGNKEAVELLEEQL ERLKKIQAMFEEAVEAFRAGDRERFGELLE KIIEEGKALLPLVEKIKEAI	ATGCACCACCACCACCACCACGA AAACCTGTACTTCCAGAGCAGCC TCAAAGAAAAGTTTGAGGAGTAT GAGAAAATCGGGAAGCGTATTCT CGAACTGTTACAGGAAGCCCGTG ACGCTTTCGAGGCTGGTGATCTC GCGCGGGTTGATGAGTTACTTCG GGAATTAAAGGAGCTTTTTAAGA AGGATCTCAAGTTAGCTGAAGAA

		ATGAAAAAGGAAGCGGAAGAAGC TGGGAATAAAGAGGCGGTGGAGC TGCTGGAAGAACAGCTCGAACGT CTCAAGAAAATCCAGGCGATGTT CGAGGAGGCAGTTGAGGCGTTTC GGGCCGGGGACCGCGAGCGTTTT GGTGAGCTCCTCGAAAAGATCAT CGAGGAGGGGAAAGCACTTTTAC CTCTTGTGGAGAAGATCAAAGAG GCTATC
KABLE1.2	MHHHHHHENLYFQSSLKEKFEEYEKIGPRI LELWQEARDAFEAGDLARVDELLRELKELF KKDLKLAEEMKKEAEEAGNKEAVELLEEQL ERLKKIQAMFEEAVEAFRAGDRERFGELLE KIIEEGKALLPLVEKIKEAI	ATGCACCACCACCACCACCACGA AAACCTGTACTTCCAGAGCAGCC TCAAAGAAAAGTTTGAGGAGTAT GAGAAAATCGGGCCGCGTATTCT TGAACTGTGGCAGGAAGCCCGTG ACGCTTTCGAGGCTGGTGATCTC GCGCGGGTTGATGAGTTACTTCG GGAATTAAAGGAGCTTTTTAAGA AGGATCTCAAGTTAGCTGAAGAA ATGAAAAAGGAAGCGGAAGAAGC TGGGAATAAAGAGGCGGTGGAGC TGCTGGAAGAACAGCTCGAACGT CTCAAGAAAATCCAGGCGATGTT CGAGGAGGCAGTTGAGGCGTTTC GGGCCGGGGACCGCGAGCGTTTT GGTGAGCTCCTCGAAAAGATCAT CGAGGAGGGGAAAGCACTTTTAC CTCTTGTGGAGAAGATCAAAGAG GCTATC
KABLE1.2$_{cryst}$	MHHHHHHENLYFQSSLKEKFAEYEAIGPRI LELWQAARNAFEAGDLARVANLLAELKELF KKDLNLANAMAAEAAEAGNKEAVALLAEQL ERLKKIQAMFAAAVNAFRAGDREAFGALLE AIINEGKALLPLVEAIKEAI	ATGCACCACCACCACCACCACGA AAACCTGTACTTCCAGAGCTCAC TGAAGGAGAAATTCGCCGAATAC GAGGCGATTGGGCCGCGGATTCT CGAATTGTGGCAGGCAGCGCGTA ATGCTTTCGAAGCTGGGGATCTC GCTCGGGTTGCCAATTTGCTTGC GGAATTGAAGGAACTGTTCAAGA AAGACCTGAATCTTGCGAACGCA ATGGCGGCCGAGGCGGCGGAAGC CGGGAATAAGGAAGCTGTAGCCC TTTTGGCGGAACAGCTTGAGCGG TTAAAGAAAATCCAGGCAATGTT CGCCGCGGCGGTGAATGCTTTCC GGGCGGGGGACCGCGAGGCATTT GGTGCATTGTTGGAGGCAATCAT CAACGAAGGCAAGGCTCTCTTAC CGCTCGTGGAGGCGATTAAGGAG GCCATC
KABLE1.3	MHHHHHHENLYFQSSLKEKFEEYEKFGPRI LELWQEARDAFEAGDLARVDELLRELKELF KKDLKLAEEMKKEAEEAGNKEAVELLEEQL ERLKKIQAMFEEAVEAFRAGDRERFGELLE KIIEEGKALLPLVEKIKEAI	ATGCACCACCACCACCACCACGA AAACCTGTACTTCCAGAGCAGCC TCAAAGAAAAGTTTGAGGAGTAT GAGAAATTTGGGCCGCGTATTCT TGAACTGTGGCAGGAAGCCCGTG ACGCTTTCGAGGCTGGTGATCTC

		GCGCGGGTTGATGAGTTACTTCG GGAATTAAAGGAGCTTTTTAAGA AGGATCTCAAGTTAGCTGAAGAA ATGAAAAAGGAAGCGGAAGAAGC TGGGAATAAAGAGGCGGTGGAGC TGCTGGAAGAACAGCTCGAACGT CTCAAGAAAATCCAGGCGATGTT CGAGGAGGCAGTTGAGGCGTTTC GGGCCGGGGACCGCGAGCGTTTT GGTGAGCTCCTCGAAAAGATCAT CGAGGAGGGGAAAGCACTTTTAC CTCTTGTGGAGAAGATCAAAGAG GCTATC
KABLE1.4	MHHHHHHENLYFQSSLKEKFEEYEKFGPRI LELWQEARDAFEAGDLARVDELLRELKELF KKDLKLAEEMKKEAEEAGNKEAVELLEEQL ERLKKIQAMFEEAVEAFRAGDRERFGELLE KIIEEGKALLPNVEKIKEAI	ATGCACCACCACCACCACCACGA AAACCTGTACTTCCAGAGCAGCC TCAAAGAAAAGTTTGAGGAGTAT GAGAAATTTGGGCCGCGTATTCT TGAACTGTGGCAGGAAGCCCGTG ACGCTTTCGAGGCTGGTGATCTC GCGCGGGTTGATGAGTTACTTCG GGAATTAAAGGAGCTTTTTAAGA AGGATCTCAAGTTAGCTGAAGAA ATGAAAAAGGAAGCGGAAGAAGC TGGGAATAAAGAGGCGGTGGAGC TGCTGGAAGAACAGCTCGAACGT CTCAAGAAAATCCAGGCGATGTT CGAGGAGGCAGTTGAGGCGTTTC GGGCCGGGGACCGCGAGCGTTTT GGTGAGCTCCTCGAAAAGATCAT CGAGGAGGGGAAAGCACTTTTAC CTAACGTGGAGAAGATCAAAGAG GCTATC

Supplemental text

Computational design of FABLE_RosettaScript(.xml)

```
<ROSETTASCRIPTS>
  <SCOREFXNS>
    <ScoreFunction name="ligand_soft_rep" weights="ligand_soft_rep" />
    <ScoreFunction name="hard_rep" weights="ligandprime" />
    <ScoreFunction name="ref15" weights="ref2015">
      <Reweight scoretype="atom_pair_constraint" weight="5"/>
    </ScoreFunction>
    <ScoreFunction name="ref15_1" weights="ref2015">
      <Reweight scoretype="aa_composition" weight="1" />
      <Reweight scoretype="netcharge" weight="1.0" />
      <Reweight scoretype="atom_pair_constraint" weight="5"/>
      <Set aa_composition_setup_file="helix_composition.comp" />
      <Set netcharge_setup_file="helix_netcharge.charge" />
    </ScoreFunction>
  </SCOREFXNS>
  <RESIDUE_SELECTORS>
  </RESIDUE_SELECTORS>
  <TASKOPERATIONS>
    <InitializeFromCommandline name="ifcl"/>
    <ReadResfile name="resfile" filename="resfile_topology.txt"/>
    <ExtraRotamersGeneric name="extrachi" ex1="1" ex2="1" ex1_sample_level="1" ex2_sample_level="1"
extrachi_cutoff="14"/>
    <DetectProteinLigandInterface name="design_interface" cut1="6.0" cut2="8.0" cut3="10.0" cut4="12.0"
design="1" resfile="resfile_topology.txt" />
    IncludeCurrent name="include_curr" />
  </TASKOPERATIONS>
  <FILTERS>
    <PackStat name="pstat" confidence="0" threshold="0" repeats="10"/>
    <PackStat name="pstat_mc" threshold="0" repeats="10"/>
    <NetCharge name="net_charge" confidence="0"/>
    <LigInterfaceEnergy name="ligen"  scorefxn="ref15" include_cstE="0" energy_cutoff="0" confidence="0"/>
    <ScoreType name="total_score_1" scorefxn="ref15_1" score_type="total_score" threshold="0"/>
    <ScoreType name="total_score" scorefxn="ref15" score_type="total_score" threshold="0"/>
    <BuriedUnsatHbonds name="bu" report_sc_heavy_atom_unsats="true" scorefxn="ref15" cutoff="0"
residue_surface_cutoff="20.0" ignore_surface_res="true" print_out_info_to_pdb="true" confidence="0" />
  </FILTERS>
  <LIGAND_AREAS>
    <LigandArea name="docking_sidechain" chain="X" cutoff="6.0" add_nbr_radius="true"
all_atom_mode="true" minimize_ligand="10" />
    <LigandArea name="final_sidechain" chain="X" cutoff="6.0" add_nbr_radius="true" all_atom_mode="true"
/>
    <LigandArea name="final_backbone" chain="X" cutoff="7.0" add_nbr_radius="false" all_atom_mode="true"
Calpha_restraints="0.3" />
  </LIGAND_AREAS>
  <INTERFACE_BUILDERS>
    <InterfaceBuilder name="side_chain_for_docking" ligand_areas="docking_sidechain" />
    <InterfaceBuilder name="side_chain_for_final" ligand_areas="final_sidechain" />
    <InterfaceBuilder name="backbone" ligand_areas="final_backbone" extension_window="3" />
  </INTERFACE_BUILDERS>
  <MOVEMAP_BUILDERS>
```

```
    <MoveMapBuilder name="docking" sc_interface="side_chain_for_docking" minimize_water="true" />
    <MoveMapBuilder name="final" sc_interface="side_chain_for_final" bb_interface="backbone"
minimize_water="true" />
  </MOVEMAP_BUILDERS>
  <SCORINGGRIDS ligand_chain="X" width="46">
    <ClassicGrid grid_name="vdw" weight="1.0" />
  </SCORINGGRIDS>
  <MOVERS>
    <ConstraintSetMover name="atomic" cst_file="constraints_helix.cst" />
    FavorNativeResidue name="favor_native" bonus="0.00" />
    <Transform name="transform" chain="X" box_size="10.0" move_distance="0.1" angle="5" cycles="500"
repeats="1" temperature="5" rmsd="4.0" use_constraints="true" cst_fa_file="constraints_helix.cst"
cst_fa_weight="5" />
    HighResDocker name="high_res_docker" cycles="6" repack_every_Nth="3" scorefxn="ligand_soft_rep"
movemap_builder="docking" />
    <PackRotamersMover name="design_interface" scorefxn="hard_rep" task_operations="design_interface" />
    FinalMinimizer name="final" scorefxn="hard_rep" movemap_builder="final" />
    <InterfaceScoreCalculator name="add_scores" chains="X" scorefxn="hard_rep" />
    <ParsedProtocol name="low_res_dock">
      <Add mover_name="transform" />
    </ParsedProtocol>
    ParsedProtocol name="high_res_dock">
      Add mover_name="high_res_docker" />
      Add mover_name="final" />
    /ParsedProtocol>
    <PackRotamersMover name="fixbb_aro" scorefxn="ref15_1" task_operations="resfile,extrachi,ifcl"/>
    <PackRotamersMover name="pack" scorefxn="ref15_1" task_operations="ifcl,resfile,extrachi"/>
    <PackRotamersMover name="pack_fast" scorefxn="ref15_1" task_operations="ifcl,resfile"/>
    <MinMover name="min_bb" scorefxn="ref15" tolerance="0.0000001" max_iter="1000" chi="false"
bb="true">
      <MoveMap name="map_bb">
        <Span begin="1" end="200" bb="true" chi="false" />
        <Span begin="201" end="999" bb="false" chi="false"/>
      </MoveMap>
    </MinMover>
    <Idealize name="idealize"/>
    <MinMover name="min_sc" scorefxn="ref15" tolerance="0.0000001" max_iter="1000" chi="true"
bb="false">
      <MoveMap name="map_sc">
        <Span begin="1" end="200" bb="false" chi="true" />
        <Span begin="201" end="999" bb="false" chi="false"/>
      </MoveMap>
    </MinMover>
    <MinMover name="min_sc_bb" scorefxn="ref15" tolerance="0.0000001" max_iter="1000" chi="true"
bb="true">
      <MoveMap name="map_sc_bb">
        <Span begin="1" end="200" bb="true" chi="true" />
        <Span begin="201" end="999" bb="false" chi="false"/>
      </MoveMap>
    </MinMover>
    <ParsedProtocol name="parsed_pack_fast" >
      <Add mover_name="pack_fast"/>
      <Add mover_name="min_bb"/>
    </ParsedProtocol>
    <ParsedProtocol name="parsed_pack" >
      <Add mover_name="pack"/>
```

```
        <Add mover_name="min_bb"/>
        <Add mover_name="min_sc"/>
    </ParsedProtocol>
    <GenericMonteCarlo name="pack_mc" preapply="0" trials="3" temperature="0.03" filter_name="pstat_mc"
sample_type="high" mover_name="parsed_pack">
        <Filters>
            <AND filter_name="total_score_1" temperature="15" sample_type="low"/>
        </Filters>
    </GenericMonteCarlo>
    <GenericMonteCarlo name="pack_fast_mc" preapply="0" trials="2" temperature="0.03"
filter_name="pstat_mc" sample_type="high" mover_name="parsed_pack_fast">
        <Filters>
            <AND filter_name="total_score_1" temperature="15" sample_type="low"/>
        </Filters>
    </GenericMonteCarlo>
  </MOVERS>
  <PROTOCOLS>
    <Add mover="atomic"/>
    Add mover_name="favor_native" />
    <Add mover_name="fixbb_aro"/>
    <Add mover_name="low_res_dock" />
    <Add mover_name="design_interface" />
    Add mover_name="high_res_dock" />
    <Add mover_name="parsed_pack_fast"/>
    <Add mover_name="pack_fast_mc"/>
    <Add mover_name="pack_mc"/>
    <Add mover_name="min_sc_bb"/>
    Add mover_name="low_res_dock" />
    Add mover_name="design_interface" />
    Add mover_name="high_res_dock" />
    <Add mover_name="add_scores" />
    <Add filter_name="pstat"/>
    <Add filter_name="net_charge"/>
    <Add filter_name="ligen"/>
    <Add filter_name="total_score"/>
    <Add filter_name="bu"/>
  </PROTOCOLS>
  <OUTPUT scorefxn="ref15_1"/>
</ROSETTASCRIPTS>
```

Computational design of FABLE_Flag(.txt)

-out:path:pdb output
-out:path:score output
-extra_res_fa cou485.params
-packing:multi_cool_annealer 10
-packing:linmem_ig 10
-ignore_zero_occupancy false
-s able128_cou485.pdb

Computational design of FABLE_Command line inputs

~/rosetta_bin_linux_2020.08.61146_bundle/main/source/bin/rosetta_scripts.static.linuxgccrelease -database /wynton/home/degradolab/lonelu/rosetta_bin_linux_2020.08.61146_bundle/main/database/ -parser:protocol rscript_dock_fixbb_design_round1.xml @options_helix_1.txt -run:constant_seed -run:jran $SGE_TASK_ID -out:suffix _$SGE_TASK_ID -out:no_nstruct_label

Computational design of FABLE_constraints (.cst)

AtomPair O2 1X ND1 49A HARMONIC 3.0 0.2
AtomPair C8 1X ND1 49A HARMONIC 3.7 0.2
Angle ND1 49A O2 1X C10 1X HARMONIC 1.91 0.12
Dihedral ND1 49A O2 1X C10 1X O1 1X CIRCULARHARMONIC 3.14 0.17

Computational design of FABLE_net charge (.charge)

DESIRED_CHARGE -5 #Desired net charge is zero.
PENALTIES_CHARGE_RANGE -10 -1 #Penalties are listed in the observed net charge range of -2 to +4.
PENALTIES 10 0 0 0 0 0 0 0 0 10 #The penalties are 10 for an observed charge of -2, 0 for an observed charge of -1 to +3, and 10 for an observed charge of +4.
BEFORE_FUNCTION QUADRATIC #Ramp quadratically for observed net charges of -3 or less.
AFTER_FUNCTION QUADRATIC #Ramp quadratically for observed net charges of +5 or greater.

Computational design of FABLE_resfile (.txt)

```
NATRO
ALLAAxc
NOTAA MTC
USE_INPUT_SC
start

1 A PIKAA S
2 A PIKAA TGIFYALSWVHM
3 A PIKAA K
4 A PIKAA S
5 A PIKAA E
6 A PIKAA TGIFYALSWVHM
7 A PIKAA A
8 A PIKAA E
9 A PIKAA TGIFYALSWVMH
10 A PIKAA KVSNLFRTDYAQWEIGHM
11 A PIKAA A
12 A PIKAA V
13 A PIKAA TGIFYALSWVH
14 A PIKAA KVSNLFRTDYAQWEIGHM
15 A PIKAA E
16 A PIKAA TGIFYALSWVNQH
17 A PIKAA KVSNLFRTDYAQWEIGHM
18 A PIKAA A
19 A PIKAA V
20 A PIKAA TGIFYALSWVHM
21 A PIKAA KVSNLFRTDYAQWEIGHM
22 A PIKAA T
23 A PIKAA TGIFYALSWVMH
24 A PIKAA KVSNLFRTDYAQWEIGHM
25 A PIKAA A
26 A PIKAA A
27 A PIKAA TGIFYALSWVHM
28 A PIKAA Q
29 A PIKAA N
30 A PIKAA G
31 A PIKAA D
32 A PIKAA K
33 A PIKAA E
34 A PIKAA A
35 A PIKAA TGIFYALSWVHM
36 A PIKAA A
37 A PIKAA Q
38 A PIKAA Y
39 A PIKAA TGIFYALSWVMH
40 A PIKAA A
41 A PIKAA R
42 A PIKAA TGIFYALSWVMNQH
43 A PIKAA A
44 A PIKAA S
45 A PIKAA L
46 A NATRO
47 A PIKAA T
48 A PIKAA R
49 A NATRO
```

50 A PIKAA E
51 A PIKAA E
52 A PIKAA L
53 A PIKAA TGIFYALSWVHM
54 A PIKAA N
55 A PIKAA R
56 A PIKAA TGIFYALSWVHM
57 A PIKAA L
58 A PIKAA Q
59 A PIKAA K
60 A PIKAA TGIFYALSWVHM
61 A PIKAA R
62 A PIKAA R
63 A PIKAA E
64 A PIKAA G
65 A PIKAA N
66 A PIKAA K
67 A PIKAA E
68 A PIKAA TGIFYALSWVHM
69 A PIKAA V
70 A PIKAA T
71 A PIKAA L
72 A PIKAA TGIFYALSWVHM
73 A PIKAA N
74 A PIKAA E
75 A PIKAA TGIFYALSWVHM
76 A PIKAA T
77 A PIKAA A
78 A PIKAA KVSNLFRTDYAQWEIGHM
79 A PIKAA TGIFYALSWVHM
80 A PIKAA Q
81 A PIKAA T
82 A PIKAA G
83 A PIKAA K
84 A PIKAA S
85 A PIKAA KVSNLFRTDYAQWEIGHM
86 A PIKAA TGIFYALSWVNQHM
87 A PIKAA N
88 A PIKAA A
89 A PIKAA TGIFYALSWVMH
90 A PIKAA KVSNLFRTDYAQWEIGHM
91 A PIKAA A
92 A PIKAA A
93 A PIKAA TGIFYALSWVMH
94 A PIKAA K
95 A PIKAA N
96 A PIKAA G
97 A PIKAA D
98 A PIKAA D
99 A PIKAA D
100 A PIKAA S
101 A PIKAA TGIFYALSWVMH
102 A PIKAA E
103 A PIKAA S
104 A PIKAA KVSNLFRTDYAQWEIGHM
105 A PIKAA VSNLFTYAQWIGHM

106 A PIKAA Q
107 A PIKAA A
108 A PIKAA TGIFYALSWVNQHM
109 A PIKAA KVSNLFRTDYAQWEIGHM
110 A PIKAA K
111 A PIKAA KVSNLFRTDYAQWEIGHM
112 A PIKAA VSNLFTYAQWIGHM
113 A PIKAA A
114 A PIKAA K
115 A PIKAA KVSNLFRTDYAQWEIGHM
116 A PIKAA KVSNLFRTDYAQWEIGHM
117 A PIKAA T
118 A PIKAA KVSNLFRTDYAQWEIGHM
119 A PIKAA TGIFYALSWVHM
120 A PIKAA KVSNLFRTDYAQWEIGHM
121 A PIKAA Q
122 A PIKAA TGIFYALSWVNQHM
123 A PIKAA A
124 A PIKAA K
125 A PIKAA A
126 A PIKAA VSNLFTYAQWIGHM

Computational design of FABLE cou485 parameters (.params)

```
NAME cou
IO_STRING cou Z
TYPE LIGAND
AA UNK
ATOM  C2  aroC  X   -0.02
ATOM  O1  Oaro  X   -0.57
ATOM  C10 COO   X   0.71
ATOM  O2  OOC   X   -0.67
ATOM  C8  aroC  X   -0.02
ATOM  C4  aroC  X   -0.02
ATOM  C1  aroC  X   -0.02
ATOM  C6  aroC  X   -0.02
ATOM  C7  aroC  X   -0.02
ATOM  C3  aroC  X   -0.02
ATOM  N1  Nhis  X   -0.44
ATOM  C11 CH3   X   -0.18
ATOM  H5  Hapo  X   0.19
ATOM  H6  Hapo  X   0.19
ATOM  H7  Hapo  X   0.19
ATOM  C12 CH3   X   -0.18
ATOM  H8  Hapo  X   0.19
ATOM  H9  Hapo  X   0.19
ATOM  H10 Hapo  X   0.19
ATOM  C5  aroC  X   -0.02
ATOM  H1  Haro  X   0.21
ATOM  H3  Haro  X   0.21
ATOM  H2  Haro  X   0.21
ATOM  C9  CH1   X   0.00
ATOM  F1  F     X   -0.16
ATOM  F2  F     X   -0.16
ATOM  F3  F     X   -0.16
ATOM  H4  Haro  X   0.21
BOND_TYPE  F1   C9  1
BOND_TYPE  F2   C9  1
BOND_TYPE  F3   C9  1
BOND_TYPE  O1   C2  1
BOND_TYPE  O1   C10 1
BOND_TYPE  O2   C10 2
BOND_TYPE  N1   C3  1
BOND_TYPE  N1   C11 1
BOND_TYPE  N1   C12 1
BOND_TYPE  C1   C2  2
BOND_TYPE  C1   C4  1
BOND_TYPE  C1   C6  1
BOND_TYPE  C2   C5  1
BOND_TYPE  C3   C5  2
BOND_TYPE  C3   C7  1
BOND_TYPE  C4   C8  2
BOND_TYPE  C4   C9  1
BOND_TYPE  C5   H1  1
BOND_TYPE  C6   C7  2
BOND_TYPE  C6   H2  1
BOND_TYPE  C7   H3  1
BOND_TYPE  C8   C10 1
BOND_TYPE  C8   H4  1
```

```
BOND_TYPE  C11  H5  1
BOND_TYPE  C11  H6  1
BOND_TYPE  C11  H7  1
BOND_TYPE  C12  H8  1
BOND_TYPE  C12  H9  1
BOND_TYPE  C12  H10 1
CHI 1  C7   C3   N1   C11
CHI 2  C8   C4   C9   F1
NBR_ATOM  C2
NBR_RADIUS 5.923196
ICOOR_INTERNAL    C2     0.000000    0.000000    0.000000   C2    O1    C10
ICOOR_INTERNAL    O1     0.000000  180.000000    1.409420   C2    O1    C10
ICOOR_INTERNAL    C10    0.000000   58.463932    1.386066   O1    C2    C10
ICOOR_INTERNAL    O2   179.925876   57.937170    1.226078   C10   O1    C2
ICOOR_INTERNAL    C8  -179.925892   63.301065    1.472680   C10   O1    O2
ICOOR_INTERNAL    C4    -0.015728   56.938781    1.340468   C8    C10   O1
ICOOR_INTERNAL    C1     0.014038   61.035345    1.469219   C4    C8    C10
ICOOR_INTERNAL    C6  -179.980373   56.250303    1.401339   C1    C4    C8
ICOOR_INTERNAL    C7   179.987003   59.272543    1.399558   C6    C1    C4
ICOOR_INTERNAL    C3    -0.002786   59.626591    1.393812   C7    C6    C1
ICOOR_INTERNAL    N1  -179.998592   59.914843    1.409634   C3    C7    C6
ICOOR_INTERNAL    C11  -29.995192   59.285655    1.444938   N1    C3    C7
ICOOR_INTERNAL    H5  -160.400020   68.664840    1.095868   C11   N1    C3
ICOOR_INTERNAL    H6   118.861740   68.474544    1.096109   C11   N1    H5
ICOOR_INTERNAL    H7   121.608625   69.215932    1.095223   C11   N1    H6
ICOOR_INTERNAL    C12  179.691253   59.261398    1.444710   N1    C3    C11
ICOOR_INTERNAL    H8    79.879643   69.218588    1.095174   C12   N1    C3
ICOOR_INTERNAL    H9   119.524176   68.641682    1.095983   C12   N1    H8
ICOOR_INTERNAL    H10  118.889069   68.492185    1.095932   C12   N1    H9
ICOOR_INTERNAL    C5   179.996131   60.228042    1.390873   C3    C7    N1
ICOOR_INTERNAL    H1   179.316588   58.204851    1.086138   C5    C3    C7
ICOOR_INTERNAL    H3  -179.255672   61.873585    1.087037   C7    C6    C3
ICOOR_INTERNAL    H2  -179.746324   51.829077    1.075641   C6    C1    C7
ICOOR_INTERNAL    C9   179.986364   58.867821    1.500828   C4    C8    C1
ICOOR_INTERNAL    F1    59.996833   68.979155    1.347636   C9    C4    C8
ICOOR_INTERNAL    F2   120.009390   69.167204    1.347464   C9    C4    F1
ICOOR_INTERNAL    F3   119.943271   69.078969    1.347408   C9    C4    F2
ICOOR_INTERNAL    H4   179.999796   63.686307    1.085843   C8    C10   C4
```

Computational design of FABLE composition (.comp)

```
TYPE THR
DELTA_START 0
DELTA_END 1
PENALTIES 0 100
ABSOLUTE 5
BEFORE_FUNCTION CONSTANT
AFTER_FUNCTION QUADRATIC
END_PENALTY_DEFINITION

PENALTY_DEFINITION
TYPE GLY
DELTA_START 0
DELTA_END 1
PENALTIES 0 100
ABSOLUTE 9
BEFORE_FUNCTION CONSTANT
AFTER_FUNCTION QUADRATIC
END_PENALTY_DEFINITION

PENALTY_DEFINITION
TYPE SER
DELTA_START 0
DELTA_END 1
PENALTIES 0 100
ABSOLUTE 5
BEFORE_FUNCTION CONSTANT
AFTER_FUNCTION QUADRATIC
END_PENALTY_DEFINITION

PENALTY_DEFINITION
TYPE ASN
DELTA_START 0
DELTA_END 1
PENALTIES 0 100
ABSOLUTE 8
BEFORE_FUNCTION CONSTANT
AFTER_FUNCTION QUADRATIC
END_PENALTY_DEFINITION

PENALTY_DEFINITION
TYPE ARG
DELTA_START 0
DELTA_END 1
PENALTIES 0 100
ABSOLUTE 8
BEFORE_FUNCTION CONSTANT
AFTER_FUNCTION QUADRATIC
END_PENALTY_DEFINITION

PENALTY_DEFINITION
TYPE ALA
DELTA_START 0
DELTA_END 1
PENALTIES 0 100
ABSOLUTE 18
```

```
BEFORE_FUNCTION CONSTANT
AFTER_FUNCTION QUADRATIC
END_PENALTY_DEFINITION

PENALTY_DEFINITION
TYPE TRP
DELTA_START 0
DELTA_END 1
PENALTIES 0 100
ABSOLUTE 3
BEFORE_FUNCTION CONSTANT
AFTER_FUNCTION QUADRATIC
END_PENALTY_DEFINITION

PENALTY_DEFINITION
TYPE LYS
DELTA_START 0
DELTA_END 1
PENALTIES 0 100
ABSOLUTE 8
BEFORE_FUNCTION CONSTANT
AFTER_FUNCTION QUADRATIC
END_PENALTY_DEFINITION

PENALTY_DEFINITION
TYPE GLN
DELTA_START 0
DELTA_END 1
PENALTIES 0 100
ABSOLUTE 8
BEFORE_FUNCTION CONSTANT
AFTER_FUNCTION QUADRATIC
END_PENALTY_DEFINITION

PENALTY_DEFINITION
TYPE TYR
DELTA_START 0
DELTA_END 1
PENALTIES 0 100
ABSOLUTE 8
BEFORE_FUNCTION CONSTANT
AFTER_FUNCTION QUADRATIC
END_PENALTY_DEFINITION

PENALTY_DEFINITION
TYPE GLU
DELTA_START 0
DELTA_END 1
PENALTIES 0 100
ABSOLUTE 8
BEFORE_FUNCTION CONSTANT
AFTER_FUNCTION QUADRATIC
END_PENALTY_DEFINITION

PENALTY_DEFINITION
TYPE ASP
```

```
DELTA_START 0
DELTA_END 1
PENALTIES 0 100
ABSOLUTE 9
BEFORE_FUNCTION CONSTANT
AFTER_FUNCTION QUADRATIC
END_PENALTY_DEFINITION

PENALTY_DEFINITION
TYPE VAL
DELTA_START 0
DELTA_END 1
PENALTIES 0 100
ABSOLUTE 12
BEFORE_FUNCTION CONSTANT
AFTER_FUNCTION QUADRATIC
END_PENALTY_DEFINITION

PENALTY_DEFINITION
TYPE MET
DELTA_START 0
DELTA_END 1
PENALTIES 0 100
ABSOLUTE 8
BEFORE_FUNCTION CONSTANT
AFTER_FUNCTION QUADRATIC
END_PENALTY_DEFINITION
```

KABLE_Design_Strategy_1_Constraints

```
AtomPair N3 1X OE2 108A HARMONIC 2.5 0.1
Dihedral N1 1X N2 1X N3 1X OE2 108A CIRCULARHARMONIC 3.14 0.17
Angle OE2 108A N3 1X N2 1X HARMONIC 1.92 0.17
Angle CD 108A OE2 108A N3 1X HARMONIC 1.92 0.17
```

KABLE_Design_Strategy_2_Constraints

```
AtomPair N3 1X OD2 49A HARMONIC 2.5 0.1
Dihedral N1 1X N2 1X N3 1X OD2 49A CIRCULARHARMONIC 3.14 0.17
Dihedral CB 49A CG 49A OD2 49A N3 1X CIRCULARHARMONIC 3.14 0.17
Angle OD2 49A N3 1X N2 1X HARMONIC 1.92 0.17
Angle CG 49A OD2 49A N3 1X HARMONIC 1.92 0.17
```

Example of KABLE_sequence_design_LigandMPNN

```
/home/degradolab/yuda/LigandMPNN/run.py \
    --model_type "ligand_mpnn" \
    --seed 111 \
    --pdb_path "… " \
    --out_folder "…" \
    --fixed_residues "A49" \
    --omit_AA "C" \
    --batch_size 2 \
    --number_of_batches 5 \
```

Example of KABLE_sequence_design_Rosetta FastRelax

```
~/rosetta_bin_linux_2020.08.61146_bundle/main/source/bin/relax.static.linuxgccrelease \
  -database ~ /rosetta_bin_linux_2020.08.61146_bundle/main/database/ \
  -in:file:s $pdb_filename \
  -extra_res_fa ~/…/ 6nt.params \
  -constraints:cst_fa_file ~/…/constraints.cst \
    -constraints:cst_fa_weight "5" \
  -relax:quick \
```

Extract_Chi1_and_Chi2.py

```
import os
import csv
from Bio.PDB import PDBParser
from Bio.PDB.vectors import calc_dihedral
import math

# Define a mapping of residue types to the atoms involved in chi1 and chi2 calculations
residue_atoms = {
    'default': [('N', 'CA', 'CB', 'CG'), ('CA', 'CB', 'CG', 'CD')],  # Default for most amino acids
    'TYR': [('N', 'CA', 'CB', 'CG'), ('CA', 'CB', 'CG', 'CD1')],  # Tyrosine
    'HIS': [('N', 'CA', 'CB', 'CG'), ('CA', 'CB', 'CG', 'ND1')],  # Histidine
    'ASP': [('N', 'CA', 'CB', 'CG'), ('CA', 'CB', 'CG', 'OD1')],  # Aspartic acid
    'GLN': [('N', 'CA', 'CB', 'CG'), ('CA', 'CB', 'CG', 'CD')],   # Glutamine
    'LEU': [('N', 'CA', 'CB', 'CG'), ('CA', 'CB', 'CG', 'CD1')],  # Leucine
    'ILE': [('N', 'CA', 'CB', 'CG1'), ('CA', 'CB', 'CG1', 'CD1')],  # Isoleucine
    'PHE': [('N', 'CA', 'CB', 'CG'), ('CA', 'CB', 'CG', 'CD1')],  # Phenylalanine
    'THR': [('N', 'CA', 'CB', 'OG1')],  # Threonine (chi1 only)
    # Add more residue types as needed
}

def calculate_dihedrals(pdb_file, residue_number, residue_type='default'):
    parser = PDBParser()
    structure = parser.get_structure('X', pdb_file)
    atom_pairs = residue_atoms.get(residue_type, residue_atoms['default'])
    chi1_atoms = atom_pairs[0]  # Chi1 is always the first set of atoms
    chi2_atoms = atom_pairs[1] if len(atom_pairs) > 1 else None  # Chi2 is optional
    for model in structure:
        for chain in model:
            for residue in chain:
                if residue.id[1] == residue_number:
                    try:
                        # Extract vectors for chi1 calculation
                        vectors_chi1 = [residue[x].get_vector() for x in chi1_atoms]
                        chi1 = calc_dihedral(*vectors_chi1)
                        chi1_deg = math.degrees(chi1)

                        # Extract vectors for chi2 calculation if available
                        chi2_deg = None
                        if chi2_atoms:
                            vectors_chi2 = [residue[x].get_vector() for x in chi2_atoms]
                            chi2 = calc_dihedral(*vectors_chi2)
                            chi2_deg = math.degrees(chi2)
                        return chi1_deg, chi2_deg
                    except KeyError:
                        # Atoms required not found
                        return None, None
    return None, None  # Residue not found

def process_directory(directory_path, residue_number, residue_type, output_csv):
    with open(output_csv, 'w', newline='') as csvfile:
        fieldnames = ['File Name', 'Chi1 (degrees)', 'Chi2 (degrees)']
        writer = csv.DictWriter(csvfile, fieldnames=fieldnames)
        writer.writeheader()

        for file in os.listdir(directory_path):
```

```
        if file.endswith(".pdb"):
            pdb_file_path = os.path.join(directory_path, file)
            chi1, chi2 = calculate_dihedrals(pdb_file_path, residue_number, residue_type)
            writer.writerow({'File Name': file, 'Chi1 (degrees)': chi1, 'Chi2 (degrees)': chi2 if chi2 is not None else
"N/A"})

# Example usage
directory_path =
'/Users/chenyuda/Documents/Code/ABLE_Fragment/fragment_paper/md_278k_hie_202404/chi1chi2_for_H49/all_
pdb_for_H49/'
residue_number = 49  # Example residue number
residue_type = 'HIS'  # Specify residue type here
output_csv = 'Chi1Chi2_md_Thr112_6w70_ABLE_6w6x_6w70_and_pdb.csv'
process_directory(directory_path, residue_number, residue_type, output_csv)
```

Generate_contour_from_tyr_chi1and2.py

```
import numpy as np
import pandas as pd
import matplotlib.pyplot as plt
from scipy.stats import gaussian_kde
from matplotlib.colors import LinearSegmentedColormap

def plot_density_contour(file_path, labels, x_range, y_range, contour_color, scatter_colors, contour_line_color,
bg_color='white', contour_alpha=0.6, contour_linewidth=3, symbol_sizes=None, output_file='density_contour.svg'):
    fig, ax = plt.subplots(figsize=(10, 8), facecolor=bg_color)
    ax.set_facecolor(bg_color)

    # Read the CSV file
    data_frame = pd.read_csv(file_path, header=None)

    # Extract group names
    group_names = data_frame.iloc[0, ::2].values

    # Process contour group (first group)
    chi1_contour = data_frame.iloc[1:, 0].dropna().values.astype(float)
    chi2_contour = data_frame.iloc[1:, 1].dropna().values.astype(float)
    data_contour = np.vstack([chi1_contour, chi2_contour])
    kde_contour = gaussian_kde(data_contour)
    x_min, x_max = x_range
    y_min, y_max = y_range
    x_grid, y_grid = np.mgrid[x_min:x_max:100j, y_min:y_max:100j]
    grid_coords = np.vstack([x_grid.ravel(), y_grid.ravel()])
    density_contour = kde_contour(grid_coords).reshape(x_grid.shape)
    cmap = LinearSegmentedColormap.from_list(f'custom_cmap_{labels[0]}', ['white', contour_color])
    contour_filled = ax.contourf(x_grid, y_grid, density_contour, levels=4, cmap=cmap, alpha=contour_alpha,
extend='both')
    contour_lines = ax.contour(x_grid, y_grid, density_contour, levels=4, colors=contour_line_color,
linewidths=contour_linewidth)
    ax.scatter(chi1_contour, chi2_contour, c=contour_color, s=symbol_sizes[0], label=labels[0])
    print(f"{labels[0]}: {len(chi1_contour)} points")

    # Process scatter groups (all other groups)
    for i in range(1, len(labels)):
        chi1_scatter = data_frame.iloc[1:, 2*i].dropna().values.astype(float)
        chi2_scatter = data_frame.iloc[1:, 2*i+1].dropna().values.astype(float)

        if len(chi1_scatter) == 0 or len(chi2_scatter) == 0:
            print(f"{labels[i]}: No data found")
            continue

        ax.scatter(chi1_scatter, chi2_scatter, c=scatter_colors[i-1], s=symbol_sizes[i], label=labels[i])
        print(f"{labels[i]}: {len(chi1_scatter)} points")

    # Add color bar for the filled contour
    plt.colorbar(contour_filled, ax=ax, label='Density')

    # Customizing the range for the x and y axes
    ax.set_xlim([x_min, x_max])
    ax.set_ylim([y_min, y_max])

    ax.set_xlabel('chi1')
```

```
    ax.set_ylabel('chi2')
    ax.set_title('Density Contour Plot of chi1 and chi2')
    ax.legend()

    # Save the plot as an SVG file
    plt.savefig(output_file, format='svg')
    print(f"Plot saved as {output_file}")

    plt.show()

# File path to the CSV file
file_path = '…' # Replace with your actual file path

# Labels for the datasets
labels = ['complexed ABLE MD Simulation', 'Uncomplexed ABLE', 'Uncomplexed ABLE H49A', 'ABLE-apixaban
complex']

# Colors for the contour plot
contour_color = '#F39191'

# Colors for the scatter plots
scatter_colors = ['#1873E5', '#59B358', '#5E4B56']

# Color for the contour lines
contour_line_color = '#ffc8c8'

# Custom ranges for x and y axes
x_range = [225, 340]
y_range = [-125, 50]

# Symbol sizes for the datasets (contour and five scatter plots)
symbol_sizes = [20, 80, 80, 80]

# Call the function with desired customizations and specify output file
output_file = '…'
plot_density_contour(file_path, labels, x_range, y_range, contour_color, scatter_colors, contour_line_color,
bg_color='white', contour_alpha=0.8, contour_linewidth=0.1, symbol_sizes=symbol_sizes, output_file=output_file)
```

Count_water.py.

```
import prody as pr
import matplotlib.pyplot as plt
import csv
#import warnings
#warnings.filterwarnings('ignore')

####### Script settings ######
discard_frames = […]

lig_dist = 3.5

traj_pdb_path = '…'

lig_chain = '…'

lig_resnum = 127

output_csv_file = '…'

######## Functions #######

def main():
    # Load MD trajectory
    traj_pdb = pr.parsePDB(traj_pdb_path)
    print('-'*20, 'Total number of frames in traj: ', len(traj_pdb.getCoordsets()), '-'*20)

    # Perform analysis
    num_waters_per_frame = [] # Each element in this list represents a single frame.
    num_frames_processed = 0
    # Iterate over each frame (model), which is a Coordset in prody
    for frame_ix, coordset in enumerate(traj_pdb.getCoordsets()):
        if frame_ix in discard_frames:
            continue
        num_frames_processed += 1
        # Make a standalone prody obj for each frame
        par = pr.atomic.atomgroup.AtomGroup()
        par.setCoords(coordset)
        par.setNames(traj_pdb.getNames())
        par.setResnames(traj_pdb.getResnames())
        par.setChids(traj_pdb.getChids())
        par.setResnums(traj_pdb.getResnums())
        par.setElements(traj_pdb.getElements())

        # Define ligand.
        if lig_chain:
            pr_lig = par.select(f'chain {lig_chain} and resnum {lig_resnum}')
        else:
            pr_lig = par.select(f'resnum {lig_resnum}')

        lig_resname = set(pr_lig.getResnames())
        lig_heavyatoms = pr_lig.select('not element H')
        if len(lig_resname) > 1:
            print(f'Note: more than one ligand selected. Residue names {lig_resname}.')
```

```
        if len(num_waters_per_frame) == 0:
            print(f'Ligand {lig_resname} selected with {len(lig_heavyatoms)} heavy atoms.')

        # Count waters in the active site, defined by a distance cutoff from the ligand.
        wat_neighbs = par.select(
                f'(water and name O) within {lig_dist} of Lig', Lig=pr_lig)
        if wat_neighbs is None:
            num_waters_in_frame = 0
        else:
            num_waters_in_frame = len(wat_neighbs)

        # Record the frame number (1-indexed) and the number of waters in that frame.
        num_waters_per_frame.append(tuple([frame_ix+1, num_waters_in_frame]))

    framenumbers = [i[0] for i in num_waters_per_frame]
    numberwaters = [i[1] for i in num_waters_per_frame]

    # Write out the results to a csv file.
    with open(output_csv_file, 'w', newline='') as csvfile:
        writer = csv.writer(csvfile)
        writer.writerow(['Frame #', '# waters'])
        for frame, waters in zip(framenumbers, numberwaters):
            writer.writerow([frame, waters])

    # Plot
    plt.plot(framenumbers, numberwaters)
    plt.xlabel('Frame #')
    plt.ylabel('# waters in active site')
    plt.title(traj_pdb_path)
    plt.grid(True)
    plt.show()

    print(f'Number of frames processed: {num_frames_processed}')
    print(f'Number of frames discarded: {len(discard_frames)}')



######## Main #######
if __name__ == "__main__":
    main()
```

Reference

1. O. Khersonsky, D. S. Tawfik, Enzyme promiscuity: a mechanistic and evolutionary perspective. *Annu Rev Biochem* **79**, 471–505 (2010).

2. P. A. Romero, F. H. Arnold, Exploring protein fitness landscapes by directed evolution. *Nat Rev Mol Cell Biol* **10**, 866–876 (2009).

3. M. S. Packer, D. R. Liu, Methods for the directed evolution of proteins. *Nat Rev Genet* **16**, 379–394 (2015).

4. M. L. Romero Romero, A. Rabin, D. S. Tawfik, Functional Proteins from Short Peptides: Dayhoff's Hypothesis Turns 50. *Angew Chem Int Ed Engl* **55**, 15966–15971 (2016).

5. N. Tokuriki, D. S. Tawfik, Protein dynamism and evolvability. *Science* **324**, 203–207 (2009).

6. S. Mallik, D. S. Tawfik, E. D. Levy, How gene duplication diversifies the landscape of protein oligomeric state and function. *Curr Opin Genet Dev* **76**, 101966 (2022).

7. P. L. Bedard, D. M. Hyman, M. S. Davids, L. L. Siu, Small molecules, big impact: 20 years of targeted therapy in oncology. *The Lancet* **395**, 1078–1088 (2020).

8. L. An, M. Said, L. Tran, S. Majumder, I. Goreshnik, G. R. Lee, D. Juergens, J. Dauparas, I. Anishchenko, B. Coventry, A. K. Bera, A. Kang, P. M. Levine, V. Alvarez, A. Pillai, C. Norn, D. Feldman, D. Zorine, D. R. Hicks, X. Li, M. G. Sanchez, D. K. Vafeados, P. J. Salveson, A. A. Vorobieva, D. Baker, Binding and sensing diverse small molecules using shape-complementary pseudocycles. *Science* **385**, 276–282 (2024).

9. I. V. Korendovych, W. F. DeGrado, De novo protein design, a retrospective. *Quarterly Reviews of Biophysics* **53**, e3 (2020).

10. W. Yang, L. Lai, Computational design of ligand-binding proteins. *Current Opinion in Structural Biology* **45**, 67–73 (2017).

11. C. E. Tinberg, S. D. Khare, J. Dou, L. Doyle, J. W. Nelson, A. Schena, W. Jankowski, C. G. Kalodimos, K. Johnsson, B. L. Stoddard, D. Baker, Computational design of ligand-binding proteins with high affinity and selectivity. *Nature* **501**, 212–216 (2013).

12. J. Dou, A. A. Vorobieva, W. Sheffler, L. A. Doyle, H. Park, M. J. Bick, B. Mao, G. W. Foight, M. Y. Lee, L. A. Gagnon, L. Carter, B. Sankaran, S. Ovchinnikov, E. Marcos, P.-S. Huang, J. C. Vaughan, B. L. Stoddard, D. Baker, De novo design of a fluorescence-activating β-barrel. *Nature* **561**, 485–491 (2018).

13. N. F. Polizzi, W. F. DeGrado, A defined structural unit enables de novo design of small-molecule–binding proteins. *Science* **369**, 1227–1233 (2020).

14. L. Lu, X. Gou, S. K. Tan, S. I. Mann, H. Yang, X. Zhong, D. Gazgalis, J. Valdiviezo, H. Jo, Y. Wu, M. E. Diolaiti, A. Ashworth, N. F. Polizzi, W. F. DeGrado, De novo design of drug-binding proteins with predictable binding energy and specificity. *Science* **384**, 106–112 (2024).

15. R. Stenner, J. W. Steventon, A. Seddon, J. L. R. Anderson, A de novo peroxidase is also a promiscuous yet stereoselective carbene transferase. *Proceedings of the National Academy of Sciences* **117**, 1419–1428 (2020).

16. S. D. Copley, An evolutionary biochemist's perspective on promiscuity. *Trends in Biochemical Sciences* **40**, 72–78 (2015).

17. J. Söding, A. N. Lupas, More than the sum of their parts: on the evolution of proteins from peptides. *Bioessays* **25**, 837–846 (2003).

18. Cell Boundaries: How Membranes and Their Proteins Work, *Routledge & CRC Press*. https://www.routledge.com/Cell-Boundaries-How-Membranes-and-Their-Proteins-Work/White-vonHeijne-Engelman/p/book/9780367357160.

19. D. M. Rosenbaum, S. G. F. Rasmussen, B. K. Kobilka, The structure and function of G-protein-coupled receptors. *Nature* **459**, 356–363 (2009).

20. D. Mishra, T. Z. Markus, R. Naaman, M. Kettner, B. Göhler, H. Zacharias, N. Friedman, M. Sheves, C. Fontanesi, Spin-dependent electron transmission through bacteriorhodopsin embedded in purple membrane. *Proceedings of the National Academy of Sciences* **110**, 14872–14876 (2013).

21. D. N. Woolfson, Understanding a protein fold: The physics, chemistry, and biology of α-helical coiled coils. *Journal of Biological Chemistry* **299** (2023).

22. M. Fasano, S. Curry, E. Terreno, M. Galliano, G. Fanali, P. Narciso, S. Notari, P. Ascenzi, The extraordinary ligand binding properties of human serum albumin. *IUBMB Life* **57**, 787–796 (2005).

23. A. Lee, J. D. Stewart, J. Clardy, B. Ganem, New insight into the catalytic mechanism of chorismate mutases from structural studies. *Chemistry & Biology* **2**, 195–203 (1995).

24. H. Qin, J. P. Edwards, L. Zaritskaya, A. Gupta, C. J. Mu, T. J. Fry, D. M. Hilbert, D. W. LaFleur, Chimeric Antigen Receptors Incorporating D Domains Targeting CD123 Direct Potent Mono- and Bi-specific Antitumor Activity of T Cells. *Molecular Therapy* **27**, 1262–1274 (2019).

25. S. Berger, F. Seeger, T.-Y. Yu, M. Aydin, H. Yang, D. Rosenblum, L. Guenin-Macé, C. Glassman, L. Arguinchona, C. Sniezek, A. Blackstone, L. Carter, R. Ravichandran, M. Ahlrichs, M. Murphy, I. S. Pultz, A. Kang, A. K. Bera, L. Stewart, K. C. Garcia, S. Naik, J. B. Spangler, F. Beigel, M. Siebeck, R. Gropp, D. Baker, Preclinical proof of principle for orally delivered Th17 antagonist miniproteins. *Cell* **187**, 4305-4317.e18 (2024).

26. D. A. Erlanson, S. W. Fesik, R. E. Hubbard, W. Jahnke, H. Jhoti, Twenty years on: the impact of fragments on drug discovery. *Nat Rev Drug Discov* **15**, 605–619 (2016).

27. J. C. Aschenbrenner, A. S. de Godoy, M. Fairhead, C. W. E. Tomlinson, M. Winokan, B. H. Balcomb, E. Capkin, A. V. Chandran, M. Golding, L. Koekemoer, R. M. Lithgo, P. G. Marples, X. Ni, W. Thompson, C. Wild, M.-A. E. Xavier, D. Fearon, F. von Delft, Identifying novel chemical matter against the Chikungunya virus nsP3 macrodomain through crystallographic fragment screening. *bioRxiv*, 2024.08.23.609196 (2024).

28. M. Schuller, G. J. Correy, S. Gahbauer, D. Fearon, T. Wu, R. E. Díaz, I. D. Young, L. Carvalho Martins, D. H. Smith, U. Schulze-Gahmen, T. W. Owens, I. Deshpande, G. E. Merz, A. C. Thwin, J. T. Biel, J. K. Peters, M. Moritz, N. Herrera, H. T. Kratochvil, QCRG Structural Biology Consortium, A. Aimon, J. M. Bennett, J. Brandao Neto, A. E. Cohen, A. Dias, A. Douangamath, L. Dunnett, O. Fedorov, M. P. Ferla, M. R. Fuchs, T. J. Gorrie-Stone, J. M. Holton, M. G. Johnson, T. Krojer, G. Meigs, A. J. Powell, J. G. M. Rack, V. L. Rangel, S. Russi, R. E. Skyner, C. A. Smith, A. S. Soares, J. L. Wierman, K. Zhu, P. O'Brien, N. Jura, A. Ashworth, J. J. Irwin, M. C. Thompson, J. E. Gestwicki, F. von Delft, B. K. Shoichet, J. S. Fraser, I. Ahel, Fragment binding to the Nsp3 macrodomain of SARS-CoV-2 identified through crystallographic screening and computational docking. *Sci Adv* **7**, eabf8711 (2021).

29. D. Röthlisberger, O. Khersonsky, A. M. Wollacott, L. Jiang, J. DeChancie, J. Betker, J. L. Gallaher, E. A. Althoff, A. Zanghellini, O. Dym, S. Albeck, K. N. Houk, D. S. Tawfik, D. Baker, Kemp elimination catalysts by computational enzyme design. *Nature* **453**, 190–195 (2008).

30. R. Blomberg, H. Kries, D. M. Pinkas, P. R. E. Mittl, M. G. Grütter, H. K. Privett, S. L. Mayo, D. Hilvert, Precision is essential for efficient catalysis in an evolved Kemp eliminase. *Nature* **503**, 418–421 (2013).

31. D. Patsch, T. Schwander, M. Voss, D. Schaub, S. Hüppi, M. Eichenberger, P. Stockinger, L. Schelbert, S. Giger, F. Peccati, G. Jiménez-Osés, M. Mutný, A. Krause, U. T. Bornscheuer, D. Hilvert, R. M. Buller, Enriching productive mutational paths accelerates enzyme evolution. *Nat Chem Biol* **20**, 1662–1669 (2024).

32. H. K. Privett, G. Kiss, T. M. Lee, R. Blomberg, R. A. Chica, L. M. Thomas, D. Hilvert, K. N. Houk, S. L. Mayo, Iterative approach to computational enzyme design. *Proceedings of the National Academy of Sciences* **109**, 3790–3795 (2012).

33. I. V. Korendovych, D. W. Kulp, Y. Wu, H. Cheng, H. Roder, W. F. DeGrado, Design of a switchable eliminase. *Proceedings of the National Academy of Sciences* **108**, 6823–6827 (2011).

34. S. Bhattacharya, E. G. Margheritis, K. Takahashi, A. Kulesha, A. D'Souza, I. Kim, J. H. Yoon, J. R. H. Tame, A. N. Volkov, O. V. Makhlynets, I. V. Korendovych, NMR-guided directed evolution. *Nature* **610**, 389–393 (2022).

35. A. Broom, R. V. Rakotoharisoa, M. C. Thompson, N. Zarifi, E. Nguyen, N. Mukhametzhanov, L. Liu, J. S. Fraser, R. A. Chica, Ensemble-based enzyme design can recapitulate the effects of laboratory directed evolution in silico. *Nat Commun* **11**, 4808 (2020).

36. V. A. Risso, S. Martinez-Rodriguez, A. M. Candel, D. M. Krüger, D. Pantoja-Uceda, M. Ortega-Muñoz, F. Santoyo-Gonzalez, E. A. Gaucher, S. C. L. Kamerlin, M. Bruix, J. A. Gavira, J. M. Sanchez-Ruiz, De novo active sites for resurrected Precambrian enzymes. *Nat Commun* **8**, 16113 (2017).

37. H. A. Bunzel, J. L. R. Anderson, D. Hilvert, V. L. Arcus, M. W. van der Kamp, A. J. Mulholland, Evolution of dynamical networks enhances catalysis in a designer enzyme. *Nat. Chem.* **13**, 1017–1022 (2021).

38. J. P. Schwans, D. A. Kraut, D. Herschlag, Determining the catalytic role of remote substrate binding interactions in ketosteroid isomerase. *Proc Natl Acad Sci U S A* **106**, 14271–14275 (2009).

39. S. J. Putman, A. F. Coulson, I. R. Farley, B. Riddleston, J. R. Knowles, Specificity and kinetics of triose phosphate isomerase from chicken muscle. *Biochem J* **129**, 301–310 (1972).

40. J. D. Schnettler, M. S. Wang, M. Gantz, H. A. Bunzel, C. Karas, F. Hollfelder, M. H. Hecht, Selection of a promiscuous minimalist cAMP phosphodiesterase from a library of de novo designed proteins. *Nat. Chem.* **16**, 1200–1208 (2024).

41. T. A. Farid, G. Kodali, L. A. Solomon, B. R. Lichtenstein, M. M. Sheehan, B. A. Fry, C. Bialas, N. M. Ennist, J. A. Siedlecki, Z. Zhao, M. A. Stetz, K. G. Valentine, J. L. R. Anderson, A. J. Wand, B. M. Discher, C. C. Moser, P. L. Dutton, Elementary tetrahelical protein design for diverse oxidoreductase functions. *Nat Chem Biol* **9**, 826–833 (2013).

42. A. E. Donnelly, G. S. Murphy, K. M. Digianantonio, M. H. Hecht, A de novo enzyme catalyzes a life-sustaining reaction in Escherichia coli. *Nat Chem Biol* **14**, 253–255 (2018).

43. A. J. Burton, A. R. Thomson, W. M. Dawson, R. L. Brady, D. N. Woolfson, Installing hydrolytic activity into a completely de novo protein framework. *Nature Chem* **8**, 837–844 (2016).

44. N. F. Polizzi, Y. Wu, T. Lemmin, A. M. Maxwell, S.-Q. Zhang, J. Rawson, D. N. Beratan, M. J. Therien, W. F. DeGrado, De novo design of a hyperstable non-natural protein–ligand complex with sub-Å accuracy. *Nature Chem* **9**, 1157–1164 (2017).

45. A. J. Reig, M. M. Pires, R. A. Snyder, Y. Wu, H. Jo, D. W. Kulp, S. E. Butch, J. R. Calhoun, T. Szyperski, E. I. Solomon, W. F. DeGrado, Alteration of the oxygen-dependent reactivity of de novo Due Ferri proteins. *Nature Chem* **4**, 900–906 (2012).

46. S. I. Mann, A. Nayak, G. T. Gassner, M. J. Therien, W. F. DeGrado, De Novo Design, Solution Characterization, and Crystallographic Structure of an Abiological Mn-Porphyrin-

Binding Protein Capable of Stabilizing a Mn(V) Species. *J Am Chem Soc* **143**, 252–259 (2021).

47. J. Dauparas, G. R. Lee, R. Pecoraro, L. An, I. Anishchenko, C. Glasscock, D. Baker, Atomic context-conditioned protein sequence design using LigandMPNN. bioRxiv [Preprint] (2023). https://doi.org/10.1101/2023.12.22.573103.

48. J. Abramson, J. Adler, J. Dunger, R. Evans, T. Green, A. Pritzel, O. Ronneberger, L. Willmore, A. J. Ballard, J. Bambrick, S. W. Bodenstein, D. A. Evans, C.-C. Hung, M. O'Neill, D. Reiman, K. Tunyasuvunakool, Z. Wu, A. Žemgulytė, E. Arvaniti, C. Beattie, O. Bertolli, A. Bridgland, A. Cherepanov, M. Congreve, A. I. Cowen-Rivers, A. Cowie, M. Figurnov, F. B. Fuchs, H. Gladman, R. Jain, Y. A. Khan, C. M. R. Low, K. Perlin, A. Potapenko, P. Savy, S. Singh, A. Stecula, A. Thillaisundaram, C. Tong, S. Yakneen, E. D. Zhong, M. Zielinski, A. Žídek, V. Bapst, P. Kohli, M. Jaderberg, D. Hassabis, J. M. Jumper, Accurate structure prediction of biomolecular interactions with AlphaFold 3. *Nature* **630**, 493–500 (2024).

49. Z. Lin, H. Akin, R. Rao, B. Hie, Z. Zhu, W. Lu, N. Smetanin, R. Verkuil, O. Kabeli, Y. Shmueli, A. dos Santos Costa, M. Fazel-Zarandi, T. Sercu, S. Candido, A. Rives, Evolutionary-scale prediction of atomic-level protein structure with a language model. *Science* **379**, 1123–1130 (2023).

50. J. L. Watson, D. Juergens, N. R. Bennett, B. L. Trippe, J. Yim, H. E. Eisenach, W. Ahern, A. J. Borst, R. J. Ragotte, L. F. Milles, B. I. M. Wicky, N. Hanikel, S. J. Pellock, A. Courbet, W. Sheffler, J. Wang, P. Venkatesh, I. Sappington, S. V. Torres, A. Lauko, V. De Bortoli, E. Mathieu, S. Ovchinnikov, R. Barzilay, T. S. Jaakkola, F. DiMaio, M. Baek, D. Baker, De novo design of protein structure and function with RFdiffusion. *Nature* **620**, 1089–1100 (2023).

51. J. B. Ingraham, M. Baranov, Z. Costello, K. W. Barber, W. Wang, A. Ismail, V. Frappier, D. M. Lord, C. Ng-Thow-Hing, E. R. Van Vlack, S. Tie, V. Xue, S. C. Cowles, A. Leung, J. V. Rodrigues, C. L. Morales-Perez, A. M. Ayoub, R. Green, K. Puentes, F. Oplinger, N. V. Panwar, F. Obermeyer, A. R. Root, A. L. Beam, F. J. Poelwijk, G. Grigoryan, Illuminating protein space with a programmable generative model. *Nature* **623**, 1070–1078 (2023).

52. S. Gahbauer, G. J. Correy, M. Schuller, M. P. Ferla, Y. U. Doruk, M. Rachman, T. Wu, M. Diolaiti, S. Wang, R. J. Neitz, D. Fearon, D. S. Radchenko, Y. S. Moroz, J. J. Irwin, A. R. Renslo, J. C. Taylor, J. E. Gestwicki, F. von Delft, A. Ashworth, I. Ahel, B. K. Shoichet, J. S. Fraser, Iterative computational design and crystallographic screening identifies potent inhibitors targeting the Nsp3 macrodomain of SARS-CoV-2. *Proc Natl Acad Sci U S A* **120**, e2212931120 (2023).

53. S. Nad, H. Pal, Unusual Photophysical Properties of Coumarin-151. *J. Phys. Chem. A* **105**, 1097–1106 (2001).

54. R. Das, D. Baker, Macromolecular Modeling with Rosetta. *Annual Review of Biochemistry* **77**, 363–382 (2008).

55. R. Wu, F. Ding, R. Wang, R. Shen, X. Zhang, S. Luo, C. Su, Z. Wu, Q. Xie, B. Berger, J. Ma, J. Peng, High-resolution de novo structure prediction from primary sequence. bioRxiv [Preprint] (2022). https://doi.org/10.1101/2022.07.21.500999.

56. J. R. Lakowicz, Ed., "Solvent and Environmental Effects" in *Principles of Fluorescence Spectroscopy* (Springer US, Boston, MA, 2006; https://doi.org/10.1007/978-0-387-46312-4_6), pp. 205–235.

57. I. D. Kuntz, K. Chen, K. A. Sharp, P. A. Kollman, The maximal affinity of ligands. *Proceedings of the National Academy of Sciences* **96**, 9997–10002 (1999).

58. A. L. Hopkins, G. M. Keserü, P. D. Leeson, D. C. Rees, C. H. Reynolds, The role of ligand efficiency metrics in drug discovery. *Nat Rev Drug Discov* **13**, 105–121 (2014).

59. J. C. Klima, L. A. Doyle, J. D. Lee, M. Rappleye, L. A. Gagnon, M. Y. Lee, E. P. Barros, A. A. Vorobieva, J. Dou, S. Bremner, J. S. Quon, C. M. Chow, L. Carter, D. L. Mack, R. E. Amaro, J. C. Vaughan, A. Berndt, B. L. Stoddard, D. Baker, Incorporation of sensing modalities into de novo designed fluorescence-activating proteins. *Nat Commun* **12**, 856 (2021).

60. V. Lamba, E. Sanchez, L. R. Fanning, K. Howe, M. A. Alvarez, D. Herschlag, M. Forconi, Kemp Eliminase Activity of Ketosteroid Isomerase. *Biochemistry* **56**, 582–591 (2017).

61. D. Listov, E. Vos, G. Hoffka, S. Y. Hoch, A. Berg, S. Hamer-Rogotner, O. Dym, S. C. L. Kamerlin, S. J. Fleishman, High-efficiency Kemp eliminases by complete computational design. bioRxiv [Preprint] (2025). https://doi.org/10.1101/2025.01.04.631280.

62. A. Bhowmick, S. C. Sharma, T. Head-Gordon, The Importance of the Scaffold for de Novo Enzymes: A Case Study with Kemp Eliminase. *J. Am. Chem. Soc.* **139**, 5793–5800 (2017).

63. V. Vaissier, S. C. Sharma, K. Schaettle, T. Zhang, T. Head-Gordon, Computational Optimization of Electric Fields for Improving Catalysis of a Designed Kemp Eliminase. *ACS Catal.* **8**, 219–227 (2018).

64. R. L. Dunbrack, Rotamer libraries in the 21st century. *Curr Opin Struct Biol* **12**, 431–440 (2002).

65. C. Bissantz, B. Kuhn, M. Stahl, A Medicinal Chemist's Guide to Molecular Interactions. *J. Med. Chem.* **53**, 5061–5084 (2010).

66. O. Khersonsky, D. Röthlisberger, O. Dym, S. Albeck, C. J. Jackson, D. Baker, D. S. Tawfik, Evolutionary optimization of computationally designed enzymes: Kemp eliminases of the KE07 series. *J Mol Biol* **396**, 1025–1042 (2010).

67. X. Jing, F. Wu, X. Luo, J. Xu, RaptorX-Single: single-sequence protein structure prediction by integrating protein language models. bioRxiv [Preprint] (2023). https://doi.org/10.1101/2023.04.24.538081.

68. O. Khersonsky, G. Kiss, D. Röthlisberger, O. Dym, S. Albeck, K. N. Houk, D. Baker, D. S. Tawfik, Bridging the gaps in design methodologies by evolutionary optimization of the stability and proficiency of designed Kemp eliminase KE59. *Proceedings of the National Academy of Sciences* **109**, 10358–10363 (2012).

69. M. L. Casey, D. S. Kemp, K. G. Paul, D. D. Cox, Physical organic chemistry of benzisoxazoles. I. Mechanism of the base-catalyzed decomposition of benzisoxazoles. *J. Org. Chem.* **38**, 2294–2301 (1973).

70. M. P. Frushicheva, J. Cao, Z. T. Chu, A. Warshel, Exploring challenges in rational enzyme design by simulating the catalysis in artificial kemp eliminase. *Proceedings of the National Academy of Sciences* **107**, 16869–16874 (2010).

71. P. Wang, J. Zhang, S. Zhang, D. Lu, Y. Zhu, Using High-Throughput Molecular Dynamics Simulation to Enhance the Computational Design of Kemp Elimination Enzymes. *J. Chem. Inf. Model.* **63**, 1323–1337 (2023).

72. S. N. Thorn, R. G. Daniels, M. T. Auditor, D. Hilvert, Large rate accelerations in antibody catalysis by strategic use of haptenic charge. *Nature* **373**, 228–230 (1995).

73. Y. Chen, B. K. Shoichet, Molecular docking and ligand specificity in fragment-based inhibitor discovery. *Nat Chem Biol* **5**, 358–364 (2009).

74. A. Bar-Even, E. Noor, Y. Savir, W. Liebermeister, D. Davidi, D. S. Tawfik, R. Milo, The moderately efficient enzyme: evolutionary and physicochemical trends shaping enzyme parameters. *Biochemistry* **50**, 4402–4410 (2011).

75. D. J. Tantillo, J. Chen, K. N. Houk, Theozymes and compuzymes: theoretical models for biological catalysis. *Curr Opin Chem Biol* **2**, 743–750 (1998).

76. M. P. Frushicheva, M. J. Mills, P. Schopf, M. K. Singh, R. B. Prasad, A. Warshel, Computer aided enzyme design and catalytic concepts. *Current Opinion in Chemical Biology* **21**, 56–62 (2014).

77. C. Acosta-Silva, J. Bertran, V. Branchadell, A. Oliva, Kemp Elimination Reaction Catalyzed by Electric Fields. *ChemPhysChem* **21**, 295–306 (2020).

78. B. L. Vallee, R. J. Williams, Metalloenzymes: the entatic nature of their active sites. *Proc Natl Acad Sci U S A* **59**, 498–505 (1968).

79. B. K. Shoichet, W. A. Baase, R. Kuroki, B. W. Matthews, A relationship between protein stability and protein function. *Proc Natl Acad Sci U S A* **92**, 452–456 (1995).

80. C. Nick Pace, J. Martin Scholtz, A Helix Propensity Scale Based on Experimental Studies of Peptides and Proteins. *Biophysical Journal* **75**, 422–427 (1998).

81. L. I. Gutierrez-Rus, E. Vos, D. Pantoja-Uceda, G. Hoffka, J. Gutierrez-Cardenas, M. Ortega-Muñoz, V. A. Risso, M. A. Jimenez, S. C. L. Kamerlin, J. M. S. Ruiz, Enzyme enhancement

through computational stability design targeting NMR-determined catalytic hotspots. ChemRxiv [Preprint] (2024). https://doi.org/10.26434/chemrxiv-2024-7xxzg.

82. P. M. Collins, J. T. Ng, R. Talon, K. Nekrosiute, T. Krojer, A. Douangamath, J. Brandao-Neto, N. Wright, N. M. Pearce, F. von Delft, Gentle, fast and effective crystal soaking by acoustic dispensing. *Acta Crystallogr D Struct Biol* **73**, 246–255 (2017).

83. W. Kabsch, XDS. *Acta Crystallogr D Biol Crystallogr* **66**, 125–132 (2010).

84. P. R. Evans, G. N. Murshudov, How good are my data and what is the resolution? *Acta Crystallogr D Biol Crystallogr* **69**, 1204–1214 (2013).

85. A. J. McCoy, R. W. Grosse-Kunstleve, P. D. Adams, M. D. Winn, L. C. Storoni, R. J. Read, Phaser crystallographic software. *J Appl Crystallogr* **40**, 658–674 (2007).

86. D. Liebschner, P. V. Afonine, M. L. Baker, G. Bunkóczi, V. B. Chen, T. I. Croll, B. Hintze, L. W. Hung, S. Jain, A. J. McCoy, N. W. Moriarty, R. D. Oeffner, B. K. Poon, M. G. Prisant, R. J. Read, J. S. Richardson, D. C. Richardson, M. D. Sammito, O. V. Sobolev, D. H. Stockwell, T. C. Terwilliger, A. G. Urzhumtsev, L. L. Videau, C. J. Williams, P. D. Adams, Macromolecular structure determination using X-rays, neutrons and electrons: recent developments in Phenix. *Acta Crystallogr D Struct Biol* **75**, 861–877 (2019).

87. P. Emsley, B. Lohkamp, W. G. Scott, K. Cowtan, Features and development of Coot. *Acta Crystallogr D Biol Crystallogr* **66**, 486–501 (2010).

88. R. Keegan, M. Wojdyr, G. Winter, A. Ashton, *DIMPLE* : a difference map pipeline for the rapid screening of crystals on the beamline. *Acta Crystallogr A Found Adv* **71**, s18–s18 (2015).

89. G. J. Correy, M. Rachman, T. Togo, S. Gahbauer, Y. U. Doruk, M. Stevens, P. Jaishankar, B. Kelley, B. Goldman, M. Schmidt, T. Kramer, A. Ashworth, P. Riley, B. K. Shoichet, A. R. Renslo, W. P. Walters, J. S. Fraser, Extensive exploration of structure activity relationships for the SARS-CoV-2 macrodomain from shape-based fragment merging and active learning. bioRxiv [Preprint] (2024). https://doi.org/10.1101/2024.08.25.609621.

90. N. M. Pearce, T. Krojer, A. R. Bradley, P. Collins, R. P. Nowak, R. Talon, B. D. Marsden, S. Kelm, J. Shi, C. M. Deane, F. von Delft, A multi-crystal method for extracting obscured crystallographic states from conventionally uninterpretable electron density. *Nat Commun* **8**, 15123 (2017).

91. M. D. Winn, C. C. Ballard, K. D. Cowtan, E. J. Dodson, P. Emsley, P. R. Evans, R. M. Keegan, E. B. Krissinel, A. G. W. Leslie, A. McCoy, S. J. McNicholas, G. N. Murshudov, N. S. Pannu, E. A. Potterton, H. R. Powell, R. J. Read, A. Vagin, K. S. Wilson, Overview of the CCP4 suite and current developments. *Acta Crystallogr D Biol Crystallogr* **67**, 235–242 (2011).

92. N. W. Moriarty, R. W. Grosse-Kunstleve, P. D. Adams, electronic Ligand Builder and Optimization Workbench (eLBOW): a tool for ligand coordinate and restraint generation. *Acta Crystallogr D Biol Crystallogr* **65**, 1074–1080 (2009).

93. N. M. Pearce, T. Krojer, F. von Delft, Proper modelling of ligand binding requires an ensemble of bound and unbound states. *Acta Crystallogr D Struct Biol* **73**, 256–266 (2017).

94. D. G. Gibson, L. Young, R.-Y. Chuang, J. C. Venter, C. A. Hutchison, H. O. Smith, Enzymatic assembly of DNA molecules up to several hundred kilobases. *Nat Methods* **6**, 343–345 (2009).

95. D. A. Case, H. M. Aktulga, K. Belfon, D. S. Cerutti, G. A. Cisneros, V. W. D. Cruzeiro, N. Forouzesh, T. J. Giese, A. W. Götz, H. Gohlke, S. Izadi, K. Kasavajhala, M. C. Kaymak, E. King, T. Kurtzman, T.-S. Lee, P. Li, J. Liu, T. Luchko, R. Luo, M. Manathunga, M. R. Machado, H. M. Nguyen, K. A. O'Hearn, A. V. Onufriev, F. Pan, S. Pantano, R. Qi, A. Rahnamoun, A. Risheh, S. Schott-Verdugo, A. Shajan, J. Swails, J. Wang, H. Wei, X. Wu, Y. Wu, S. Zhang, S. Zhao, Q. Zhu, T. E. I. Cheatham, D. R. Roe, A. Roitberg, C. Simmerling, D. M. York, M. C. Nagan, K. M. Jr. Merz, AmberTools. *J. Chem. Inf. Model.* **63**, 6183–6191 (2023).

96. Gaussian 09, Revision A.02 – ScienceOpen. https://www.scienceopen.com/document?vid=6be7271f-f651-464b-aee6-ef20b0743b6b.

97. U. C. Singh, P. A. Kollman, An approach to computing electrostatic charges for molecules. *Journal of Computational Chemistry* **5**, 129–145 (1984).

98. B. H. Besler, K. M. Merz Jr., P. A. Kollman, Atomic charges derived from semiempirical methods. *Journal of Computational Chemistry* **11**, 431–439 (1990).

99. J. Wang, W. Wang, P. A. Kollman, D. A. Case, Automatic atom type and bond type perception in molecular mechanical calculations. *Journal of Molecular Graphics and Modelling* **25**, 247–260 (2006).

100. J. Wang, R. M. Wolf, J. W. Caldwell, P. A. Kollman, D. A. Case, Development and testing of a general amber force field. *Journal of Computational Chemistry* **25**, 1157–1174 (2004).

101. S. Izadi, R. Anandakrishnan, A. V. Onufriev, Building Water Models: A Different Approach. *J. Phys. Chem. Lett.* **5**, 3863–3871 (2014).

102. Settle: An analytical version of the SHAKE and RATTLE algorithm for rigid water models - Miyamoto - 1992 - Journal of Computational Chemistry - Wiley Online Library. https://onlinelibrary.wiley.com/doi/10.1002/jcc.540130805.

103. T. Darden, D. York, L. Pedersen, Particle mesh Ewald: An N·log(N) method for Ewald sums in large systems. *The Journal of Chemical Physics* **98**, 10089–10092 (1993).

104. R. J. Gowers, M. Linke, J. Barnoud, T. J. E. Reddy, M. N. Melo, S. L. Seyler, J. Domanski, D. L. Dotson, S. Buchoux, I. M. Kenney, O. Beckstein, "MDAnalysis: A Python Package for the Rapid Analysis of Molecular Dynamics Simulations" (LA-UR-19-29136, Los Alamos National Laboratory (LANL), Los Alamos, NM (United States), 2019); https://doi.org/10.25080/Majora-629e541a-00e.

105. A. N. Alexandrova, D. Röthlisberger, D. Baker, W. L. Jorgensen, Catalytic Mechanism and Performance of Computationally Designed Enzymes for Kemp Elimination. *J. Am. Chem. Soc.* **130**, 15907–15915 (2008).

106. K. Świderek, I. Tuñón, V. Moliner, J. Bertran, Protein Flexibility and Preorganization in the Design of Enzymes. The Kemp Elimination Catalyzed by HG3.17. *ACS Catal.* **5**, 2587–2595 (2015).

107. R. V. Rakotoharisoa, B. Seifinoferest, N. Zarifi, J. D. M. Miller, J. M. Rodriguez, M. C. Thompson, R. A. Chica, Design of Efficient Artificial Enzymes Using Crystallographically Enhanced Conformational Sampling. *J. Am. Chem. Soc.* **146**, 10001–10013 (2024).

108. S. Wang, W. Li, S. Liu, J. Xu, RaptorX-Property: a web server for protein structure property prediction. *Nucleic Acids Res* **44**, W430–W435 (2016).

109. F. Hollfelder, A. J. Kirby, D. S. Tawfik, Off-the-shelf proteins that rival tailor-made antibodies as catalysts. *Nature* **383**, 60–63 (1996).

110. O. Khersonsky, D. Röthlisberger, A. M. Wollacott, P. Murphy, O. Dym, S. Albeck, G. Kiss, K. N. Houk, D. Baker, D. S. Tawfik, Optimization of the in-silico-designed kemp eliminase KE70 by computational design and directed evolution. *J Mol Biol* **407**, 391–412 (2011).

111. M. Merski, B. K. Shoichet, Engineering a model protein cavity to catalyze the Kemp elimination. *Proceedings of the National Academy of Sciences* **109**, 16179–16183 (2012).

112. L. I. Gutierrez-Rus, M. Alcalde, V. A. Risso, J. M. Sanchez-Ruiz, Efficient Base-Catalyzed Kemp Elimination in an Engineered Ancestral Enzyme. *Int J Mol Sci* **23**, 8934 (2022).